CRITICAL VELOCITY OF HIGH-PERFORMANCE YARN TRANSVERSELY IMPACTED BY DIFFERENT INDENTERS

by

Boon Him Lim

A Dissertation

Submitted to the Faculty of Purdue University

In Partial Fulfillment of the Requirements for the degree of

Doctor of Philosophy

School of Aeronautics & Astronautics

West Lafayette, Indiana

May 2019

THE PURDUE UNIVERSITY GRADUATE SCHOOL
STATEMENT OF COMMITTEE APPROVAL

Dr. Weinong Chen, Chair
School of Aeronautics and Astronautics
Dr. James Doyle
School of Aeronautics and Astronautics
Dr. Michael Sangid
School of Aeronautics and Astronautics
Dr. Wenbin Yu
School of Aeronautics and Astronautics

Approved by:

Dr. Weinong Chen
Head of the Graduate Program

I’d like to dedicate this dissertation to my family and those who helped and supported me

ACKNOWLEDGMENTS

First and foremost, I would like to thank my advisor Professor Weinong Chen for his guidance throughout my graduate study. I thank him for allowing me to work in Impact Science Laboratory since I was an undergraduate student. I would be forever grateful for the advice and input that he gave me throughout my graduate study.

I would like to express my gratitude to US Army PEO Soldier and National Institute of Justice (NIJ) for providing financial support on most of the work presented in this dissertation.

I would also like to thank my committee members, Professor James F. Doyle, Professor Michael Sangid and Professor Wenbin Yu for providing inputs and directions into my research problems when needed.

A special thanks to Dr. Michael J. Forrestal for travelling to Purdue University at least once every year to provide insightful idea to solve the research challenges.

I would like to thank my fellow graduate students, Dr. Ben Claus, Dr. Jou-Mei Chu, Dr. Hangjie Liao, Dr. Niranjan Parab, Dr. Matt Hudspeth, Dr. Waterloo Tsutsui, Yizhou Nie, Nes Kedir, Xuedong Zhai, Jinling Gao, and Zherui Guo for their help and support whenever I need it.

Finally, for those who have helped me in one way or another, I greatly appreciate it.

TABLE OF CONTENTS

LIST OF TABLES

LIST OF FIGURES

ABSTRACT

Author: Lim, Boon Him. PhD
Institution: Purdue University
Degree Received: May 2019
Title: Critical Velocity of High-Performance Yarn Transversely Impacted by Different Indenters
Committee Chair: Weinong Chen

Critical velocity is defined as projectile striking velocity that causes instantaneous rupture of the specimen under transverse impact. The main goal of this dissertation was to determine the critical velocities of a Twaron® 2040 warp yarn impacted by different round indenters. Special attention was placed to develop models to predict the critical velocities when transversely impacted by the indenters. An MTS 810 load frame was utilized to perform quasi-static transverse and uniaxial tension experiments to examine the stress concentration and the constitutive mechanical properties of the yarn which were used as an input to the models. A gas/powder gun was utilized to perform ballistic experiments to evaluate the critical velocities of a Twaron® 2040 warp yarn impacted by four different type of round projectiles. These projectiles possessed a radius of curvature of 2 μm, 20 μm, 200 μm and 2 mm. The results showed that as the projectile radius of curvature increased, the critical velocity also increased. However, these experimental critical velocities showed a demonstrated reduction as compared to the classical theory. Post-mortem analysis via scanning electron microscopy on the recovered specimens revealed that the fibers failure surfaces changed from shear to fibrillation as the radius of curvature of the projectile increased. To improve the prediction capability, two additional models, Euler-Bernoulli beam and Hertzian contact, were developed to predict the critical velocity. For the Euler–Bernoulli beam model, the critical velocity was obtained by assuming the specimen ruptured instantaneously when the maximum flexural strain reached the ultimate tensile strain of the yarn upon impact. On the other hand, for the Hertzian contact model, the yarn was assumed to fail when the indentation depth was equivalent to the diameter of the yarn. Unlike Smith theory, the Euler-Bernoulli beam model underestimated the critical velocity for all cases. The Hertzian model was capable of predicting the critical velocities of a Twaron® 2040 yarn transversely impacted by 2 μm and 20 μm round projectiles.

CHAPTER 1. INTRODUCTION

1.1 High-Performance Fibers and its Application

High-performance fibers, such as those manufactured from poly[(benzo-[1,2-d;5,4-d']-benzoxazole-2,6-diyl)-1,4-phenylene] (e.g. Zylon®), phenylene terephthalamides (e.g. Kevlar®, Twaron®) and ultra-high-molecular-weight polyethylene (e.g. Dyneema®, Spectra®) are characterized by their superior mechanical properties. These fibers exhibit an unmatched combination of high Young's modulus, high ultimate tensile strength, high impact resistance, and low density. As such, high-performance fibers have been widely used in many applications such as fire proof clothing, tires, diving glove and cut resistant gloves.

1.2 Motivation

One of the most important applications of high-performance fiber is in ballistic protections application such as soft body armors and turbine fragment containment systems. For these applications, the high-performance fibers often undergo dynamic transverse loading.

A soft body armor typically consists of a number of plies of high-performance fabrics which are intended to protect against small caliber bullet penetration [1]. When a soft body armor is subjected to high velocity impact, the material near the impact face would fail before significant energy is dissipated [2]. Since high-performance fabrics are weaved by using high performance yarns, it is crucial to understand how these yarns fail when subjected to transverse loading. Therefore, the main goal of this dissertation is to understand how high-performance yarn behaved under transverse loading with different indenters at various transverse loading velocities.

1.3 Research Goal and Summary

The high-performance yarn used in the current study was Twaron® 2040 warp yarn extracted from Twaron® CT 709 plain weave fabric. To achieve the research goal, quasi-static transverse loading experiments were performed using an MTS 810 to study the stress concentration developed in the yarn. Then, ballistic experiments were performed to determine the critical velocity to evaluate the ballistic performance of these yarns. Critical velocity is defined as the projectile's striking velocity

that causes instantaneously rupture of the yarn upon transverse impact [3, 4]. Classical theory developed by Smith *et al.* [4] always overestimates the critical velocity as compared to the experimental results [3, 5-8]. Based on the observation in the ballistic experiments, we proposed two models, namely, Euler-Bernoulli beam model and the Hertzian contact model to improve the prediction capability on the critical velocity.

The dissertation is organized as the following: Chapter 2 provides a literature review on the Smith theory and the limitation, including previous work in which they attempted to improve the prediction capability. Chapter 3 presents the axial mechanical properties of the high-performance yarns. In addition, this chapter also provides details on the quasi-static transverse loading experiments with different round indenters and the post-mortem failure surface analysis on the recovered specimens. Chapter 4 presents two models to improve the prediction capability for a Twaron® yarn impacted by razor blade. Chapter 5 presents the ballistic experiments to determine the critical velocity of Twaron® 2040 warp yarn transversely impacted by different round projectiles. In addition, the predicted critical velocities from three different models namely, Smith model, Euler-Bernoulli beam model and Hertzian contact model were compared and discussed in Chapter 5. Chapter 6 presents a summary of the finding of the current research. Chapter 7 presents a special topic on the degradation of high-performance yarn under cyclic mechanical loading. Since the projectile used in these studies were made by steel, Chapter 8 presents the mechanical behavior of steel under constant engineering and true strain rates.

CHAPTER 2. LITERATURE REVIEW

2.1 Critical Velocity

The use of high-performance yarn in soft body armor required understanding of the performance of this yarn under ballistic loading conditions, especially under transverse impact. One of the parameters that dominates the ballistic performance of a yarn subjected to high velocity impact is the critical velocity [3, 6, 9, 10]. Critical velocity is defined as the projectile's striking velocity that causes instantaneous rupture of a yarn upon impact [3, 6]. If a projectile strikes a yarn below such a critical velocity, the yarn would deform in to a "V" shape as shown in Figure 1a. On the other hand, when impacted at or above the critical velocity, insignificant transverse deflection of the yarn is observed. In addition, the yarn would be ruptured instantaneously as shown in Figure 1b [3, 8]. Hence, it is important to predict this critical velocity for a yarn subjected to transverse impact.

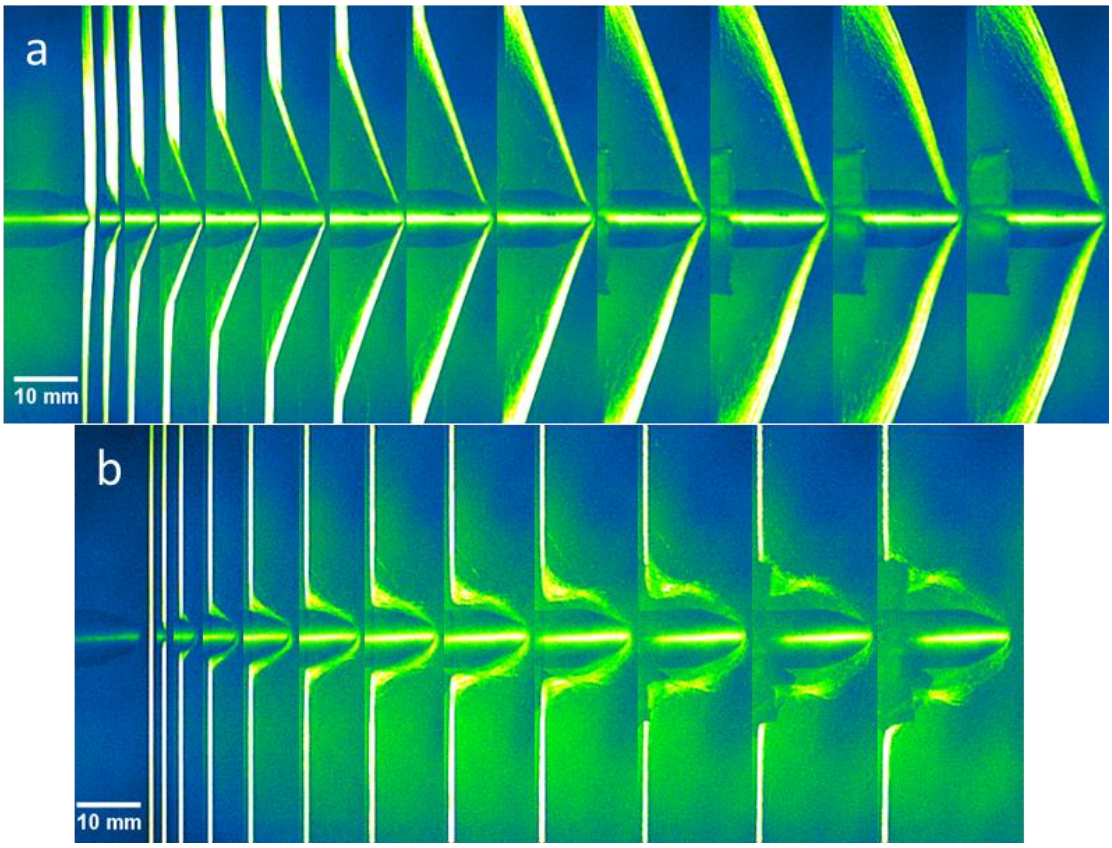

Figure 1: High speed images of a yarn impacted by 2-mm round projectile at (a) below critical velocity (b) above critical velocity.

2.2 Smith Theory

The analytical model that predicts the critical velocity and the transverse wave speed of a yarn subjected to transverse impact is the Smith theory [4, 6]. Figure 2 sketches the deformation of a yarn subjected to transverse impact by a projectile.

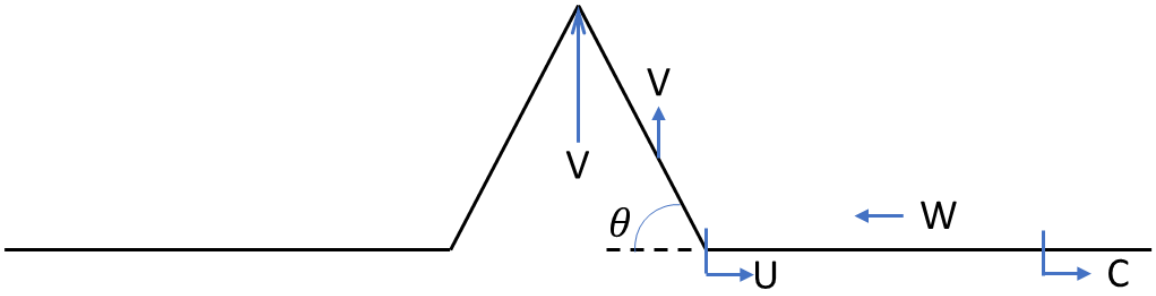

Figure 2: Schematic of infinite length yarn subjected to transverse impact by a projectile [6]

The equations of motion and solutions for Smith theory can be found in [4, 6]. The solution method presented in this section is similar to the work done by Smith *et al.* [4] and Hudspeth *et al.* [6]. The Smith theory could be deduced into five equations: axial wave speed (C), axial particle velocity (W), transverse wave speed (U), transverse particle velocity (V), and angle (θ). The first four equations are needed to predict the critical velocity. When a projectile impacts a yarn, a uniaxial tensile wave is generated at the point of impact. Such a tensile wave propagates at the speed of sound (C) of the material which is given in Eqn. 1,

$$C = \sqrt{\frac{E}{\rho}} \qquad \text{Eqn. 1}$$

where E and ρ are Young's modulus and density of the yarn, respectively. The material behind the uniaxial tensile wave is pulled toward the projectile with a particle velocity given in Eqn. 2,

$$W = C\varepsilon \qquad \text{Eqn. 2}$$

where ε is axial strain developed in the yarn behind the longitudinal wave. In addition, a secondary wave, also known as transverse wave is generated at the point of impact. This transverse wave propagates at a slower speed compared to the uniaxial tensile wave. The mathematical expression for the transverse wave speed is expressed in Eqn. 3.

$$U = C\sqrt{\left(\frac{\varepsilon}{1+\varepsilon}\right)} \qquad \text{Eqn. 3}$$

Similarly, the material behind this transverse wave moves in the striking direction with a transverse particle velocity equivalent to the projectile striking velocity as shown in Eqn. 4.

$$V = \sqrt{(1+\varepsilon)^2 U^2 - [(1+\varepsilon)U - W]^2} \quad \text{Eqn. 4}$$

The angle developed during transverse impact can be determined using Eqn. 5

$$\tan\theta = \frac{V}{U(1+\varepsilon) - W} \quad \text{Eqn. 5}$$

If the axial mechanical properties of the yarn are known, Eqns. 3 and 4 can predict the theoretical transverse wave speed and critical velocity, respectively. When a projectile strikes below the critical velocity, the theoretical and experimental transverse wave speeds are in good agreements [11, 12]. However, a demonstrative reduction in critical velocities from experiments is observed compared to those from theoretical prediction [6, 10, 13].

2.3 Smith Theory Limitation

It is well known that the critical velocity predicted by Smith theory is always overestimated when compared with those obtained from experiments. Several studies were performed in effort to understand why the critical velocity determined from Smith's theory overestimated the actual critical velocity determined from experiments. For example, Bazhenov *et al.* [13] shot a 3-cm spherical metal ball with a striking velocity of 670 m/s into a SVM aramid yarn. These specimens fractured at a striking velocity lower than the theoretical critical velocity. The authors suggested that non-linear constitutive material properties of the SVM yarns at large deformation caused the theoretical critical velocity to be overestimated [13]. In addition, the authors also claimed that non-linear interactions between the projectile and specimen caused the yarn rupture at a lower critical velocity [13].

Chocron *et al.* [10, 11] studied the wave propagation developed in a yarn impacted by a flat head projectile such as fragmented simulating projectile (FSP) and right circular cylinder (RCC). The authors suggested the reason Smith theory overestimated the critical velocity was due to the specimen "bounced-off" from the face of a flat head projectile [10, 11]. When a yarn was impacted by a flat head projectile, two waves were generated at both edges of the projectile and propagated toward the center of the projectile [11]. The transverse particle velocity doubled when these waves met in the middle. This caused the yarn to bounce off from the face of the projectile, ultimately

led to the decreased in critical velocity [10]. Such bouncing phenomenon was also observed experimentally by Field and Sun [12].

Hudspeth *et al.* [3, 5, 6] suggested that such a reduction in the critical velocity was caused by the multi-axial stress developed in the Kevlar® KM2, Dyneema® SK76, and AuTx® yarns during transverse impact. These specimens were loaded in the transverse direction under quasi-static loading conditions using a universal material testing machine (MTS 810) with three indenters: razor blade, 0.30-cal FSP and 0.30-cal round [3, 6]. The mechanical properties and critical velocities of these high-performance yarns were tabulated in Table 1.

Table 1: Mechanical properties of Kevlar® KM2, Dyneema® SK76 and AuTx® yarn.

Properties	Kevlar® KM2	Dyneema® SK76	AuTx®
Density, ρ [kg/m^3] [14, 15]	1440	970	1270
Young's modulus, E [GPa] [3]	99.5	127.5	131.0
Axial breaking strain, ε_{UTS} [%] [3]	2.57	2.68	2.91
Fiber diameter, r [μm] [14-16]	12	18.12	10.22
Experiment critical velocity, Razor Blade [m/s] [3]	145-310	190-315	180-340
Experiment critical velocity, FSP [m/s] [3]	480-645	450-690	540-720
Experiment critical velocity, 0.30-cal Round [m/s] [3]	540-700	505-750	475-805
Smith's critical velocity [m/s] [3]	727	1030	975

The axial rupture strain determined from transverse loading experiments for all three projectiles shows a demonstrative reduction as compared to the ultimate tensile strain [3, 6]. For FSP projectile, most of the fibers failed at the corners suggests. Such phenomenon suggests pre-mature failure have occurred due to the development of multi-axial stress that caused stress concentration at the corners [6]. Therefore, the authors suggested that a possible way to improve the Smith model was to substitute the ultimate tensile strain in Eqn. 4 with the rupture strain determined from quasi-static transverse loading experiments [6]. In addition, a 20-mm powder gun was utilized to determine the critical velocities of yarns impacted by these projectiles [3]. The results showed that

the yarns impacted by a razor blade had the lowest critical velocity, followed by 0.30-cal FSP and then 0.30-cal round [3]. Similar conclusions were also drawn from quasi-static transverse loading experiments, with the rupture strain for yarn loaded with razor blade being the lowest, followed by 0.30-cal FSP and 0.30 round indenters [3, 6].

Numerical simulation presented by Sockalingam *et al.* [17-19] revealed that under transverse impact between cylindrical projectile and a Kevlar® KM2 fiber or yarn would yield flexural waves causing fiber kinking and fibrillation. Since Smith theory did not account for such a phenomenon, the predicted critical velocity was always overestimated as compared to the experiments.

2.4 Research Questions and Gaps

From the literature review, the projectile's nose shape is an important parameter that would influence the critical velocity. Besides that, the interaction between the projectile and yarn must also be considered. However, from Eqn. 4, the critical velocity determined from Smith model, which occurs when the yarn reaches its axial tensile failure strain, is independent of projectile's nose shape and projectile-yarn interaction. A blunt or pointed projectile would have the same predicted critical velocity. To be able to accurately predict the critical velocity, the projectile's nose shape and projectile-yarn interaction must be accounted for. The interaction between the yarn and the projectile causes waves other than axial and transverse wave to develop in the yarn specimen [8, 18, 19]. The interaction also causes stress concentration, introducing other failure modes and ultimately reducing the critical velocity [3, 5-8].

The aim of this research is to improve the prediction capability on the critical velocity. Quasi-static uniaxial tensile experiments were performed to obtain the axial mechanical behavior of the yarn. Then, quasi-static transverse loading experiments were performing using different round indenters to measure the stress concentration in the yarn. Load cells were mounted beneath the indenter and the grips to measure the transverse and axial loads to determine the stress concentration in the yarn. Scanning electron microscopy was utilized to examine the failure surface on the recovered specimens. Then, a strain energy model and a quasi-static curved beam model were used to predict the stress concentration under quasi-static loading conditions.

Ballistic experiments were performed using four different round projectiles to obtain the critical velocities. A high-speed camera was integrated into the ballistic experimental setup to capture the high-speed images of the yarn impacted by the projectile. Failure surface analysis was then performed on the recovered specimen via scanning electron microscopy. Euler-Bernoulli beam model was used to predict the lowest limit of the critical velocity. For those specimens that failed due to shear, Hertzian contact model with shear failure criterion were used to predict their respective critical velocity.

CHAPTER 3. MECHANICAL BEHAVIOR OF HIGH-PERFORMANCE YARNS TRANSVERSELY LOADED BY DIFFERENT INDENTERS

(A version of this chapter has been published in Fibers [7])

3.1 Abstract

In this study, we performed off-axis transverse loading experiments to study the stress concentration developed in a high-performance yarn with different indenters. A universal testing machine was utilized to perform quasi-static transverse loading experiments on Twaron® yarns. Seven different round indenters possessing radius of curvature ranging from 0.20 to 4.50 mm were employed in the experiments. In addition, post-mortem failure analysis was performed on the recovered specimens via a scanning electron microscope. From the transverse loading experiments, the results showed that, as the radius of curvature of the indenters increased, the concentrated load decreased, causing the failure surfaces to change from a combination of kink band, snapped-back, and localized shear to only fibrillations. The concentrated stresses were predicted by a strain energy model when loaded by an indenter with a radius of curvature smaller than 1.59 mm. For indenters larger than 1.59 mm, the specimens failed in fibrillation, the concentrated stresses agreed well with the stresses predicted by quasi-static circular curved beam theory.

Keywords: transverse impact; high-performance fiber; critical velocity; strain energy; curved beam

3.2 Introduction

High performance fibers are known for their superior mechanical properties, including a high Young's modulus, a high ultimate tensile strength, a high impact resistance, and a low density. Due to these superior mechanical properties, high performance fibers have become prominent in ballistic protection applications such as turbine fragment containment systems and soft body armors.

The indicator of the ballistic performance for high-performance yarns is the critical velocity [3, 5, 6, 11, 20]. Critical velocity is defined as the projectile's striking velocity that causes instantaneous

rupture on the yarn specimen upon impact. A classical theory developed by Smith *et al.* [4] has been shown to be capable of predicting the critical velocity using only the axial mechanical properties. However, the critical velocity obtained from the experiments revealed a demonstrative reduction compared to the critical velocity obtained from theoretical analysis [6, 20]. Moreover, ballistic experiments performed by Hudspeth *et al.* [3] revealed that, when a Kevlar® KM2 yarn was impacted by a razor blade and a 7.62 mm round projectile at the corresponding critical velocities, the failure surfaces of the fibers changed from shear to fibrillation. These results suggest that there is a transition radius of curvature that is causing fibers to fail only in fibrillation. However, the transition radius of curvature was not yet determined.

When impacted by a projectile with a large radius of curvature, the stress concentration developed in the yarn specimen was speculated to be caused by bending of the specimen [18, 19]. For example, when a yarn was impacted by a 7.62 mm round projectile, the high-speed images revealed that the yarn deformed to the contour of the projectile prior to failure [21]. This deformation induced an additional component of axial strain caused by bending in the specimens [18].

The classical Smith theory assumes that bending is negligible, which may turn out to be the culprit of inaccurate prediction on the critical velocity. Therefore, in this study, to isolate the bending effects without the addition of inertia effects, quasi-static transverse loading experiments were performed on Twaron® yarns using seven different round indenters to study the stress concentration developed in the yarns. Post-mortem failure analysis was performed on the recovered yarns via a scanning electron microscope (SEM) to correlate the failure mode with the indenter radius and ascertain the critical radius of curvature. Finally, a strain energy model and a quasi-static circular curved beam model were used to predict the concentrated load and to compare with the experimental results.

3.3 Materials and Methods

The specimens used in this study were strands of Twaron® yarns extracted from a plain weave single ply CT 709 Twaron® in the warp direction. According to Teijin Aramid, this fabric is weaved using Twaron® 2040 yarn. This type of yarn consists of 1000 filaments with an average diameter of 9 μm. Plain weave fabric consists of warp and weft directions. An optical method was

used to determine these directions in which the warp yarns typically exhibit more crimp and have thicker widths compared to weft yarns [22]. The specimens used for both uniaxial tensile and transverse loading experiments were extracted from the warp yarns for consistency.

3.3.1 Uniaxial Tensile Experiments

Uniaxial tension experiments were performed using a servo-hydraulic universal testing system (MTS 810) at a quasi-static strain rate of 0.01/s to determine the constitutive properties of the yarn specimens. Figure 3 shows the experimental apparatus used to perform the uniaxial tensile experiments. The experiments were performed with references to ASTM D7269 [23] and ASTM D2256 [24]. First, the specimen was attached to the bollard grip. To minimize the gage length effect, the gage length of the specimens including the curved region of the bollard grips was chosen to be around 190 mm [25]. Furthermore, to minimize the slippage between the specimen and the gripping platen, carbon tape was attached to the platen assembly. A slack-start procedure from ASTM D7269 [23] was deployed in the experimental procedure to ensure that pre-tension on the specimen was minimal. When the specimen was loaded from the slack condition, the load remained zero initially and increased linearly upon loading. The point where the slope of the load history changed from zero to linear was set at the starting point of the experiments. Ten repeated experiments were performed to obtain the mechanical properties and their levels of scattering.

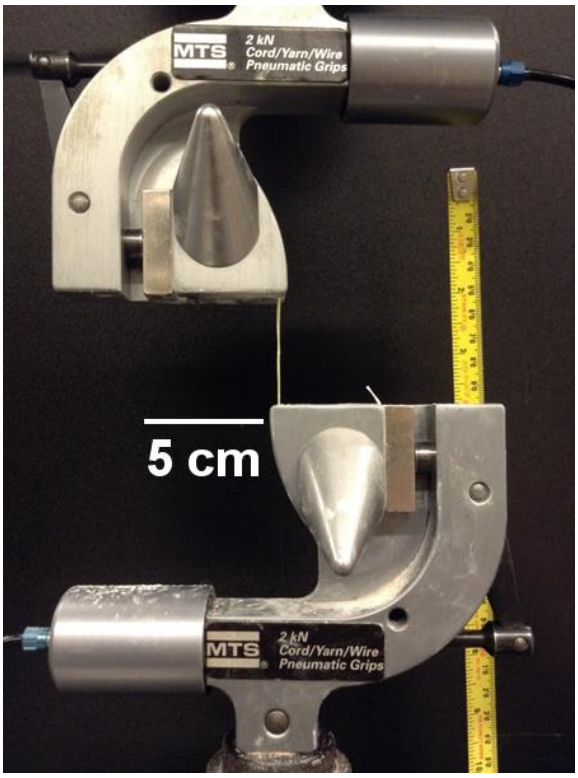

Figure 3: Experimental apparatus for uniaxial tensile experiments.

3.3.2 Transverse Loading Experiments

Transverse loading experiments were performed on the Twaron® yarns to determine the effect of the radius of curvature on the concentrated load developed in the yarns. Figure 4 presents the seven different round indenters used in the current study.

Figure 4: Seven different indenters used in transverse loading experiments. From left to right, the indenters possess radii of curvature of 0.20, 0.40, 0.79, 1.59, 2.50, 3.81, and 4.50 mm.

All of the indenters were made of 316 stainless steel with radii of curvatures of 0.20, 0.40, 0.79, 1.59, 2.50, 3.81, and 4.50 mm. The three largest indenters were made by machining precision steel rods into round indenters with their corresponding radii of curvatures at the tips, as shown on the right side in Figure 4. On the other hand, the four smaller round indenters were made by placing

the precision ground dowel pins on top of the pin holder, as shown on the left side in Figure 4. These pin holders prevented the dowel pins from bending during the experiments. A new dowel pin was used in every experiment to ensure the respective radius of curvature remains the same across the experiments. Similar to uniaxial tensile experiments, the gage length used in the transverse loading experiments was 190 mm. To facilitate the attachment of specimens on the grips, both ends of the yarns were first sandwiched and glued with two pieces of paper cardboards using epoxy adhesive. The specimen was then gripped between the block grippers using fasteners. Of all the experiments performed, none of the specimens slipped out or failed at any of the grips which suggested that the end effects due to this gripping method was negligible. A load cell was mounted below the indenter to measure the transverse load. Two additional load cells were mounted at the grips to record the axial load. These load cells were mounted at 45 degrees (angle between the horizontal axis and the specimen), as shown in Figure 5. At a 45-degree starting angle, the corresponding breaking angle was similar due to the small failure strain in the yarn. This setup ensured that both load cells mounted at the grips indeed measured the axial load in the yarn [5, 6]. Similar to uniaxial tension experiments, the slack-start procedure, including the determination of the starting point, was utilized to ensure that the pre-tension in the specimen, if any, was minimal [23]. The indenters moved up vertically at a speed of 1.9 mm/s. As a result, the yarns were loaded with an axial strain rate of 0.014/s. For each indenter, 10 repeated experiments were performed.

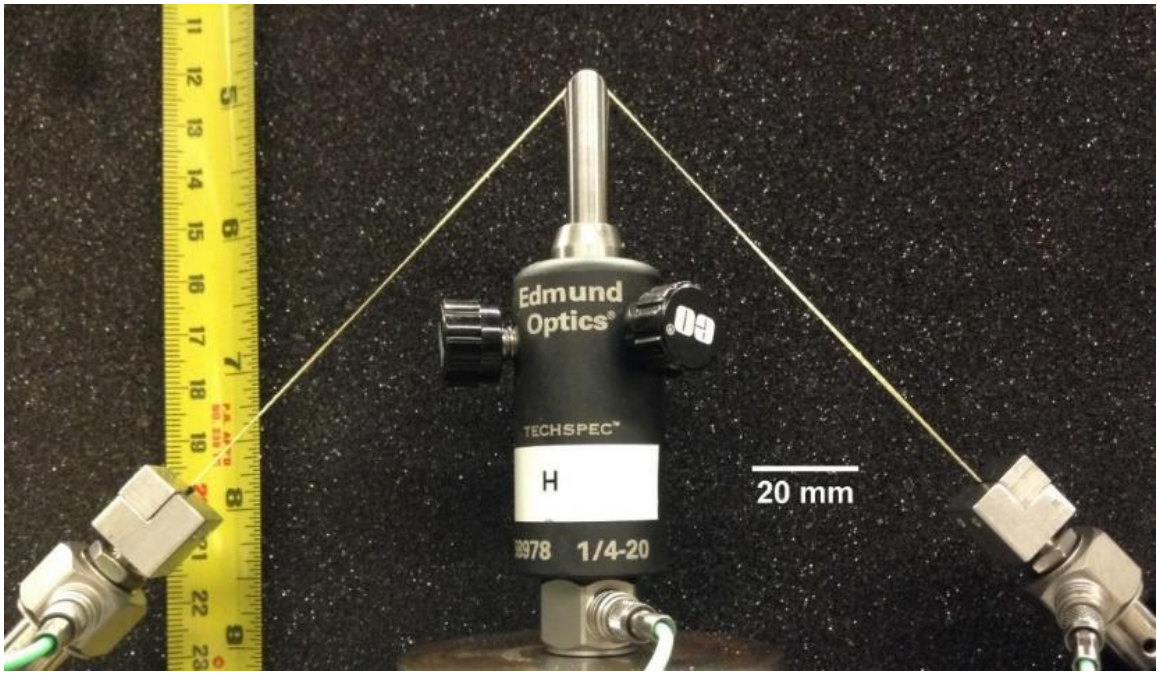

Figure 5: Experimental apparatus for transverse loading experiment.

3.4 Results

The axial tensile stress–strain properties of Twaron® 2040 yarns were obtained via uniaxial tensile experiments. The stress–strain curves for all 10 experiments are presented in Figure 6. Prior to rupture, the stress–strain relationship was linear, which was similar to those observed by Cheng *et al.* for Kevlar® [16]. The average and standard deviation values for the Young's modulus (E), ultimate tensile strength (σ_{uts}), and ultimate tensile strain were 92.55 ± 1.66 GPa, 2.47 ± 0.08 GPa, and 2.71 ± 0.08%, respectively.

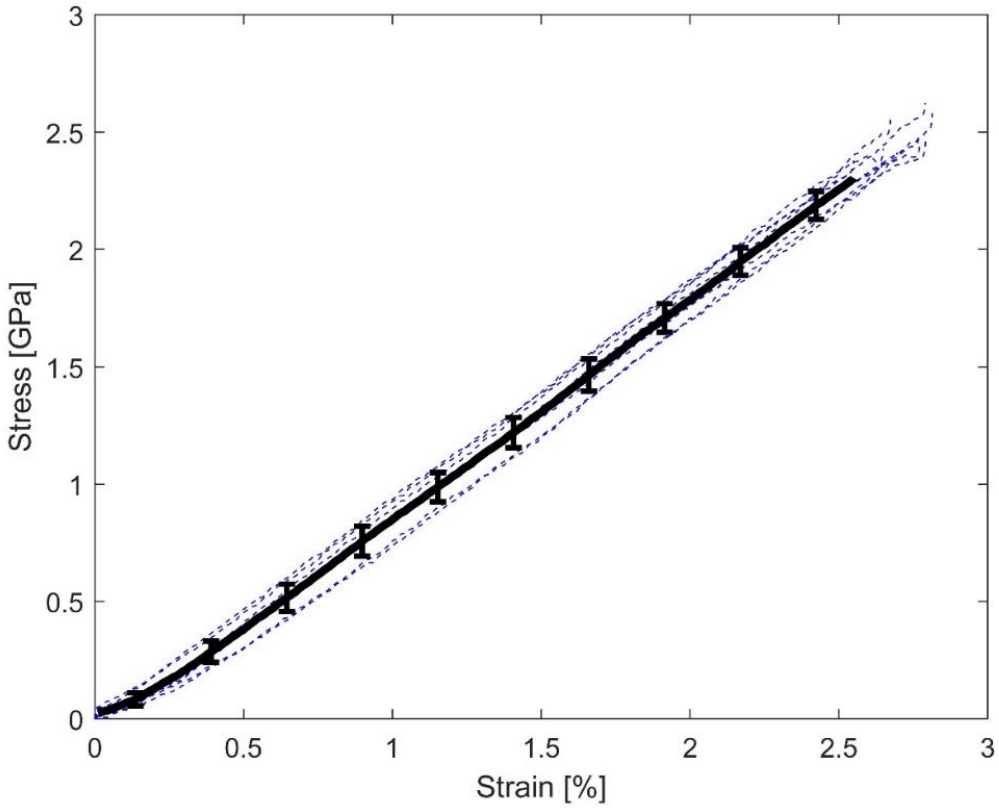

Figure 6: Stress–strain curves for all 10 experiments. The dashed curves indicate the experimental data, whereas the solid curve indicates the average stress–strain curve.

On the other hand, Table 1 lists the maximum axial load and maximum transverse load obtained from the transverse loading experiments for all seven cases. The results and errors reported in

Table 2: Maximum axial and transverse load for seven different indenters.

Radius of Curvature [mm]	Maximum Axial Load, P_{ax} [N]	Maximum Transverse Load [N]
0.20	132.7 ± 1.7	192.0 ± 3.3
0.40	137.6 ± 3.0	200.0 ± 4.5
0.79	139.3 ± 2.0	201.7 ± 2.9
1.59	138.7 ± 4.5	204.6 ± 4.2
2.50	145.5 ± 4.8	211.8 ± 4.7
3.81	150.5 ± 3.6	220.7 ± 5.2
4.50	151.3 ± 5.4	222.0 ± 6.4

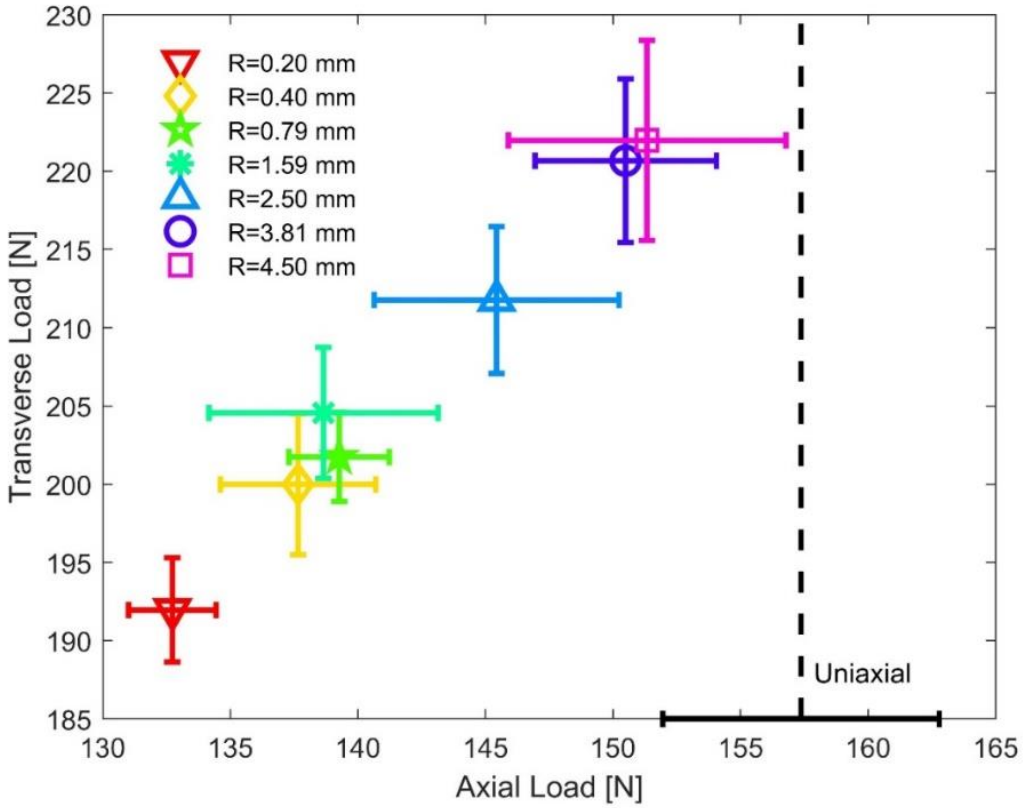

Figure 7: Transverse load versus axial load at failure for seven different indenters.

The results in Figure 7 show that the maximum axial loads under quasi-static transverse loading were lower than the ultimate tensile load for all cases. This phenomenon suggested that a stress concentration exists in a yarn under transverse loading conditions [3, 6]. One approach to describe the stress concentration is to take the difference between the ultimate tensile load and maximum axial load and divide the result by the cross-sectional area of the yarn for each case. The corresponding results are presented in Figure 8.

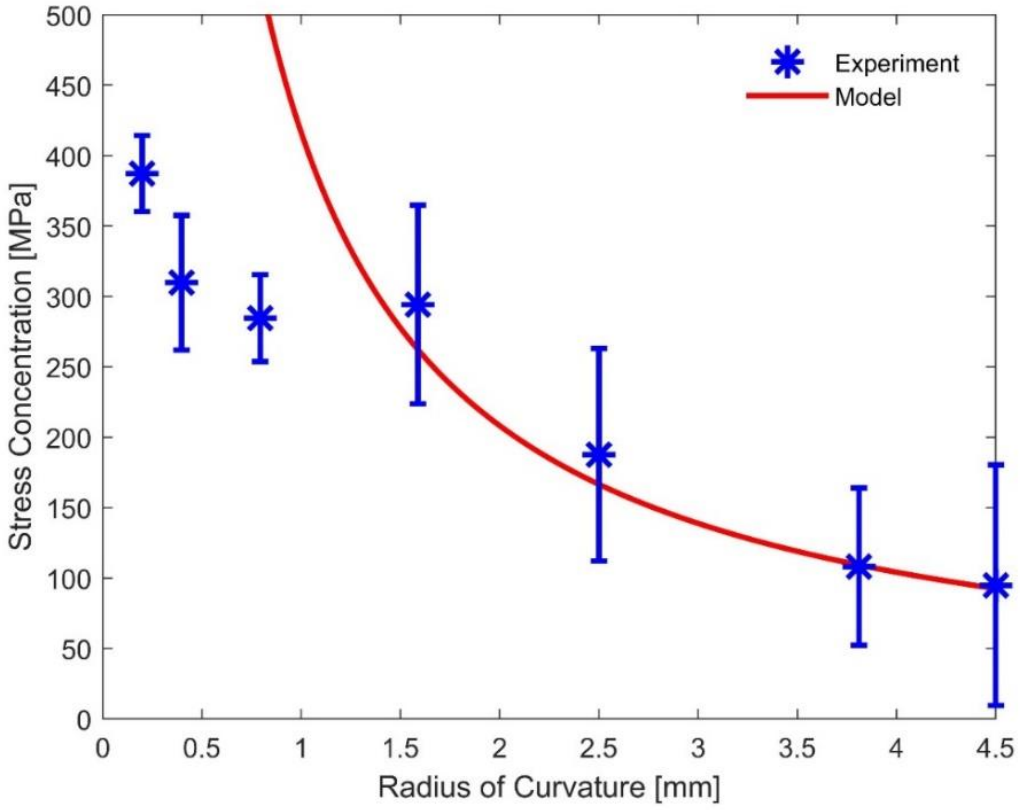

Figure 8: Stress concentration in the yarns for seven different indenters.

As can be seen in Figure 8, the stress concentration decreased as the radius of curvature increased. This trend agrees with the experimental results obtained from Hudspeth *et al.* [3, 5], who performed transverse loading experiments with a razor blade and a 7.62 mm round projectile. Furthermore, when transversely loaded by an indenter with a smaller radius of curvature, the load was localized in a concentrated area, leading to a decrease in standard deviation.

3.5 Discussion

In this section, we explore the models to predict the stress concentration developed in the yarns when transversely loaded by these indenters. The stress concentration developed in a Twaron® 2040 yarn when transversely loaded by an indenter possessing a radius of curvature between 0.20 and 1.59 mm was predicted by the strain energy model. However, for an indenter larger than 1.59 mm, the stress concentration was estimated by a curved beam model.

3.5.1 Strain Energy Model

By taking the difference between the specific axial strain energy from the uniaxial tensile experiments (u_{uts}) and the transverse loading experiments (u_{ax}), the residual specific strain energy (u_{res}) was determined for each case using Equation 6 [13]:

$$u_{res} = u_{uts} - u_{ax} = \frac{1}{2E}[\sigma_{uts}^2 - \left(\frac{P_{ax}}{A_y}\right)^2] \quad \text{Eqn. 6}$$

where P_{ax} is the average maximum axial load from the transverse loading experiments and A_y is the cross-sectional area of a yarn. The strain energy was then calculated by taking the volume integral of the specific strain energy around the arc of the indenter as formulated in Equation 7:

$$U_{res} = \int u_{res}\, dV = \frac{1}{2}\pi R A_y u_{res} \quad \text{Eqn. 7}$$

where R is the radius of curvature of the indenter, and $\frac{1}{2}\pi R$ is the arc length of the yarn on top of the indenter that was transversely loaded at 45°. The average residual strain energy, as a function of radius of curvature of the indenter, is presented in Figure 9.

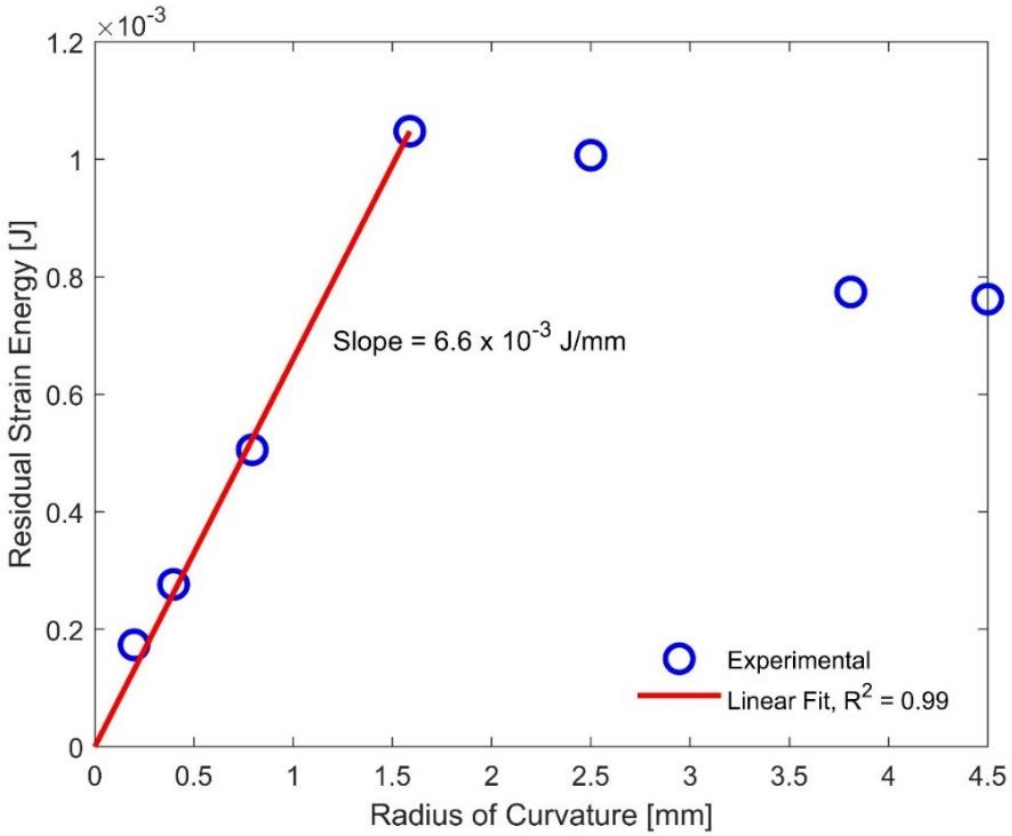

Figure 9: Residual strain energy for seven different indenters.

In Figure 9, it can be seen that the residual strain energy for a small radius of curvature up to 1.59 mm forms a linear curve with a slope of 6.6×10^{-3} J/mm and a coefficient of determination (R^2) of 0.99. These results also indicate that the stress concentration developed in a Twaron® 2040 yarn loaded transversely by an indenter possessing a radius of curvature between 0.20 and 1.59 mm can be predicted using Equations 6 and 7 together with the slope given in Figure 9. Additionally, from Figure 9, for the cases above 1.59 mm, the experimental data revealed a non-linear behavior. These results suggested that the failure mode may have changed when transversely loaded with a larger indenter. Thus, we used a curved beam model to explore the change in driving force behind the failure mode change.

3.5.2 The Curved Beam Model

Quasi-static circular curved beam model was used to describe the stress concentration developed in the yarns when transversely loaded by a large radius of curvature indenter. Under transverse loading, the yarn was deformed to the contour of the indenter prior to failure. Even though Twaron® 2040 yarn consists of 1000 fibers, only 3 fibers are shown in Figure 10 for illustration purposes. When the radius of curvature is relatively larger compared to the fiber radius, the centroid axis is almost equivalent to the neutral axis where the engineering strain along each of these axes is zero [26].

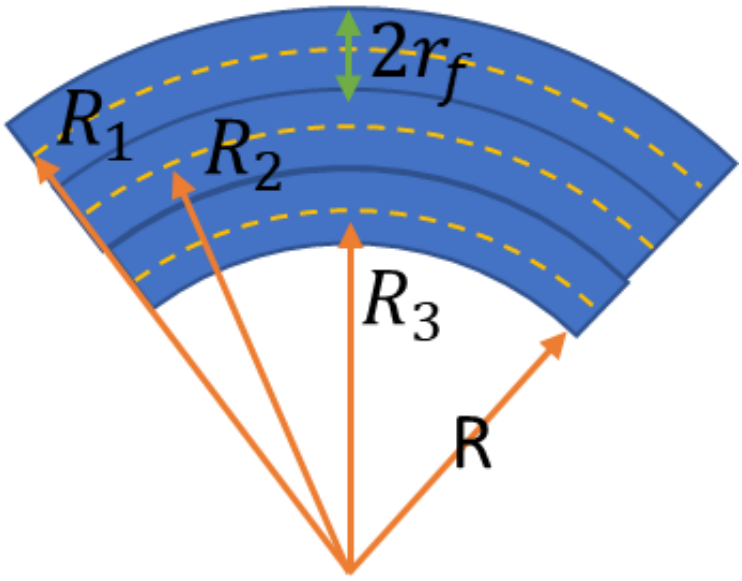

Figure 10: Schematic of circular curved beam.

The maximum bending strains that occur for each fiber at the outer surface are given in Equation 8 [26]:

$$\varepsilon_b^1 = \frac{r_f}{R_1} = \frac{r_f}{R + 5r_f}$$
$$\varepsilon_b^2 = \frac{r_f}{R_2} = \frac{r_f}{R + 3r_f} \quad \text{Eqn. 8}$$
$$\varepsilon_b^3 = \frac{r_f}{R_2} = \frac{r_f}{R + r_f}$$

where ε_b and r_f indicate the bending strain and the radius of fiber, respectively. If the radius of curvature of the indenter is significantly larger than the radius of the fiber (i.e., $R \gg r_f$), the bending stress in each fiber along the axial direction may be approximated as the ratio of the radius of fiber to the radius of curvature as given in Equation 9.

$$\sigma_b = \sigma_b^1 = \sigma_b^2 = \sigma_b^3 = E\frac{r_f}{R}. \quad \text{Eqn. 9}$$

According to Equation 9, when the radius of curvature of the indenter increases, the bending stress developed in the specimen decreases. Superimposing this prediction from Equation 9 into Figure 8, the quasi-static curved beam theory describes the experimental results on the stress concentration very well, especially when the radius of curvature is larger than 1.59 mm. The agreed results between the experiments and the model suggest that, under transverse loading, the stress concentration developed in the yarn is very likely to be caused by the bending stress. However, when the radius of curvature of the indenter was less than 1.59 mm, the theory overestimated the stress concentration developed in the yarn under transverse loading. This deviation could be the results of a failure mode change in the yarn caused by the change in the radius of curvature of the indenter for which the curved beam model does not account for. We thus examined the failure surfaces of the recovered yarns.

3.5.3 Failure Surfaces

To understand how these yarns failed under transverse loading condition, an FEI Nova Nano scanning electron microscope (SEM) was used to examine the failure surfaces of the recovered specimens. An ETD detector was used for the SEM imaging. Furthermore, all the images presented were taken with an operating voltage of 5 kV (HV), a spot size of 3, and an average working distance of 5 mm. Figure 11 presents the post-mortem images of the recovered fibers that failed in

fibrillation loaded transversely by five of the indenters, excluding two of the largest radius indenters.

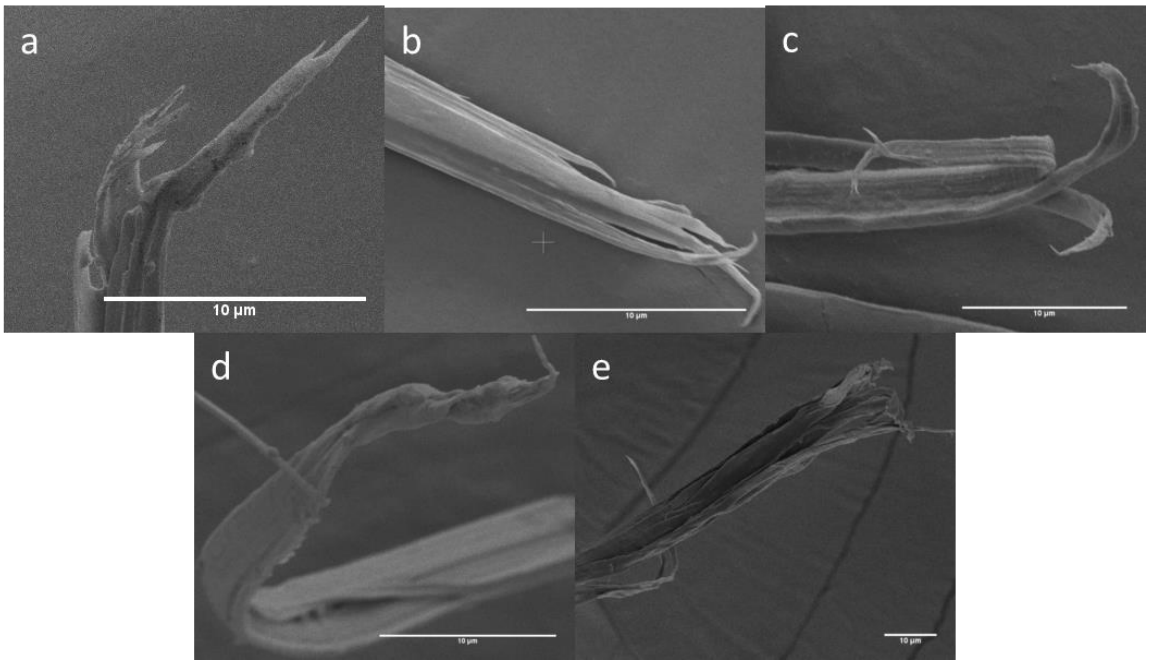

Figure 11: Fibrillation of fiber transversely loaded by indenter with radii of curvature of (a) 0.20, (b) 0.40, (c) 0.79, (d) 1.59, and (e) 2.50 mm. All scale bars are 10 µm.

When loaded transversely by a 0.20 mm indenter, the fibers failed by axial splitting, causing them to fibrillate, as shown in Figure 11a [27]. At failure, the release of strain energy caused the snapping back behavior of the fibers as shown in Figure 12b [27]. The failure location then became a free end. To remain stress free at that location, a compressive load must be generated and propagated in the fibers, which led to buckling and created kink bands, as shown in Figure 12a [27]. In Figure 12a, it can be seen that the fiber, at one end, bent downward and, at the other, bent upward. This phenomenon suggested that the kink bands were formed after the fiber snapped back—not after it was severely bent. For severe local bending, both ends of the fibers should bend in the same direction, as sketched in Figure 10.

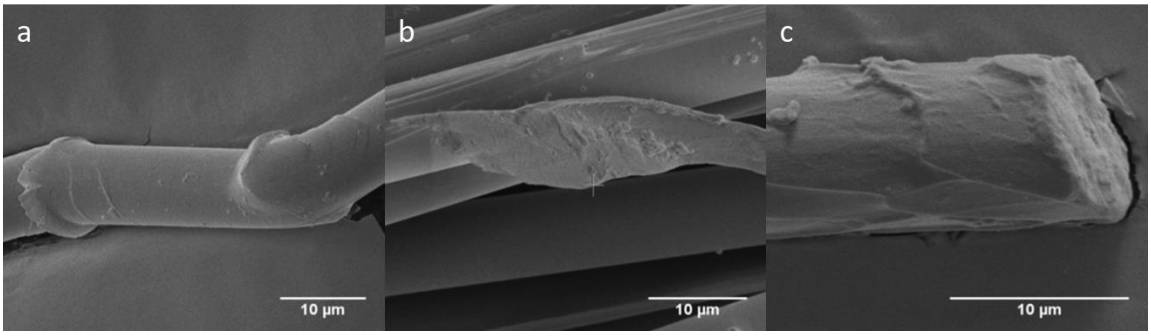

Figure 12: Additional failure surfaces that caused the fibers to form (a) kink-band, (b) snapped-back and (c) localized shear. All scale bars are 10 µm.

A similar failure mechanism was also observed when the yarn was loaded transversely by a 0.40 mm indenter. However, the failure surfaces at the end of some fibers were flattened, suggesting that the localized cutting occurred when the yarn was loaded transversely by such a projectile, as shown in Figure 12c. Such a localized cutting phenomenon was also observed by Hudspeth *et al.* [3, 5], Shin *et al.* [28], and Maya and Wetzel [9].

For the failure mechanism induced by an indenter with radius of curvature of 0.79 mm, the fibers underwent fibrillation (Figure 11c) and localized shear failure only. Neither the kink band nor snapped-back behaviors was observed. The fibrillated fibers revealed a rectangular shape and flatter surfaces (Figure 11c) compared to those loaded by the smaller indenters.

For the cases where the indenters had radii of curvature of 1.59 and 2.50 mm, the failure surfaces of the fibers only showed fibrillation, as shown in Figures 11d,e. This observation was very similar to those observed by Hudspeth *et al.* [3] under transverse impact by a 7.62 mm round projectile and by Cheng *et al.* [16] under uniaxial tensile loading. The fibrillated failure region revealed flatter damage for those loaded by 1.59 mm indenters compared to those loaded by 2.50 mm indenters. Unlike the previous indenters, localized cutting, shearing, snapped-back, and kink-band failure modes were not observed when loaded by 1.59 and 2.50 mm indenters. Such a scenario was caused by the lower stress concentration and the strain energy released at failure developed by these two indenters.

Figure 8 shows that the concentrated load developed in the yarn could be predicted by the quasi-static circular curved beam theory when the yarn was loaded transversely by indenters with a radius

of curvature larger than 1.59 mm. The model assumed the concentrated load in the fibers was caused by the additional stretching of the fibers due to bending. Thus, the failure surface should only reveal fibrillation without other failure mechanisms. Unlike large indenters, when the yarn was loaded with indenters smaller than 1.59 mm, localized shear and kink-band were observed in the recovered fibers. Since a quasi-static circular curved beam did not account for such failures, the experimental data was not in agreement for indenters possessing a radius of curvature smaller than 1.59 mm.

3.6 Conclusions

Quasi-static transverse loading experiments on Twaron® 2040 warp yarns were performed to study the stress concentration developed in the yarns. The results showed that the stress concentration decreased as the radius of curvatures of the indenter increased. Post-mortem failure analysis revealed the failure surfaces changed from combination of fibrillation, snapped-back, kink band, and localized shear to only fibrillation as the radius of curvature increased. For the cases where the radius of curvature of the indenter was smaller than 1.59 mm, the residual strain energy from the strain energy model scale linearly with the radius of curvature of the indenter. Finally, the quasi-static circular curved beam theory was utilized to predict the stress concentration induced by the indenters with a radius of curvature larger than 1.59 mm.

CHAPTER 4. CRITICAL VELOCITY OF HIGH-PERFORMANCE YARN TRANSVERSELY IMPACTED BY RAZOR BLADE

(A version of this chapter has been published in Fibers [8])

4.1 Abstract

A ballistic parameter that influences the ballistic performances of a high-performance yarn is the critical velocity. The critical velocity is defined as the projectile striking velocity that causes instantaneous rupture of the yarn upon impact. In this study, we performed ballistic experiments to determine the critical velocity of a Twaron® yarn transversely impacted by a razor blade. A high-speed camera was integrated into the experimental apparatus to capture the in-situ deformation of the yarn. The experimental critical velocity demonstrated a reduction compared to the critical velocity predicted by the classical theory. The high-speed images revealed the yarn specimen failed from the projectile side toward the free end when impacted by the razor blade. To improve the prediction capability, the Euler–Bernoulli beam and Hertzian contact models were used to predict the critical velocity. For the Euler–Bernoulli beam model, the critical velocity was obtained by assuming the specimen ruptured instantaneously when the maximum flexural strain reached the ultimate tensile strain of the yarn upon impact. On the other hand, for the Hertzian contact model, the yarn was assumed to fail when the indentation depth was equivalent to the diameter of the yarn. The errors between the average critical velocities determined from experiments and the predicted critical velocities were around 19% and 48% for the Euler–Bernoulli beam model and Hertzian contact model, respectively.

Keywords: high-performance fiber; critical velocity; Smith theory; Euler–Bernoulli beam; Hertzian contact

---

4.2 Introduction

The critical velocity is defined as the projectile striking velocity that causes instantaneous rupture of the specimen under transverse impact. When impacted at or above the critical velocity, the transverse displacement of the specimen is insignificant prior to failure [3, 4]. The classical theory

developed by Smith *et al.* [4] enabled some of the mechanical properties, such as transverse wave speed and critical velocity, to be predicted using only the axial mechanical properties. In general, the predicted transverse wave velocity using the classical theory is in good agreement with that obtained from the experiments [11, 12]. However, the Smith theory always overestimates the critical velocity [6, 20, 29].

Several studies were performed in an effort to understand why such discrepancies exist between the critical velocity determined from the Smith theory and experiments. For example, Bazhenov *et al.* [29] shot a 3-cm spherical metal ball with a striking velocity of 670 m/s into an aramid yarn. These specimens fractured at a striking velocity lower than the theoretical critical velocity. The authors suggested that the non-linear constitutive material properties of the yarns at a large deformation caused the theoretical critical velocity to be overestimated [29]. In addition, the authors also pointed out that non-linear interaction between the projectile and specimen caused the yarn to rupture at a lower critical velocity [29].

Chocron *et al.* [11, 20] studied the wave propagation developed in yarns impacted by flat head projectiles such as the fragmented simulating projectile (FSP) and the right circular cylinder. The authors suggested the reason that the Smith theory overestimated the critical velocity was that the specimen "bounced-off" the face of a flat head projectile [11, 20]. When a yarn was impacted by a flat head projectile, two waves were generated at both edges of the projectile and propagated toward the center of the projectile [11]. The superimposed waves caused the transverse particle velocity to double. This phenomenon caused the yarn to bounce off the face of the projectile and ultimately led to the decrease in critical velocity [11]. Such phenomenon was also observed experimentally by Field and Sun [12].

Recently, Hudspeth *et al.* [3, 5, 6] suggested that the reduction in the critical velocity was caused by the multi-axial stress developed in the yarns during transverse impact. Kevlar® KM2, Dyneema® SK76, and AuTx® yarns were loaded in the transverse direction under quasi-static conditions using a universal material testing machine (MTS 810) with three different projectiles: razor blade, 0.30-cal FSP, and 0.30-cal round [3, 6]. The axial rupture strain determined from quasi-static transverse loading experiments for all three projectiles showed a demonstrative

reduction compared to the ultimate tensile strain, with the razor blade being the lowest, followed by 0.30-cal FSP and 0.30 round projectiles [3, 6]. For the FSP projectile, most of the fibers failed at the corners, suggesting that multi-axial stress was developed and caused the stress concentration to occur at the corners [6]. Based on these studies, the authors suggested that a possible way to improve the Smith model was to substitute the ultimate tensile strain in the Smith theory with the rupture strain determined from quasi-static transverse loading experiments [6]. In addition, a 20-mm powder gun was utilized to determine the critical velocities of yarns impacted by these three projectiles [3]. The results showed that the yarns impacted by a razor blade had the lowest critical velocity, followed by 0.30-cal FSP and 0.30-cal round [3].

Clearly, the projectile nose shape is an important parameter that influences the critical velocity. The projectile–yarn interaction during transverse impact creates multiaxial loads on the yarn and generates additional waves such as the flexural wave [18, 19, 21]. These phenomena were not considered in the Smith theory, causing the predicted critical velocity to be overestimated. In this study, we performed ballistic experiments to determine the critical velocity for a Twaron® yarn impacted by a razor blade. In addition, we improved the prediction capability by using two different models, the Euler–Bernoulli beam model and the Hertzian contact model, to predict and compare the critical velocity with the experimental results.

4.3 Materials and Methods

The yarn specimens used in this study were strands of Twaron® 2040 yarns extracted from plain weave single ply CT 709 Twaron® in the warp direction. The quasi-static mechanical properties of this yarn were determined in previous studies and are tabulated in Table 3 [7, 30].

Table 3: Mechanical properties of Twaron® 2040 yarn and the razor blade. The mechanical properties of Twaron® 2040 were adapted from [7, 30, 31].

Properties	Value
Number of filaments in a single yarn	1000
Fiber diameter [μm]	9
Density, ρ_y [kg/m3]	1440
Yarn Young's modulus, E [GPa]	92.55

Table 3 continued

Yarn ultimate tensile strength, σ_{UTS} [GPa]	2.47
Yarn ultimate tensile strain, ε_{UTS} [%]	2.71
Yarn dynamic transverse modulus, E_t^y [GPa]	3.45
Razor blade Young's modulus, E_s [GPa]	200
Razor blade radius of curvature, R_s [µm]	2
Projectile mass, Ms [g]	28.4

4.3.1 Ballistic Experiments

A gas/powder gun was designed and developed to perform the ballistic experiments as shown in Figure 13a.

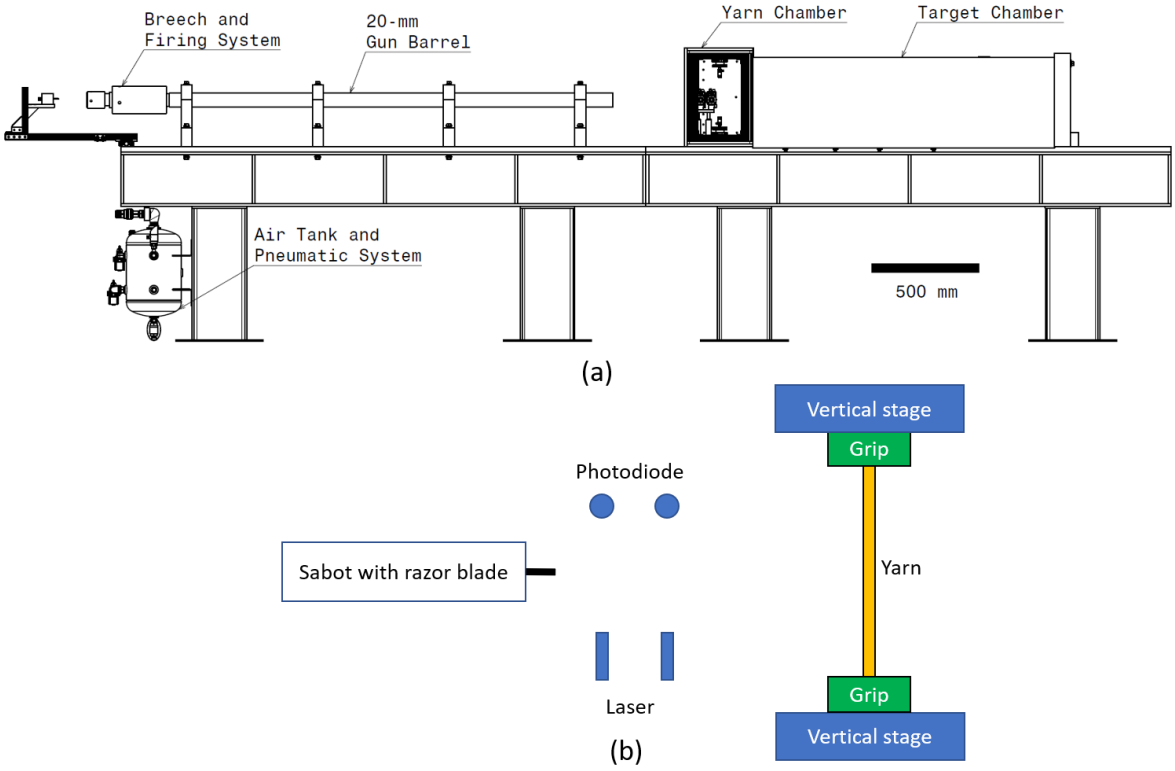

Figure 13: Experimental apparatus for ballistic experiments: (a) the ballistic experimental setup and (b) schematic inside the yarn chamber.

The apparatus consisted of a gun barrel, a target chamber, and a yarn chamber. The gun barrel possessed an inner diameter of 20 mm and a length of 2.1 m. Figure 13b presents the schematic inside the yarn chamber, which included a pair of lasers and photodiodes to measure the projectile

striking velocity. The method of attaching the yarn specimens to the grips was presented in [7] with the exception that the grips were mounted vertically instead of at 45 degrees. The Twaron® 2040 warp yarns possessed a gage length of 190 mm. Two vertical stages were used to assist in positioning the yarns as shown in Figure 13b. The projectiles used in these experiments were commercially available razor blades. The razor blades were cut to a length of 16.5 mm using a precision wafering saw. Sabots were used to ensure the razor blade fitted in the gun barrel, as shown in Figure 14a.

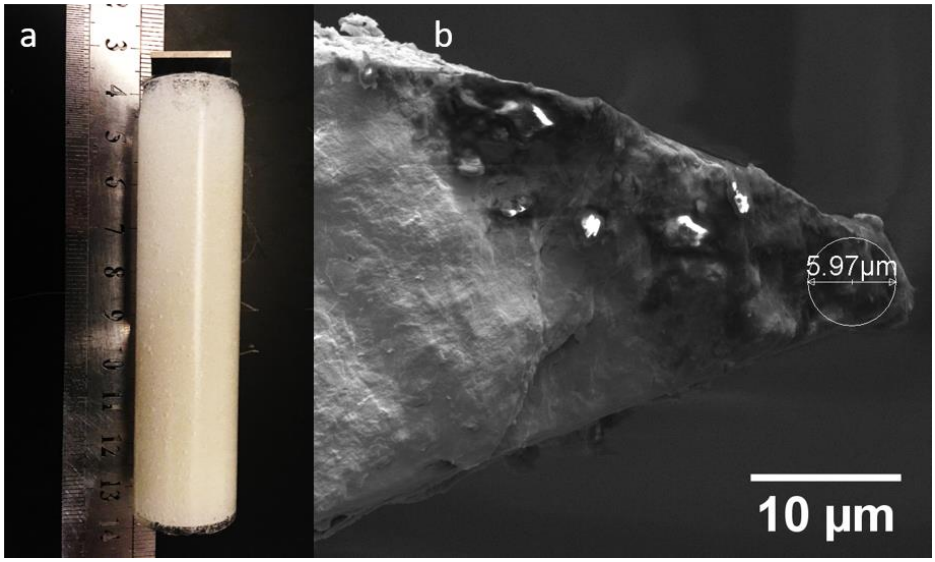

Figure 14: The razor blade projectile: (a) the razor blade with the sabot and (b) the scanning electron microscopy image at the tip of the razor blade to determine the radius of curvature. Note that for this specific case, $2R_s = 5.96$ µm.

The sabots were made by casting polyurethane foam in a mold. A slot was cut at the top of each sabot using a precision wafering saw. The purpose of this slot was to allow the razor blade to be placed on top of the sabot which was then secured on the sabot with cyanoacrylate adhesive. Another parallel cut was made at the rear end of the sabot to help align the sabot inside the gun barrel. Such an alignment ensured the contact angle between the blade and the yarn remained perpendicular. The razor blade was made of steel and the average mass of a sabot together with a razor blade (M_s) was 28.4 g. The radius of curvature of the razor blade was obtained via scanning electron microscopy (SEM) at three different locations. Figure 14b shows a representative SEM image of the radius of curvature of a razor blade. The average radius of curvature of the razor blade (R_s) was 2 µm. Compressed gas was used as a propellent when the projectile striking velocity was below 120 m/s. To achieve a higher striking velocity, smokeless gun powders were used. Finally,

a high-speed camera was integrated into the experimental apparatus to capture the in-situ dynamic impact event of the yarn subjected to a razor blade.

4.3.2 Euler–Bernoulli Beam Model

A possible reason for the Smith theory to overestimate the critical velocity is that the theory assumes bending is negligible [7, 18, 19]. Later in the results section, we showed that when the yarn was impacted by a razor blade above the critical velocity, the yarn deflection was small prior to rupture. In addition, the length of the specimen was much larger than the diameter. These criteria satisfied two of the assumptions in the Euler–Bernoulli beam theory [13]. Thus, we modeled the specimen as a Euler–Bernoulli beam with infinite length subjected to transverse impact by a pointed projectile. A Cartesian coordinate was setup with x = 0 at the impact location. Using Euler–Bernoulli beam theory with the assumption that damping in the specimen is negligible the equation of motion of a free vibration beam is given in Equation 10 [13]

$$EI_y \frac{\partial^4 v_y}{\partial x^4} + \rho_y A_y \frac{\partial^2 v_y}{\partial t^2} = 0 \qquad \text{Eqn. 10}$$

where v_y, I_y, ρ_y and A_y are transverse displacement, second moment of inertia, density, and cross-sectional area, respectively. Utilizing spectral analysis [13], the solution for Equation 10 has the form of

$$v_y(x,t) = \left(\boldsymbol{A}e^{-i\beta x} + \boldsymbol{B}e^{-\beta x} + \boldsymbol{C}e^{i\beta x} + \boldsymbol{D}e^{\beta x}\right)e^{i\omega t}$$

$$\beta = \sqrt[4]{\frac{\rho_y A_y}{EI_y}}\sqrt{\omega} \qquad \text{Eqn. 11}$$

where ω is the angular frequency. $\boldsymbol{A}$, $\boldsymbol{B}$, $\boldsymbol{C}$, and $\boldsymbol{D}$ are the integration constants. Equation 11 describes the two transverse waves propagating in the specimen when subjected to a point disturbance, a right running wave (v_y^i) and a left running wave (v_y^r), as shown in Equation 12 [13].

$$v_y^i(x,t) = \left(\boldsymbol{A}e^{-i\beta x} + \boldsymbol{B}e^{-\beta x}\right)e^{i\omega t}$$

$$v_y^r(x,t) = \left(\boldsymbol{C}e^{i\beta x} + \boldsymbol{D}e^{\beta x}\right)e^{i\omega t} \qquad \text{Eqn. 12}$$

The first terms in Equations 12a and 12b are wave solutions and the second terms are predominantly spatial damped vibrations [13]. The integration constant could be evaluated by imposing a symmetric boundary condition at the impact location as given in Equation 13.

$$v_y^i(0,t) = v_y^r(0,t)$$

$$\frac{\partial v_y^i}{\partial x}(0,t) = \frac{\partial v_y^r}{\partial x}(0,t) = 0 \qquad \text{Eqn. 13}$$

The transverse particle velocity ($\dot{v}_y^i$) and bending strain (ε_{xx}) developed in the specimen is defined as:

$$\dot{v}_y^i(x,t) = \frac{\partial v_y^i}{\partial t}$$

$$\varepsilon_{xx}(x,y,t) = -y\frac{\partial^2 v_y^i}{\partial x^2}. \qquad \text{Eqn. 14}$$

From Equations 12 - 14 at the impact location (x = 0), the particle velocity and bending strain are related by Equation 15.

$$\dot{v}_y^i(0,t) = \frac{1}{y}\sqrt{\frac{EI_y}{\rho_y A_y}}\,\varepsilon_{xx}(0,y,t) \qquad \text{Eqn. 15}$$

When the specimen is impacted by the razor blade at the impact location, the yarn moves with a transverse particle velocity equivalent to projectile striking velocity (i.e., $\dot{v}_y^i(0,t) = V_s$). It was assumed that the specimen would rupture if the bending strain reached the ultimate tensile strain. Hence, if the ultimate tensile strain of the yarn was known, the projectile critical striking velocity (V_{crit}) that would cause instantaneous rupture of the yarn could be determined from Equation 16.

$$V_{crit} = \frac{1}{y}\sqrt{\frac{EI_y}{\rho_y A_y}}\,\varepsilon_{UTS} \qquad \text{Eqn. 16}$$

Furthermore, it was assumed that the yarn possessed a circular cross-section and the interactions between fiber–fiber were negligible. For a specimen with a circular cross-section, the maximum

bending strain occurs at y = r. From Equation 16, with y = r, the critical velocity is given in Equation 17,

$$V_{crit} = \frac{1}{2} C_0 \varepsilon_{UTS} \qquad \text{Eqn. 17}$$

where $C_0 = \sqrt{E/\rho_y}$ is the axial wave speed. The predicted critical velocity obtained from the Euler–Bernoulli model was then compared with the experimental results.

4.3.3 Hertzian Contact Model

A common issue in the Smith model [4] and the Euler–Bernoulli beam model is that the critical velocity only depends on the mechanical properties of the yarn. However, experimental results revealed that the critical velocity was highly dependent on the projectile nose shape [3, 7]. As the projectile radius of curvature decreased, the critical velocity also decreased [3]. Therefore, in this model, we considered the projectile–yarn interaction and modeled the projectile and the yarn as a rigid sphere and Euler–Bernoulli beam, respectively. Figure 15 presents a free body diagram of a yarn impacted by a spherical projectile. Upon impact, a contact force (P) was generated and acted on both the projectile and the yarn.

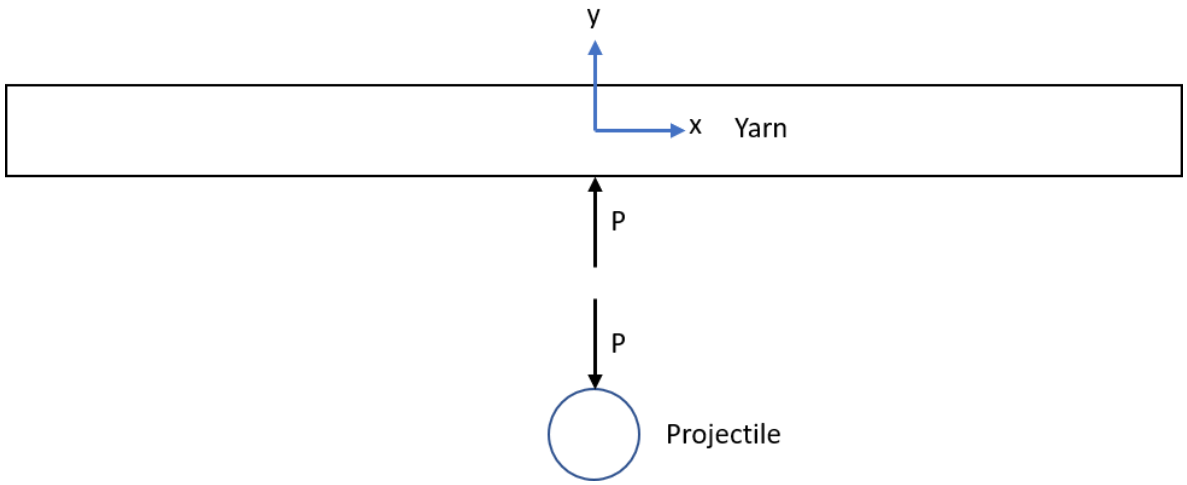

Figure 15: Free body diagram of a yarn (as a flat beam) impacted by a spherical projectile.

For a rigid body sphere possessing a mass (Ms) subjected to a contact force (P), the equation of motion is given in Equation 18,

$$M_s \ddot{v}_s = -P \qquad \text{Eqn. 18}$$

where vs is the displacement of the spherical projectile (in the y-direction) upon impact. For a dynamic Euler–Bernoulli beam possessing an infinite length, the relationship between the transverse velocity and load P at the point of impact (x = 0) is given in Equation 19 [13, 32].

$$\dot{v}_y = \frac{1}{2\sqrt{2\pi}\left(E_y I_y\right)^{\frac{1}{4}}\left(\rho_y A_y\right)^{\frac{3}{4}}} \int_0^t \frac{P(\tau)}{\sqrt{t-\tau}} d\tau \qquad \text{Eqn. 19}$$

We neglected the fiber–fiber interaction by assuming the yarn possessed a cross section with the shape of a circle and a cross-sectional area equal to the sum of the cross-section of all the fibers in the yarn. Upon impact, the contact force can be related to the displacement of the projectile and the transverse deflection of the beam using the Hertzian contact law as given in Equation 20 [32, 33].

$$P = K\left(v_s - v_y\right)^{\frac{3}{2}}$$

$$K = \frac{4}{3} E^* \sqrt{R}$$

$$E^* = \left(\frac{1}{E_s} + \frac{1}{E_t^y}\right)^{-1} \qquad \text{Eqn. 20}$$

$$R = \left(\frac{1}{R_s} + \frac{1}{R_y}\right)^{-1} \approx R_s$$

where E_s, and E_t^y are the Young's modulus of the sphere (projectile) and transverse modulus of the beam (yarn), respectively. Twaron® is a p-phenylene terephthalamide (PPTA) fiber where the mechanical properties in the axial direction are relatively rate-insensitive [16]. However, the transverse mechanical properties are rate sensitive [31]. The dynamic transverse modulus of Twaron® 2040 yarn or fiber has not yet been determined. Therefore, in this study, we assumed that the transverse modulus of the yarn is equivalent to the dynamic transverse modulus of the fiber. Experimental work performed by Guo *et al.* [31] indicated that at high-rate, the dynamic transverse

modulus for PPTA fiber increased by 2.95 times compared to that of the quasi-static. Therefore, in this study, it was assumed that the transverse modulus for Twaron® 2040 yarn also increased by a similar order of magnitude [30, 31]. The projectile was made from steel with a Young's modulus of 200 GPa. R_y is the radius of curvature of the yarn. Upon impact, the yarn remained flat, resulting in an infinite radius of curvature ($R_y = \infty$). Equations 18 and 19 are the equations of motion for a beam impacted by a spherical projectile. Note that Equation 19 is valid only at x = 0. The initial conditions for these equations of motion are

$$v_s(0) = 0$$

$$\dot{v}_s(0) = V_s \qquad \text{Eqn. 21}$$

$$v_y(0) = 0$$

where V_s is the projectile's striking velocity. Equations 18 - 21 were solved numerically using the finite difference method with the time step of 1 ns and 10,000 steps. The equations of motion were converted into a system of first order differential equations. First order forward differencing was implemented on the initial condition to obtain the solution for the initial time step [34]. For other time steps, a central differencing scheme, which is second order accurate in time, was used to formulate explicit equations to solve these differential equations.

4.4 Results

4.4.1 Ballistic Experiments

Ballistic experiments were performed to determine the critical velocity when the Twaron® yarn was transversely impacted by a razor blade. When a projectile impacts a yarn transversely, the critical velocity has a range [3]. Below the low end of the critical velocity, the yarn is not ruptured. Above the higher end of the critical velocity, the yarn ruptures immediately. The yarn is partially ruptured when impacted within the critical velocity range. Figure 16 shows the high-speed images when the yarn was impacted at (a) below, (b) within the range of, and (c) above the critical velocity.

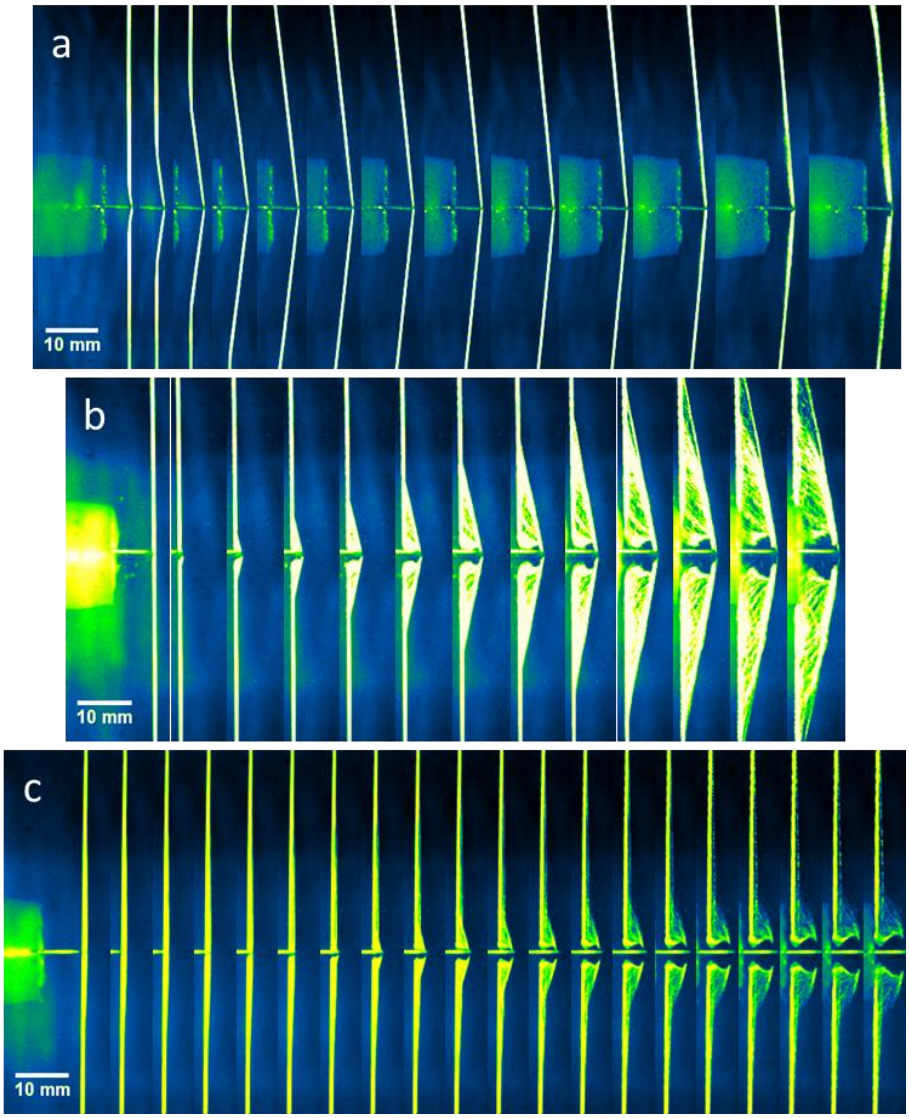

Figure 16: High-speed images of a Twaron® yarn impacted by a razor blade: (a) below critical velocity, (b) within the range of critical velocity and (c) above critical velocity. The striking velocities of the razor blade were (a) 52 m/s, (b) 135 m/s and (c) 247 m/s. The times between each frame were (a) 20 µs, (b) 5 µs and (c) 1.5 µs.

When the yarn was transversely impacted by a razor blade, the initial deformation of the yarn fell into one of the three possible cases; instantaneous rupture, partial rupture or no rupture, as shown in Figure 16. When impacted below the critical velocity, a transverse wave was observed to propagate in the yarn, causing the yarn to deform into a triangular shape very similar to the deformation described by Smith *et al.* [4]. As the striking velocity increased, some of the fibers ruptured upon contact. The fibers that did not rupture deformed into a triangular shape similar to the deformation at low velocity. When the projectile impacted at a velocity higher than the critical

velocity, the yarn ruptured instantaneously. The transverse displacement of the yarn prior to the failure was insignificant as compared to the previous two cases. Although visually distinguishable, it is important to note that such a method to determine the case each experiment falls into is qualitative in nature [3]. Interestingly, from Figure 16, the fibers of the yarn were observed to fail progressively from the razor blade side to the other free end. Figure 17 plots the yarn condition upon impact versus the striking velocity.

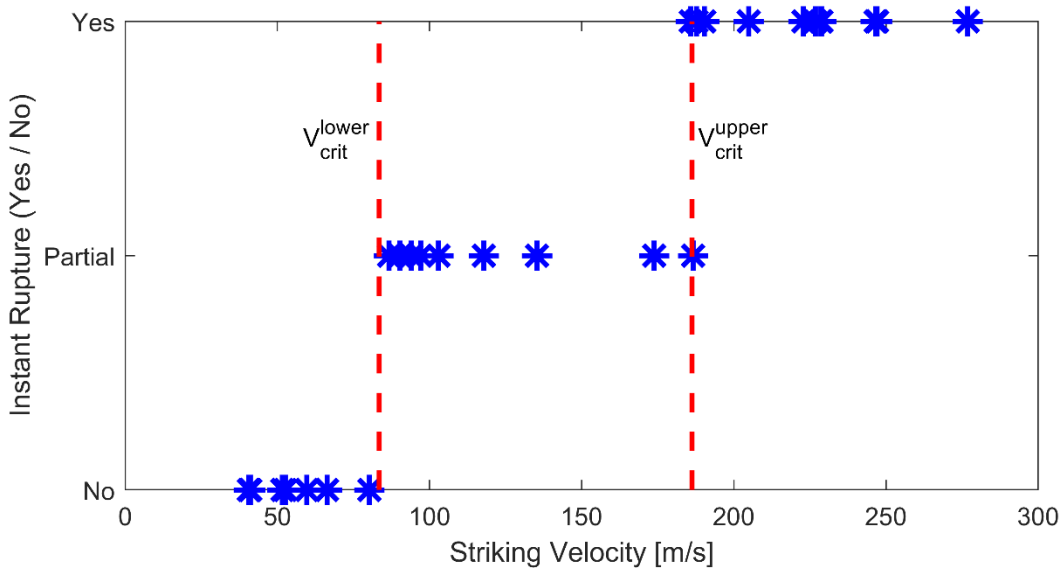

Figure 17: Experimental results for a razor blade impacting Twaron® yarn at different striking velocities.

From Figure 17, some fibers were partially ruptured upon impact at a striking velocity between 83 m/s and 186 m/s. These boundaries indicated the lower and upper limits of the critical velocity for the Twaron® yarns transversely impacted by a razor blade. Such a method to determine the critical velocity was very similar to those reported by Hudspeth *et al.* [3].

4.4.2 Hertzian Contact Model

Figure 18 shows the velocity histories for both projectile and yarn at the point of impact at several striking velocities ranging from 50 m/s to 250 m/s. These results were obtained by solving Equations 18 - 21 using the parameters listed in Table 3. Since the mass of the projectile was significantly heavier compared to the yarn, the projectile velocity remained nearly constant throughout the event. Initially, the yarn was at rest. Once the yarn was impacted, the velocity at the point of impact increased and even surpassed the projectile's striking velocity. Eventually, the

yarn velocity decreased and reached the projectile's striking velocity, causing the projectile and the yarn to move at the same speed.

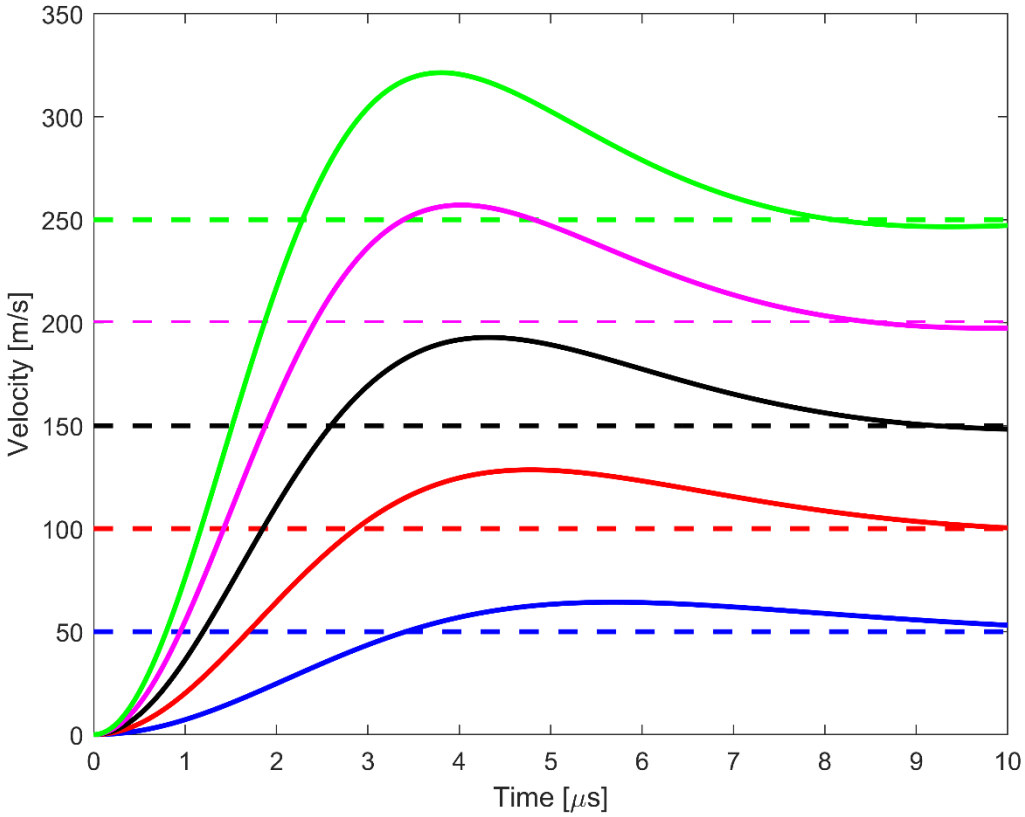

Figure 18: Velocity histories for a yarn impacted by a razor blade predicted by the Hertzian model at the point of impact. The dashed lines represent the razor blade velocities and the solid lines represent the yarn velocities. The projectile initial striking velocities are 50 m/s, 100 m/s, 150 m/s, 200 m/s and 250 m/s for blue, red, black, pink and green curves, respectively.

The normalized indentation depth (α) is defined as the difference between the projectile and yarn displacements normalized by the yarn diameter ($2r_y$) as given in Equation 22.

$$\alpha = \frac{v_s - v_y}{2r_y} \qquad \text{Eqn. 22}$$

Figure 19 shows the normalized indentation depth at several striking velocities. Initially, the projectile and yarn displacements were zero, resulting in zero indentation depth. Since the yarn required a finite amount of time to reach the projectile striking velocity, the indentation depth increased initially. As the velocity of the yarn exceeded the projectile striking velocity, the

indentation depth decreased. Since the projectile displacement was higher than the yarn displacement, the indentation depth did not reduce to zero. Finally, as the yarn velocity approached the projectile striking velocity, the normalized indentation depth reached a plateau when the two velocities converged, as shown in Figure 19.

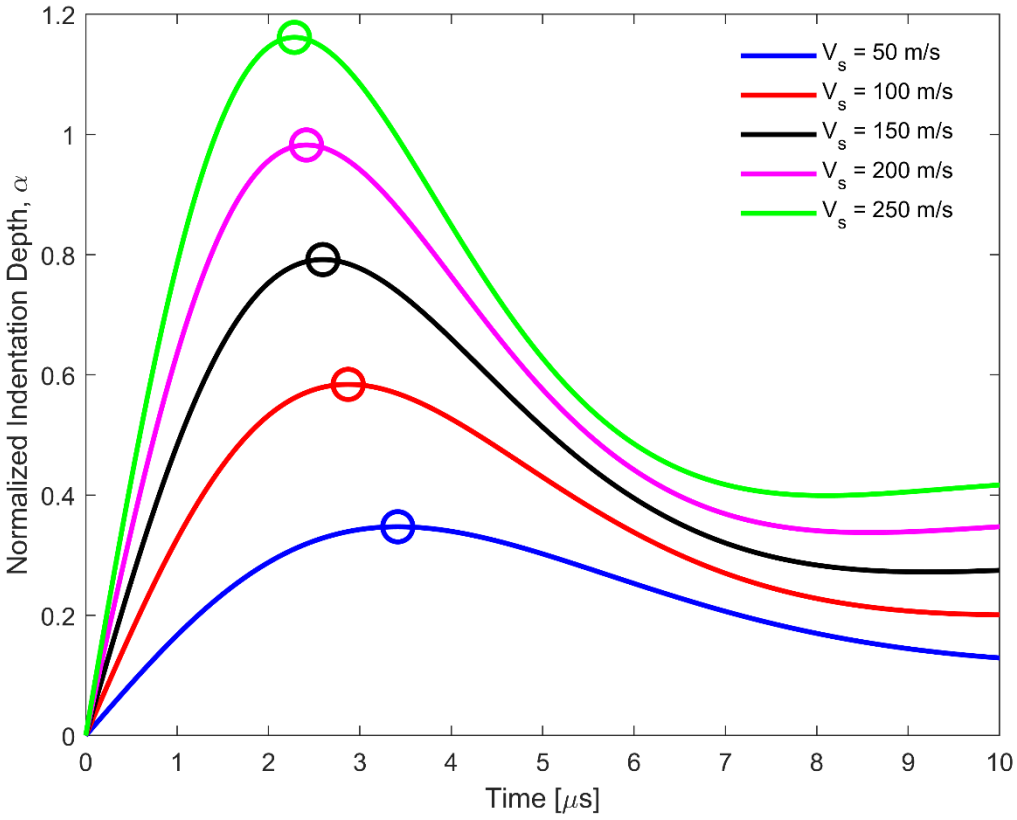

Figure 19: Normalized indentation depth histories for a Twaron® 2040 yarn impacted by a razor blade at different striking velocities predicted by the Hertzian contact model. The circle markers indicate the maximum normalized indentation depth for each case.

As the projectile's striking velocity increased, it was observed that the normalized indentation depth also increased. At a striking velocity below 200 m/s, the normalized indentation depth was less than unity. Physically, this means that the projectile was behind the yarn for all time, and the transverse displacement of the yarn at the point of impact would increase to a point that violates the assumption of small deformation in the Euler-Bernoulli beam theory, meaning the yarn would deform according to the Smith theory.

However, at a striking velocity above 200 m/s, it was observed that the normalized indentation depth was more than unity. A normalized indentation depth of more than unity means the projectile was ahead of the yarn. Physically, this means that the projectile sheared through the yarn and caused the yarn to fail, which was very similar to that observed in Figure 3c. When the projectile strikes at 200 m/s, the Hertzian contact model revealed that the maximum indentation depth was around 0.98, which was very close to unity. Therefore, the striking velocity of 200 m/s was the critical velocity for Twaron® 2040 yarn impacted by a razor blade predicted by the Hertzian contact model.

4.5 Discussion

The critical velocity obtained from the experiments, Euler–Bernoulli beam model, Hertzian contact model, and Smith model were compared, as shown in Figure 20.

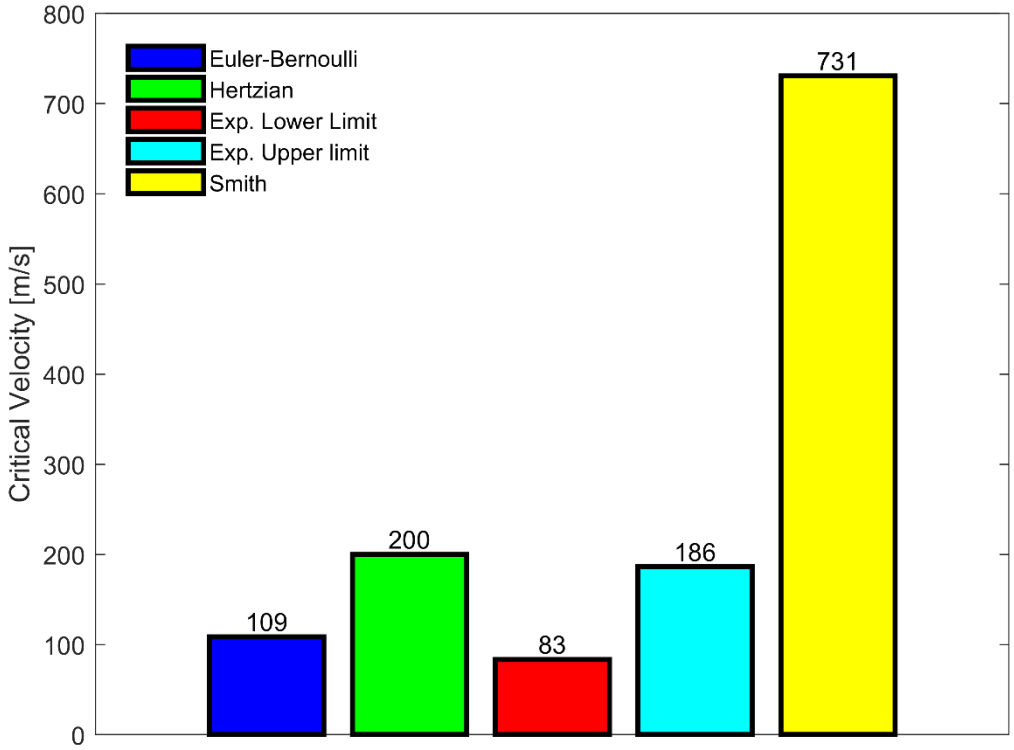

Figure 20: Critical velocities for a Twaron® yarn impacted by a razor blade determined from the Euler–Bernoulli model, Hertzian contact model, experimental results, and Smith theory.

For the Smith theory, the predicted critical velocity (V_{Smith}) could be obtained by using Equation 23 [4, 6].

$$V_{Smith} = C_0 \sqrt{\varepsilon_{UTS}(1+\varepsilon_{UTS}) - \left(\sqrt{\varepsilon_{UTS}(1+\varepsilon_{UTS})} - \varepsilon_{UTS}\right)^2} \qquad \text{Eqn. 23}$$

Using the mechanical properties listed in Table 3, the critical velocity predicted from the Smith theory was around 731 m/s. The predicted critical velocity overestimated the experimental results by at least 290%. Such a discrepancy in critical velocity agreed with the experimental results reported in the literature [3, 29].

On the other hand, for the Euler–Bernoulli beam model, the predicted critical velocity using Equation 17 is 109 m/s. From Figure 20, it was observed that the predicted critical velocity agreed well with the experimental results, especially when predicting the lower limit of the critical velocity. The Euler–Bernoulli model assumed that the yarn failed instantaneously when the maximum bending strain reached the ultimate tensile strain. Physically, this means that only one fiber located near the free end would fail; as a result, the predicted critical velocity was closer to the lower end. From the high-speed images presented in Figure 4, the fiber failed progressively from the razor blade toward the other free end. However, for the Euler–Bernoulli beam theory, the maximum bending strain occurred at the free end. The failure should also initiate from the free end, which contradicted to what was observed experimentally. To address such an issue, we used the Hertzian contact theory to model the projectile–yarn interaction and predict the critical velocity.

Unlike the Smith model and the Euler–Bernoulli beam model, the Hertzian contact model accounts for the projectile–yarn interaction. In addition, the failure criterion implemented in the Hertzian contact theory required all the fibers in a yarn to fail. As a result, the predicted critical velocity agreed well with the upper limit of the critical velocity, as shown in Figure 20.

To have a better comparison between the models, the errors between the predicted critical velocities from the Smith, Hertzian contact and Euler–Bernoulli models and the average critical velocity determined from experiments were determined. These errors were 440%, 48%, and 19% for the Smith, Hertzian contact and Euler–Bernoulli models, respectively. Even though the Euler–

Bernoulli beam model had the lowest error, the failure mechanism predicted by this model did not agree with the observations from the high-speed images. On the other hand, the Hertzian contact model accounted for the projectile–yarn interaction. The failure criterion using indentation depth was formulated based on experimental observations. As a result, the predicted velocity was in good agreement with the experimental results.

4.6 Conclusions

Ballistic experiments were performed to determine the critical velocity that caused the yarn to fail instantaneously when impacted by a razor blade. The Euler–Bernoulli beam model and Hertzian contact model were used to predict the critical velocity. The Euler–Bernoulli beam assumed that the yarn failed instantaneously when the maximum bending strain reached the ultimate tensile strain. The predicted critical velocity from the beam model was closer to the lower limit of the critical velocity with an error of 31% between these two velocities. On the other hand, the Hertzian contact considered the projectile yarn interaction. The yarn was assumed to fail when the indentation depth was equal to the yarn's diameter. The predicted critical velocity was in good agreement with the upper limit of the experimental critical velocity, with an error of 7.5% between these two velocities.

CHAPTER 5. THE EFFECT OF PROJECTILE NOSE SHAPE ON THE CRITICAL VELOCITY OF HIGH-PERFORMANCE YARN

(A version of this chapter is under review in Fibers)

5.1 Abstract

In this study, ballistic experiments were performed to determine the critical velocity of a Twaron[e] 2040 high-performance yarn transversely impacted by round projectiles. Four different round projectiles possessing a radius of curvature of 2 μm, 20 μm, 200 μm and 2 mm were used in this study. Load cells were mounted to the grips to measure the load history of the yarn upon impact. A high-speed camera was incorporated into the ballistic experimental setup to capture the failure process of the yarn upon impact. Post mortem failure analysis was performed on the recovered specimens via scanning electron microscopy. The results showed that as the radius of curvature of the projectile increased, the critical velocity also increased. The critical velocities for all cases were bounded between those predicted from Euler-Bernoulli beam and Smith models. Upon impact above the upper limit of the critical velocity, the axial loads revealed a demonstrative reduction. The failure surfaces changed from shear to fibrillation as the radius of curvature increased. For those specimens that failed in shear, Hertzian contact model was used to predict the critical velocity.

Keywords: High-performance fiber; Critical velocity; Ballistic experiments; Projectile nose shape; Smith theory

---

5.2 Introduction

Projectile nose shape is an important parameter that dominates the ballistic performance of a high-performance fiber [3, 4, 35]. The critical velocity, a ballistic parameter, is defined as the projectile striking velocity that causes instantaneous failure on the yarn under transverse impact. Upon impact below the critical velocity, the transverse waves developed in the yarn would deform according to the Smith theory [4, 11, 12]. Such transverse speed can be determined analytically using the projectile's striking velocity and

the axial mechanical properties of the yarn [4, 11, 12]. On the other hand, if the projectile strikes above the critical velocity, the transverse displacement of the yarn is insignificant [3, 8]. Also, even though Smith theory is capable of predicting the critical velocity, the predicted result would always be overestimated compared to those obtained from experiments [3, 8, 29, 36].

A factor that caused the overestimation of the predicted critical velocity by the Smith theory is the projectile's nose shape [3, 35]. Hudspeth *et al.* [3] shot a razor blade, a 0.30-cal fragmented simulation projectile (FSP) and a 0.30-cal round onto high performance yarns and found out that 0.30-cal round has the highest critical velocity, followed by 0.30-Cal FSP and razor blade. The failure surface of the recovered specimens indicated the yarns impacted by razor blade failed in shear and the 0.30-cal round failed in fibrillation [3]. Multi axial load developed in the yarn during transverse impact caused stress concentration and ultimately influenced the critical velocity [21].

Carr [10] shot a spherical steel with a mass of 0.68 g onto para-aramid yarns and Dyneema® yarn. The failure surfaces of para-aramid yarns showed fibrillation irrespective of projectile's striking velocity [10]. However, for Dyneema® yarn, the failure was caused by shear when impacted below the critical velocity [10]. The failure surfaces for Dyneema® yarn revealed melting when impacted above the critical velocity which was similar to those observed by Hudspeth *et al.* [3, 10].

Utomo *et al.* [36, 37] performed single fiber aramid and ultra-high weight molecular Polyethylene (UHMWPE) impact experiments using saddle and cylindrical projectiles impacted to obtain the mechanical behavior. The results showed that the tensile modulus was independent of the projectile's striking velocity. The failure strains determined from the saddle projectile were higher than those obtained from the cylindrical projectile. However, both failure strains were lower than the quasi-static ultimate tensile strain [36].

Phoenix *et al.* [35] performed ballistic experiments on Dyneema® SK76 yarns with various initial pretension using two types of projectiles (flat and saddle noses). The results showed that as the initial pretension increased, the Young's modulus also increased. The critical velocity for the flat nosed projectile was lower compared to that of the saddle nose projectile. A wave-propagation

model was developed to predict the critical velocity for a flat nose projectile impacted onto yarns with various initial pretension.

To the best of our knowledge, the circular nose shape projectiles (round, saddle or spherical) used in most of the transverse impact experiments contained only one radius of curvature [10, 29, 35-37]. The only exception was the experimental work done by Hudspeth *et al.* [3] where a razor blade and a 0.30-cal round projectile were used. The razor blade used in their study can be considered as a round projectile with a radius of curvature of 1.15 µm [3]. The difference in radius of curvature between the razor blade and 0.30-cal round is at least 3 orders of magnitude. To understand the effect of projectile radius of curvature on the critical velocity, we performed ballistic experiments to determine the critical velocity of an aramid yarn transversely impacted by round projectiles with different radii of curvatures.

5.3 Material and Method

The aramid yarn specimens used in this study were strands of Twaron® 2040 yarns extracted from plain weave single ply CT 709 Twaron® in the warp direction. The quasi-static axial mechanical properties of the yarn were determined in a previous studies [7].

5.3.1 Ballistic Experiments

A gas/powder gun setup was utilized to perform the ballistic experiments to determine the critical velocity of the yarn as shown in Figure 21.

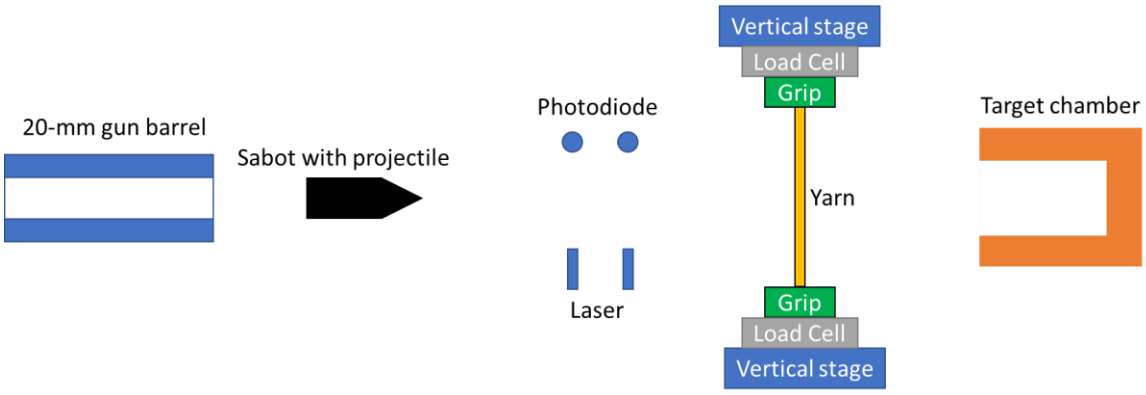

Figure 21: Experimental apparatus to determine the critical velocity.

The detail of the experimental setup including the method to attach the yarn was presented in previous studies [7, 8]. The load cells were mounted to the grips to measure the load history. Four different types of round projectiles were used in this study. These projectiles were razor blade, 20-µm round, 200-µm round, and 2-mm round. The razor blades used were commercially available razor blades. In the previous study, scanning electron microscopy (SEM) images revealed that the average radius of curvature of the razor blade was 2 µm [7]. The remaining three projectiles were custom made projectiles. The inner diameter of the gun barrel was larger than the projectiles. To fit these projectiles into the barrel sabots were used as shown in Figure 22.

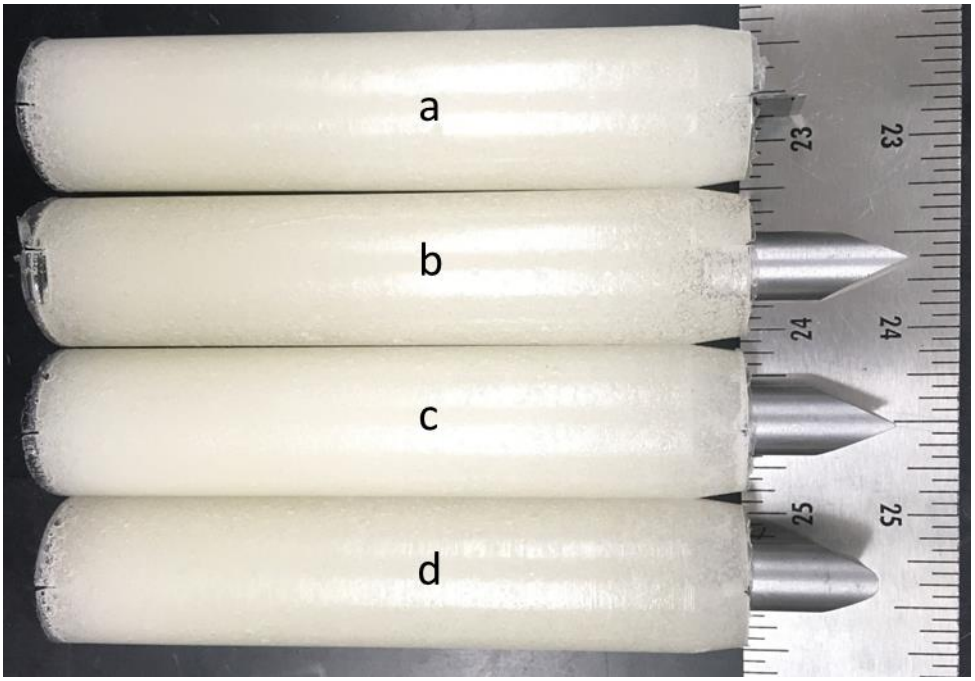

Figure 22: Round projectile with a radius of curvature of (a) 2 µm, (b) 20 µm, (c) 200 µm and (d) 2 mm

The sabots were made by polyurethane cast into a mold. An insert with a 9-mm hex shape was placed on top of the mold to fit different size projectiles except for the razor blade as shown in Figure 22. A slot was cut at the top of each sabot using a precision wafering saw. For the razor blade, the purpose of this slot was to allow the razor blade to be placed on top of the sabot as shown in Figure 22a. For the other types of projectiles, this slot was used to align the projectile to the sabot. These projectiles were then secured on the sabot with cyanoacrylate adhesive. Another parallel cut was made at the rear end of the sabot to assist in alignment of the sabot inside the gun barrel and to ensure the contact angle between the blade and the yarn was perpendicular. The

combination of sabot and projectile yield an average mass of 29 g for razor blade and 39 g for the other three types of projectiles. To observe the failure process of the yarn under transverse impact, a high-speed camera was integrated into the experimental setup.

5.4 Experimental Results

The critical velocities of Twaron® 2040 yarns upon transverse impact by four round projectiles were obtained via ballistic experiments. It is important to emphasis that for a given case, the critical velocity has a range. If the impact of the projectile on the yarn was below the lower limit of the critical velocity, the transverse waves would develop and propagate in the yarn, causing it to deform according to Smith theory [4, 8]. On the other hand, if impacted above the upper limit, the yarn would rupture instantaneously [3, 8]. When impacted within the range of the critical velocity, some of the fibers would rupture upon impact and the remaining fibers would deform into triangular shape as describe by Smith theory [3, 4, 8]. Therefore, when a yarn is transversely impacted by a projectile, the initial deformation of the yarn would fell into one of the three possible cases, (i) no rupture, (ii) partially rupture and (iii) instantaneously rupture [3, 8].

Figures 23-35 show the high-speed images when impacted below, between and above the critical velocities when impacted by 20 μm, 200 μm and 2 mm round projectiles. For those impacted by 2 μm round projectile, the high-speed images can be found in [8].

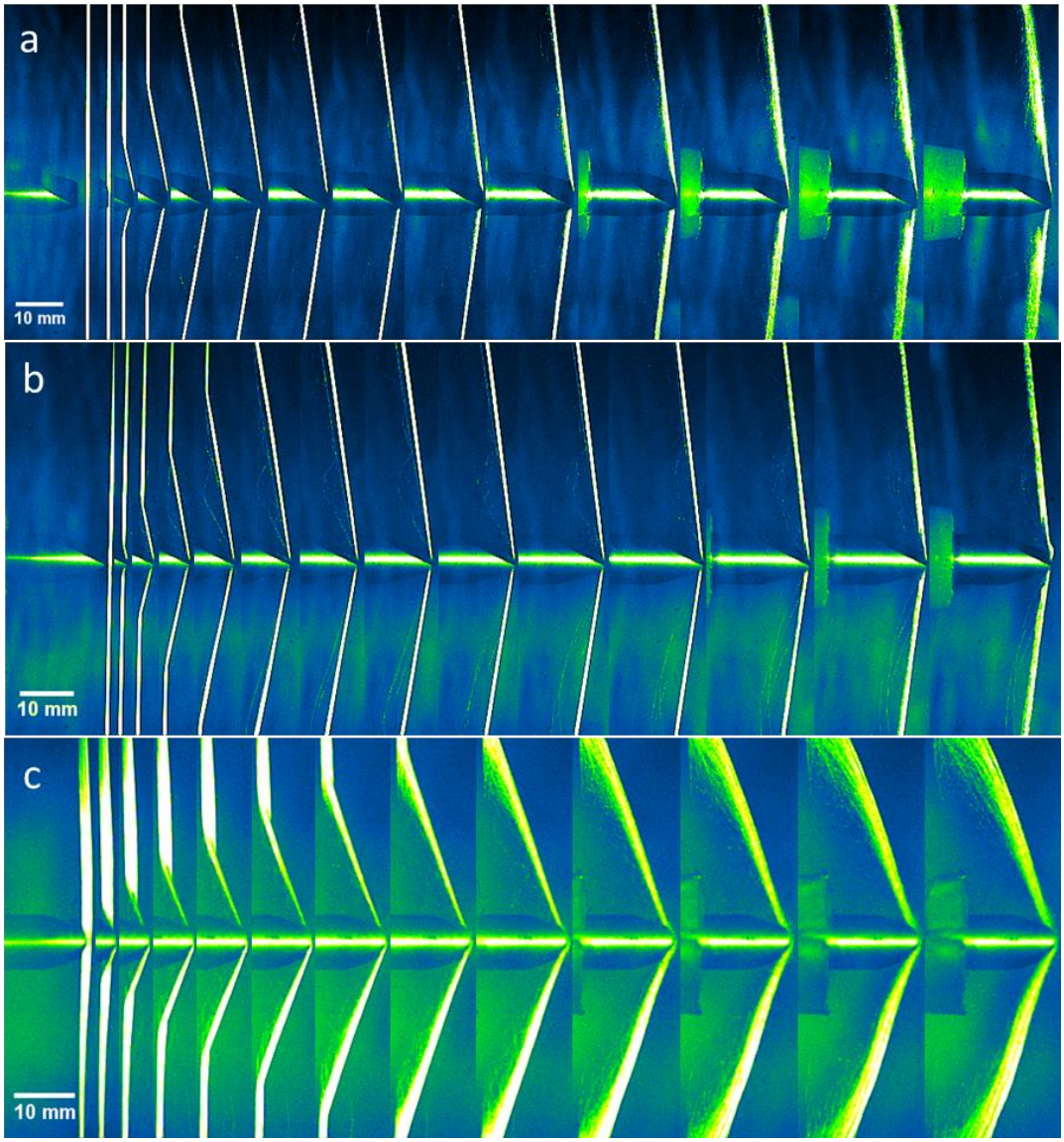

Figure 23: Deformation of yarn when transversely impacted by (a) 20 µm round, (b) 200 µm round and (c) 2 mm round projectiles at below the limit of their respective critical velocity. The projectile striking velocities were (a) 106 m/s, (b) 110 m/s and (c) 411 m/s. The time different between each frame were (a) 20 µs, (b) 15 µs and (c) 4 µs

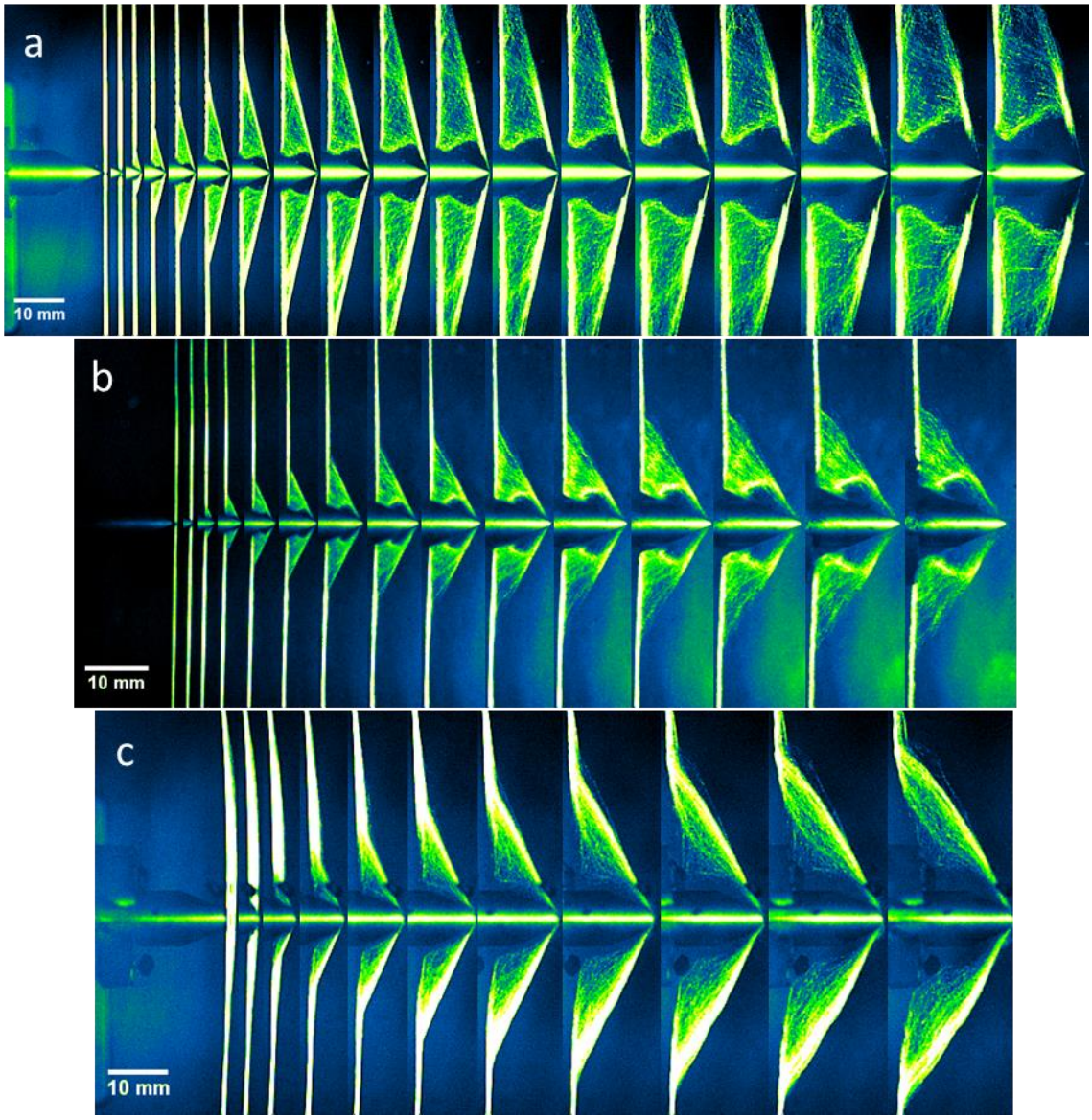

Figure 24: Yarn deformation when impacted by (a) 20 µm round, (b) 200 µm round and (c) 2 mm round projectiles between the limit of their respective critical velocity. The projectile stuck at (a) 218 m/s, (b) 458 m/s and (c) 474 m/s. The time different between each frame were (a) 5 µs, (b) 2.5 µs and (c) 4 µs

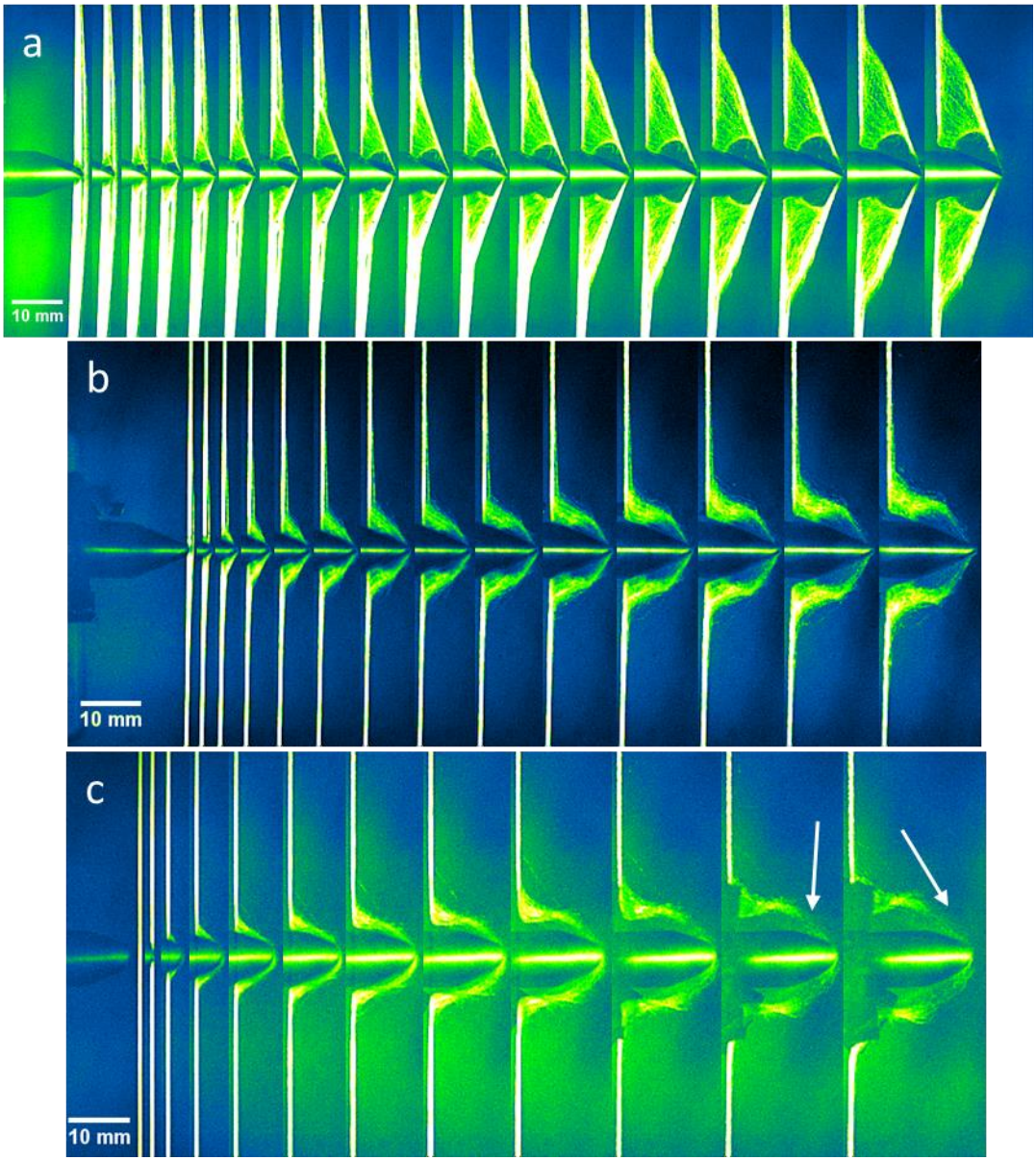

Figure 25: High-speed images when impacted by (a) 20 µm round, (b) 200 µm round and (c) 2 mm round projectiles above the critical velocity. The projectile stuck at (a) 343 m/s, (b) 552 m/s and (c) 649 m/s. The time different between each frame were (a) 2 µs, (b) 2 µs and (c) 3 µs.

From Figures 23-25, it was observed that as the radius of curvature of the projectile increased, the initial deformation of the yarn appeared to follow the contour of the projectile as opposed to triangular shape deformation as describe by Smith [4]. In addition, upon impact above the critical velocity, prior to rupture, the transverse displacement of the yarn increased as projectile's radius of curvature increased as shown in Figure 25. From Figure 25a, the transverse displacement of the

yarn at failure was small and occurred at the point of impact. Subsequently, as shown in Figure 25c, when impacted by a 2-mm round projectile, the transverse displacement of the yarn was larger than those impacted by smaller radius of curvature projectiles. Furthermore, the failure also initiated from a point away from the tips of the projectile as pointed by the arrows in Figure 25c. Figure 26 present the initial deformation of the yarn at various projectile striking velocity for all four cases.

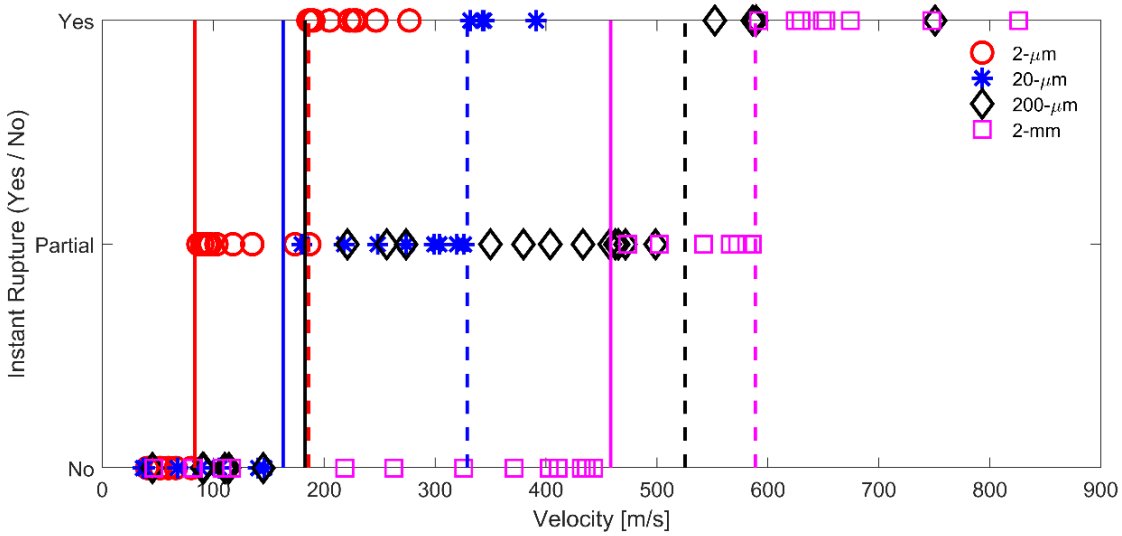

Figure 26: Yarn initial deformation when transversely impacted by (a) 2 µm round (b) 20 µm round (c) 200 µm round and (d) 2 mm round projectiles. Solid and dashed lines were the lower and upper limits of the critical velocities. The data for 2-µm round were adapted from [8].

The range of critical velocities for a Twaron® 2040 yarns transversely impacted by round projectiles possessing a radius of curvature of 2 µm, 20 µm, 200 µm and 2 mm were 83 m/s – 186 m/s, 163 m/s – 329 m/s, 183 m/s – 525 m/s and 458 m/s – 589 m/s, respectively. As pointed out in the previous study, the critical velocity predicted by Smith theory was around 731 m/s [4, 8]. Such a discrepancy between the predicted and experimental critical velocities for all cases agreed with the results reported in the literature [3, 29, 35, 36]. The load cells mounted to the grips allowed the force to be measured when the yarn specimen was subjected to transverse impact. Figure 27 plot the axial force at rupture versus the projectile striking velocity for Twaron® yarn impacted by 2 µm, 20 µm, 200 µm and 2 mm round projectiles. Such rupture load was obtained by averaging the loads from both load cells at failure.

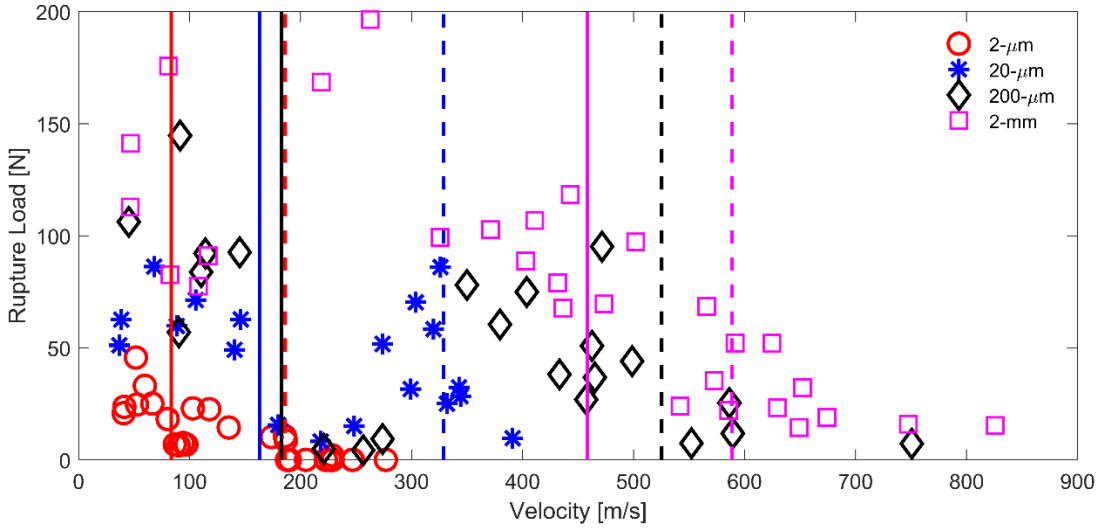

Figure 27: Axial load at rupture versus projectile striking velocity for a Twaron® 2040 yarn transversely impacted by (a) 2 µm round (b) 20 µm round (c) 200 µm round and (d) 2 mm round projectiles. Solid and dashed lines were the lower and upper limits of the critical velocities.

From Figure 27, it was observed that for a given striking velocity, the rupture load increased as the radius of curvature of the projectile increased. It is important to note that such rupture load is not equivalent to the axial load of the yarn when impacted below the lower limit of the critical velocity. The reason is that upon transverse impact below the critical velocity, the yarn deformed into triangular shape causing the axial load in the yarn to have both vertical and horizontal components. Since the load cells were only capable of measuring the vertical force, the axial force in the yarn was underestimated. For 2 µm and 20 µm cases, the rupture loads decreased as the projectile striking velocity approached its respective lower limit of the critical velocity. A possible reason is that these small projectiles were able to shear through the yarns causing them to fail progressively at the point of impact from projectile end toward the other free end. However, such failure process was not observed when impacted by larger round projectiles. The 2-mm round projectile was unable to shear through the yarn at low velocity suggesting that the yarn failed due to stretching which caused the axial rupture load to be highest among all cases.

Unlike the previous case, when impacted above the upper limit of the critical velocity, the transverse displacement of the yarn was small. In addition, the yarn remained vertical away from the point of impact. Therefore, the measured loads represented the axial load in the yarn. The rupture load showed a demonstrative reduction when impacted above the critical velocity. This

suggested that the load generated at the point of impact was unable to be transfer out by the stress waves causing stress concentration to develop in the yarn and ultimately led to premature failure [3, 5-7].

5.5 Discussion

In this section, the critical velocities predicted from several models will be compared to the experimental results. In additions, SEM was utilized to examine the failure surfaces of the recovered specimen.

5.5.1 Comparison between experiments and models

In the previous study, we used Euler-Bernoulli beam model and Hertzian contact model to improve the predictive capability of the critical velocity [8]. For the Euler-Bernoulli beam model, the yarn was modeled as a Euler-Bernoulli beam. An equation was formulated relating the transverse particle velocity with the bending strain [8, 13]. The critical velocity was then predicted by assuming the yarn failed instantaneously when the bending strain reached the ultimate tensile strain. For the Hertzian contact model, the projectile and yarn were modeled as a rigid sphere and Euler-Bernoulli beam respectively. The relationship between the contact load and deformation was described by the Hertzian contact theory [8, 33]. By neglecting the fiber-fiber interactions and assuming the cross section of the yarn was circular, the critical velocity was predicted by assuming the projectile shear through the yarn when the indentation depth was equal to the diameter of the yarn. The detail formulation on both models can be found in [8]. Figure 8 shows the critical velocities obtained from experiments, Smith model, Euler-Bernoulli model and Hertzian contact model [4, 8].

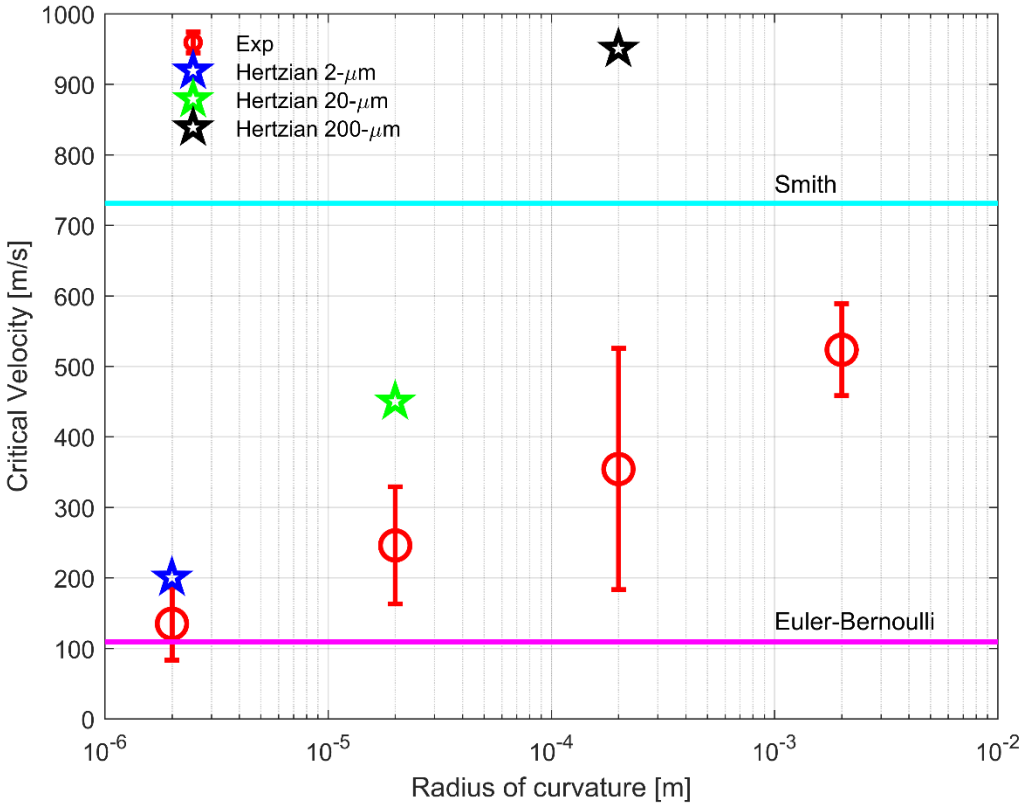

Figure 28: Comparison between experimental critical velocities with (a) Smith model [4, 8], (b) Euler-Bernoulli beam model [8] and (c) Hertzian contact model [8]. The error bars represented the lower and upper limit of the critical velocities.

From Figure 28, it was observed that the average critical velocities from experimental results fall between those predicted by the Euler-Bernoulli beam and the Smith model. The major difference between these two models is the Euler-Bernoulli beam model accounts for bending rigidity [8]. Smith theory overestimated the critical velocities from 442 % down to 40 % as the projectile radius of curvature increased from 2 μm to 2 mm. Conversely, Euler-Bernoulli beam model underestimated the critical velocities from 79 % to 19 % as the projectile's radius of curvature decreased from 2 mm to 2 μm. These results suggested that Euler-Bernoulli beam model can be used to predict the lowest limit of the critical velocity while Smith model can be used to predict the highest limit of the critical velocity. As pointed out from the previous study, the predicted critical velocities from the Euler-Bernoulli beam model and the Hertzian contact model agreed with those obtained from experiments for 2-μm round projectile as shown in Figure 8 [8]. The same Hertzian contact theory was used to predict the critical velocity for a 20-μm and a 200-μm round projectiles impacted onto the Twaron® 2040 yarn. The predicted critical velocities were

around 450 m/s and 950 m/s for 20-µm and 200-µm round projectiles, respectively. The error between the predicted critical velocities from Hertzian model and experiments increased as the projectile radius of curvature increased. For the 200-µm case, the predicted critical velocity from Hertzian model was higher than the Smith theory. SEM was used to perform post-mortem failure analysis on the failure surface of the recovered specimens.

5.5.2 Failure surfaces

The images presented in this section were taken by an FEI Nova Nano SEM with an operating voltage, a spot size and an average working distance of 5 kV (HV), 3.5, and 5 mm, respectively. Figure 29 presents the failure surfaces of a Twaron® 2040 yarns transversely impacted by a 2-µm round projectile.

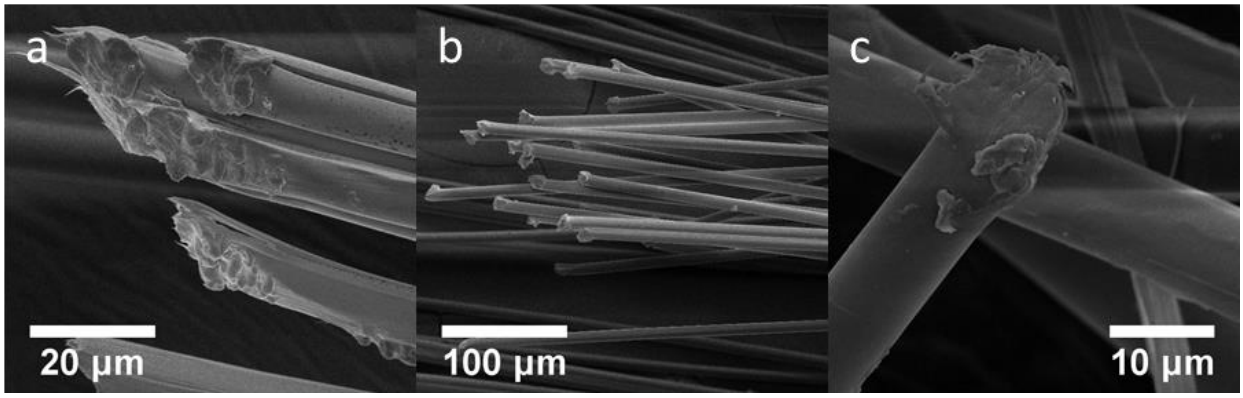

Figure 29: Failure surfaces of the recovered specimen transversely impacted by 2-µm round projectiles at (a) below, (b) between. and (c) above the critical velocities.

From Figure 29, it was observed that majority of the failure surfaces was flat. A small degree of fibrillation was observed when impacted below the critical velocities as shown in Figure 9a. The failure surfaces suggested that the 2-µm round projectile was able to cut and shear through the fibers locally at the point of impact for all the velocities. Such a failure surface was observed at all projectile striking velocity similar to those reported by Hudspeth *et al.* [3, 5], Mayo and Wetzel [9] and Shin *et al.* [28].

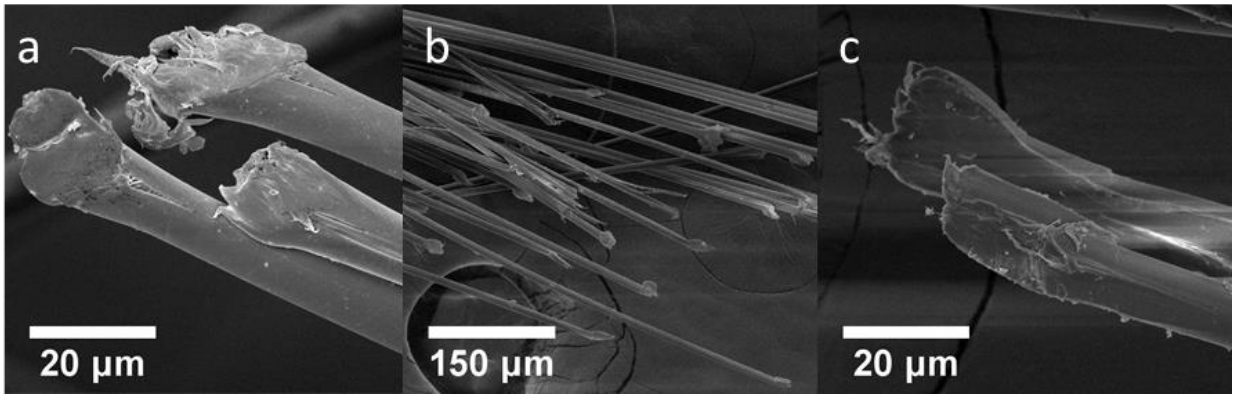

Figure 30: SEM images for 20-µm round projectiles impacted at (a) below, (b) between. and (c) above the critical velocities.

When impacted by a 20-µm round projectile, the failure surfaces revealed a combination of shear and fibrillation, as shown in Figure 30. The combination mode suggested that the fibrils were first compressed in the transverse direction causing the failure surface to be flat. The remaining fibrils were then stretched in the axial direction causing them to fail in fibrillation. The failure criterion implemented in the Hertzian contact model required the indentation depth equal to the diameter of the yarn [8]. To satisfy this assumption, the fibers needed to fail in shear causing the failure surfaces to be flat. A higher degree of fibrillation when impacted by 20-µm round projectile led to a larger error between the predicted critical velocity from the Hertzian model and experiments as shown in Figure 28.

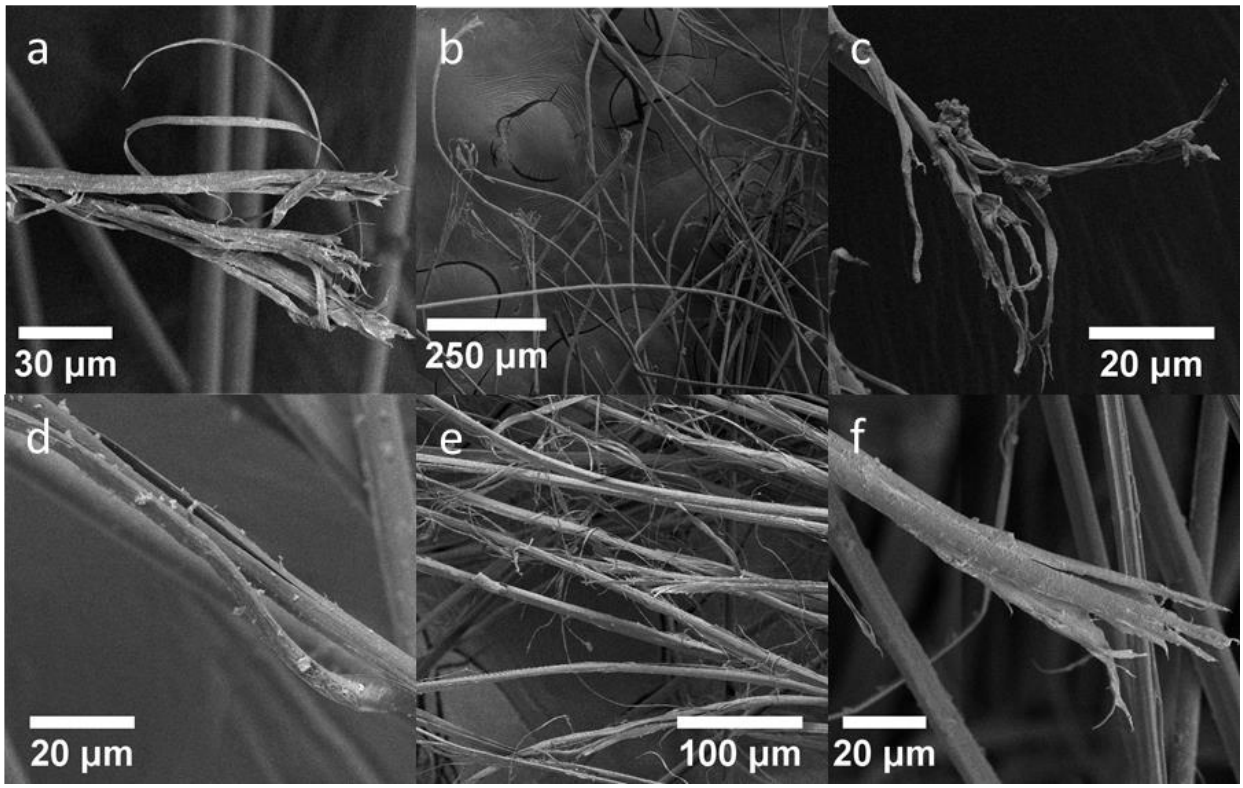

Figure 31: Failure surfaces for the recovered specimens transversely impacted by 200-µm round projectiles (first row) and 2-mm round projectile (second row) at below (a, d), between (b, e). and above (c, f) critical velocities.

When impacted by 200-µm and 2-mm projectiles, majority of the failure surfaces revealed fibril peeling on the fiber surface along the fiber direction as well as fibrillation, as shown in Figure 31. Two reasons that caused the surface to peel. When impacted by these projectiles, the abrasion between fiber-projectile and fiber-fiber causing the fibrils to peel and create defects [27]. When the specimen exhibited stretching, these defects induced a shear stress in the specimen causing the fibers to split axially which led to fibrillation [27]. The release of strain energy at failure caused fibrillation. The fibrils then snapped back and ultimately peel off from that fiber [27]. As the radius of curvature of the projectile increased, a higher force was required to indent causing shear failure in the fiber. For these two cases, the amount of force required to axially split these fibers perhaps was smaller than shear through the fiber. As a result, the fibers failed due to fibrillation. This fibrillation failure mode was also observed in the yarns upon quasi-static transverse loading with round projectiles possessing radii of curvatures larger than 1.59 mm and by Hudspeth *et al.* in transverse impact experiments with a 3.81-mm round projectile onto a Kevlar® KM2 [3, 7]. Since

these specimens failed due to fibrillation, Hertzian model was unable to accurately predict the critical velocity for these cases as the failure criterion required the specimens to fail in shear [8].

5.6 Conclusions

Ballistic experiments were performed to determine the critical velocities for Twaron® 2040 yarns transversely impacted by round projectiles. Four different round projectiles possessing a radius of curvature of 2 μm, 20 μm, 200 μm, and 2 mm were used in this study. The results showed that the average critical velocities increased as projectile radius of curvature increased. These experimental critical velocities were bounded between those predicted from Euler-Bernoulli beam and Smith models. The stress concentration developed at the point of impact caused the axial load showed a demonstrated reduction as the projectile struck above the critical velocities. The recovered specimens revealed that the failure surfaces changed from shear to fibrillation as the projectile radius of curvature increased. For those specimens that were transversely impacted by 2 μm and 20 μm round projectiles, majority of the fibers failed due to shear, as a result, Hertzian contact with shear failure criterion was able to predict their critical velocities.

CHAPTER 6. SUMMARY

6.1 Conclusions

The mechanical behaviors of a Twaron® 2040 yarns under transverse loading were studied at both quasi-static and ballistic conditions [7, 8]. The axial mechanical properties of the yarn were obtained by performing uniaxial tensions tests using an MTS 810. The results showed that the average and standard deviation values for the Young's modulus, ultimate tensile strength, and ultimate tensile strain were 92.55 ± 1.66 GPa, 2.47 ± 0.08 GPa, and 2.71 ± 0.08%, respectively.

The same yarn was also transversely loaded under quasi-static loading condition with indenters possessing radii of curvatures of 0.20 mm, 0.40 mm, 0.79mm, 1.59 mm, 2.50 mm, 3.81 mm and 4.50 mm using the same loading frame. The stress concentration developed in the yarns decreased as the projectile's radius of curvature increased. The failure surfaces on the recovered specimen changed from combination of fibrillation, snapped-back, kink-band and localized shear to only fibrillation as the radius of curvature increased. Strain energy model was capable of predicting the stress concentration in the yarn when loaded by indenter possessing a radius of curvature between 0.20 mm and 1.59 mm. On the other hand, curved beam model was able to predict the stress concentration in the yarn for those that failed only in fibrillation which happened when loaded by indenter with a radius of curvature larger than 1.59 mm.

The ballistic performance of these yarns was also evaluated by performing ballistic experiments with four different round projectiles to determine the critical velocities. A gas/powder gun were utilized to perform these ballistic experiments. The round projectiles implemented in the ballistic experiments possessing a radius of curvature of 2 μm, 20 μm, 200 μm and 2 mm. The results showed that the critical velocities increased as the projectile radius of curvature increased. The critical velocities for all these cases were lower compared to the critical velocity predicted by Smith theory. The failure surfaces revealed that the specimen failed due to mostly shear to mostly fibrillation as the radius of curvature of the projectile increased.

The predicted critical velocity from Smith theory was overestimated when compared to those obtained from experiments for all cases. To improve the prediction capability, two models, Euler-Bernoulli beam model and Hertzian contact model, were developed to predict the critical velocity. Unlike Smith theory, the beam model underestimated the critical velocity for all cases. The experimental critical velocities fall between the Euler-Bernoulli beam model and Smith model for all cases. The Hertzian contact accounted for the projectile-yarn interaction. Since the failure criterion implemented in the Hertzian contact model assumed yarn to fail in shear. In another word, the yarn failed when the indentation depth was equal to the diameter of the yarn. Therefore, Hertzian contact model was capable of predicting the critical velocity for those yarn that fail in shear. The following section discuss the preliminary ideas for potential future studies.

6.2 Future Works

Both models, Euler-Bernoulli beam model, and Hertzian contact model, proposed in these studies assumed that the fiber-fiber interaction was negligible. This assumption will become valid and automatically satisfy if the specimen is a fiber instead of a yarn. However, *in-situ* visualization of a high-performance fiber under transverse impact via light microscopy is extremely challenging. As pointed out in Table 1, typically, the diameter of a high-performance fiber is in the range of 10 μm to 20 μm. The wavelengths of visual light have the same or one-two orders of magnitude less than the fiber diameter, this will inherently limit the spatial resolution of light microscopy at high frame rates [38]. If these challenges can be overcome, the ballistic experiments should be repeated using fibers to obtain the critical velocity. The fiber results can be compared with yarn to study the effect of fiber-fiber interaction on the critical velocity under transverse impact.

In addition, the contact load predicted by the Hertzian contact model needed to be verified experimentally. The most common method to measure load is by using a load cell. However, such a method could not be implemented in ballistic experiments as the load cell required to be mounted parallel to the projectile axis. A non-contact-based method is needed to measure the load in ballistic experiments. One possible way to obtain the contact load is by performing reverse ballistic experiments. The yarn specimen mounts to a sabot and strikes toward a fixed projectile. A load cell mounts behind the projectile to measure the contact load and compare to the model. Such an experimental method is like those presented by Guo *et al.* [39].

The Hertzian contact model presented in Chapter 5 only able to predict the critical velocities for those specimens that failed due to shear. A model should be developed to predict the critical velocities for those that failed due to fibrillation. To achieve the goal, a finite element model is needed to simulate these cases. As pointed out by Sockalingam *et al.* [17, 18], the benefit of a finite element model is the ability to identify additional waves propagate in the yarn under transverse impact. By knowing the type of waves developed in the yarn, an appropriate waveguide model than can be used to represent the yarn [13]. The Hertzian contact implemented in the model only describes the contact force when subjected to point contact. From the high-speed images, it was observed that for those yarns impacted by a 2-mm projectile, the contact between the yarn specimen and the projectile become a curve line. Therefore, contact theory that describes a line contact force is needed to be implemented into the model. Finally, the failure criterion based on experimental observation is then enforced in the model to predict the critical velocities.

6.3 Additional studies

Besides axial and transverse loading condition on yarns, we also performed ballistic experiments to determine the durability of single ply CT 709 Twaron®. A folding and stretching machines were developed to exert cyclic loading on single ply CT 709 Twaron® for 10,000 and 80,000 cycles corresponding to 15 months and 10 years of usage, respectively. Uniaxial tension experiments were performed on the virgin and artificially aged yarn to determine the residual mechanical properties. A 9-mm low velocity gas gun was utilized to determine the ballistic limit of the virgin and aged single ply fabric. The details of this study are presented in Chapter 7.

The round projectiles used in the ballistic limit to determine the critical velocities of the yarn was made by steel. For transverse impact experiments on yarn, the projectile is expected to remain elastic. However, plastic deformation will occur in these projectiles under transverse impact with a few plies of high-performance fabric or soft body armor. To accurately predicted the ballistic limit, the mechanical behavior of the projectile at high strain-rates must be considered. Perhaps the most widely use experimental apparatus to determine the dynamic mechanical behavior of materials is the Kolsky bar [40]. Typically, the yield and flow stresses obtained from Kolsky bar experiments were presented as true stress, true strain and nearly constant engineering strain rates [41]. However, when performing numerical simulations for predictions of large deformation, the

yield and flow stresses are usually expressed in term of true strain rates instead of engineering strain rates [42, 43]. Hence, Chapter 8 presents a method to characterize the mechanical behavior of steel under nearly constant engineering and true strain-rates.

CHAPTER 7. THE EFFECTS OF REPETITIVE FOLDING AND BIAXIAL STRETCHING ON THE BALLISTIC PERFORMANCE OF SINGLE PLY BODY ARMOR FABRIC

7.1 Abstract

One of the possible reasons for the deterioration of soft body armors is day to day use. The body movements of the user exert repetitive mechanical loading on the armor system, thereby causing folding and stretching. Accordingly, it is important to study the durability of soft body armor under repetitive folding and biaxial stretching. To achieve these goals, experimental apparatus were developed to simulate folding and stretching on single ply Twaron® fabric corresponding to either 15 months or 10 years of usage. After such mechanical aging, single yarns were extracted from virgin and artificially aged fabrics and subsequently pulled in uniaxial tension in an effort to determine the resulting mechanical performance. Additionally, a gas gun was used to determine the ballistic limit of virgin and artificially aged fabrics. From uniaxial tensile experiments, the folded yarns show signs of deterioration when compared to yarns extracted from virgin fabric. On the other hand, the ballistic limit for all cases is quite similar, suggesting that accelerated folding and biaxial stretching up to 10-years equivalency do not degrade the ballistic performance of single ply Twaron® fabric.

Keywords: Fiber degradation; Ballistic limit; Single ply fabric; Artificial aging

---

7.2 Introduction

High performance fibers, such as those manufactured from poly[(benzo-[1,2-d;5,4-d']-benzoxazole-2,6-diyl)-1,4-phenylene] (PBO), phenylene terephthalamides (PPTA) and ultra-high-molecular-weight polyethylene (UHMWPE) are characterized by their superior mechanical properties. These fibers exhibit an unmatched combination of high Young's Modulus, high ultimate tensile strength, high impact resistance, and low density. As such, high performance fibers have become prominent in ballistic protection applications such as soft body armors and turbine fragment containment systems.

In 2003, PBO soft body armor systems worn by two US police officers were fully penetrated by projectile threats for which they were designed to halt; these were the first known incident in the US wherein a vest failed to successfully halt a threat for which it was designed [44, 45]. The Office of Law Enforcement Standards (OLES) of the National Institute of Standards and Technologies (NIST) conducted a research program under the aegis of the National Institute of Justice (NIJ) to investigate the underlying issues behind the armor failures and to study the long-term stability and durability of soft armor systems. Subsequently, several published reports have indicated that the ultimate tensile strengths of PBO yarns removed from one of the incidents armor systems decreased by 30% as compared to yarns extracted from pristine soft armor [44-46]. Hence, it was concluded that PBO fibers could degrade and deteriorate due to environmental factors and day-to-day usage by the user.

After these incidents, research into the degradation of soft body armors became essential, with several factors being studied with great intensity: combined elevated humidity and temperature [47-52], and exposure to UV radiation [47, 48, 53-55]. It has also been suggested that soft body armors may degrade due to day-to-day usage by the wearer, for instance, the body movements of the wearer may cause the body armor to be folded [56-58] as well as stretched which in turn may lead to system material or structural degradation. Previous studies have mainly focused on PBO fibers under uniaxial tensile loading with little attention paid to PPTA fabrics, especially to their ballistic resistance to projectile impact. Therefore, the main focus of this study is to investigate the role of folding and biaxial stretching in the degradation of single ply PPTA fabric, which is widely used in soft body armors.

7.3 Materials and Methods

7.3.1 Specimen

The single ply plain weave Twaron® fabric used in this study was provided by Barrday Corporation, Charlotte, North Carolina. According to the manufacturer, the Twaron® fabric was woven using yarn possessing a linear density, breaking strength, and rupture strain of 960 dtex, 225 N, and 3.45%, respectively. The dimensions of the single ply Twaron® fabric square panels used for

experimentation were 266.7 mm by 266.7 mm (10.5” by 10.5”). The fabric dry weight was 198.03 g/m2 with a thread count in both the warp and weft directions of 27 yarns per inch (YPI).

7.3.2 Stretching device

One of the goals in this study was to determine the effect of artificial aging of single ply PPTA fabric through repetitive biaxial stretching. To achieve this objective, a stretching / loosening device was developed to impart accurate and repeatable loading to induce artificial damage in the single ply PPTA fabric. Figure 32 shows a top view of the loosening device, demarcating the fabric specimen clamped between four sets of plates, which are subsequently displaced via movement of the pneumatic actuators. To minimize friction, four ball bearings were utilized and placed under each plate. Actuators were employed to push and pull the plates to produce repeatable biaxial loading on the fabric and were controlled by a programmable logic controller (PLC) via a four-way solenoid valve to automate the stretching process. The movement of the actuators simultaneously stretch the fabric in two directions, thus artificially damaging the fabric bi-axially at the center of the specimen as shown in Figure 32. A single ply fabric was placed in between the plates and a torque of 4.5 Nm (40 inch-pounds) was applied to each of the screws to secure the fabric with a known pressure. Each actuator was set to pull the plate at a force of 2200 N. The single ply body armor fabric specimens were stretched to either 10,000 or 80,000 cycles corresponding to 15 months or 10 years of usage, respectively [59].

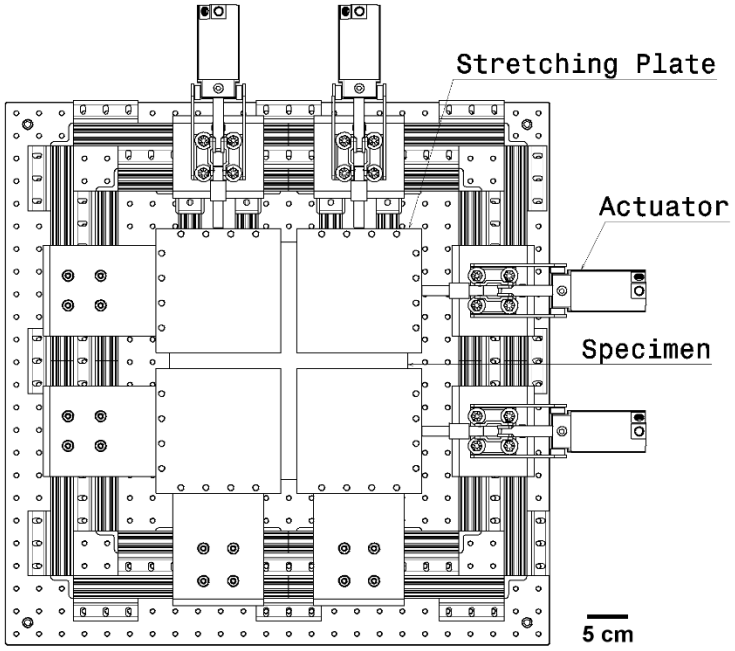

Figure 32: Top View of the stretching device used to repeatedly loosen the fabric in a biaxial manner at the center of the fabric pane.

7.3.3 Folding device

Another goal of this study was to determine the effects of artificial aging through folding of the single ply PPTA fabric. The folding device, which can be seen in Figure 33, consists of a bottom plate, a top plate, and a pneumatic actuator which was controlled by a PLC. The specimen was first folded in half and then sandwiched between the top and bottom plates as shown in Figure 33. The movement of the actuator caused the top plate to open and close by 50 degrees with respect to the bottom plate. This motion folded the specimen, creating a crease at the sample fold line and introduced damage to a localized strip. Similar to the stretched fabrics, these fabrics were also folded for either 10,000 or 80,000 cycles corresponding to 15 months or 10 years of usage, respectively [59].

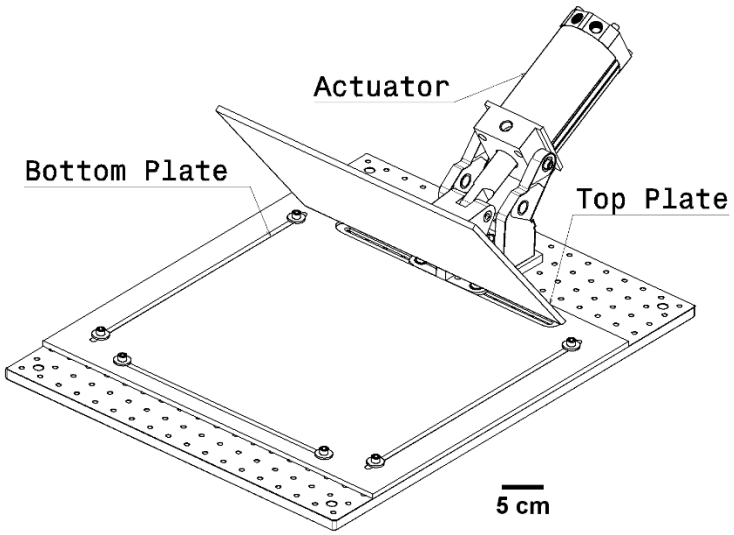

Figure 33: Isometric view of the folding machine used to damage fabric via cyclic opening-closing of the demarcated top plate.

7.3.4 Uniaxial tensile experiments

In order to determine the effect of stretching and folding on yarn constitutive properties, uniaxial tensile tests were performed on single yarns extracted from fabric plies. Since warp yarns typically exhibit more crimp and have thicker widths compared to weft yarns optical microscopy was used to determine warp and weft directions [22]. After determining ply directionality, yarns were extracted from both new and artificially degraded fabric in both warp and weft directions around the fabric center. For the folded fabric, the warp and weft yarns were extracted perpendicular to the crease line. At least ten yarns were extracted in each cases and were pulled in tension with a servo-hydraulic universal testing system (MTS 810). In accordance with ASTM D2256 [24], single yarns were placed in a set of pneumatic bollard grips with in a gage length of 190.5 mm (7.5 inch) as shown in Figure 34. The lower pneumatic grip moved downwards at a velocity of 1.9 mm/s, resulting in a tensile strain rate of 0.01/s.

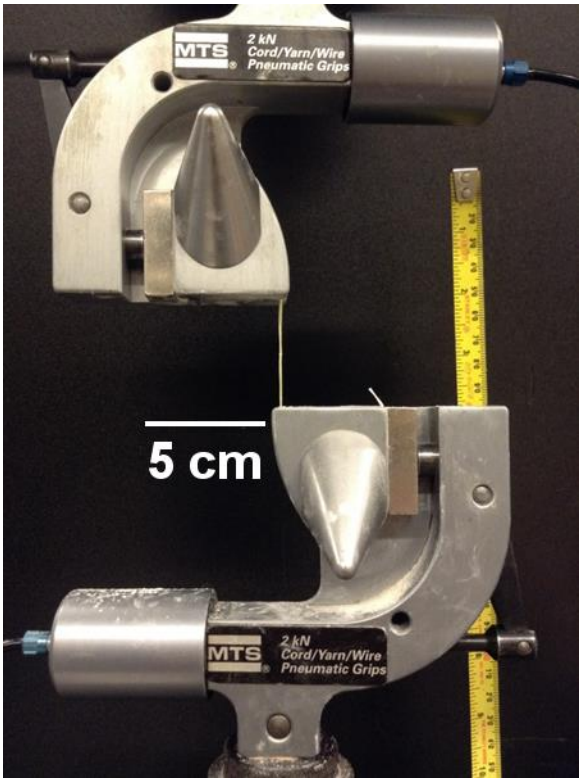

Figure 34: Experimental setup for uniaxial tensile experiments.

7.3.5 Ballistic limit experiments

The ballistic performance of virgin and artificially damaged specimens was determined using a 20-mm gas gun, as shown in Figure 35. Two sets of chronographs were employed to measure the projectile incoming velocity (V_i) before impact and the projectile residual velocity (V_r) after passing through the fabric. The projectiles used in this study were Hornady 124 grain 9-mm full metal jacketed round nose projectile (FMJRN). As the diameter of the projectile was significantly less than the inner diameter of the barrel, polyurethane foam sabots were used to ensure the projectile trajectory was straight and parallel to the axis of the gun barrel. An end cap was used to strip the sabot from the projectile. Single ply fabric specimens were fixed between two plates within the target chamber via toggle clamps, which were used to apply clamping pressure on the single ply fabric as shown in Figure 36. In an effort to ensure projectile impact into the damaged region of the artificially degraded fabric plies, a laser bore sight was used to align the damaged center of the fabric with the axis of the gun barrel.

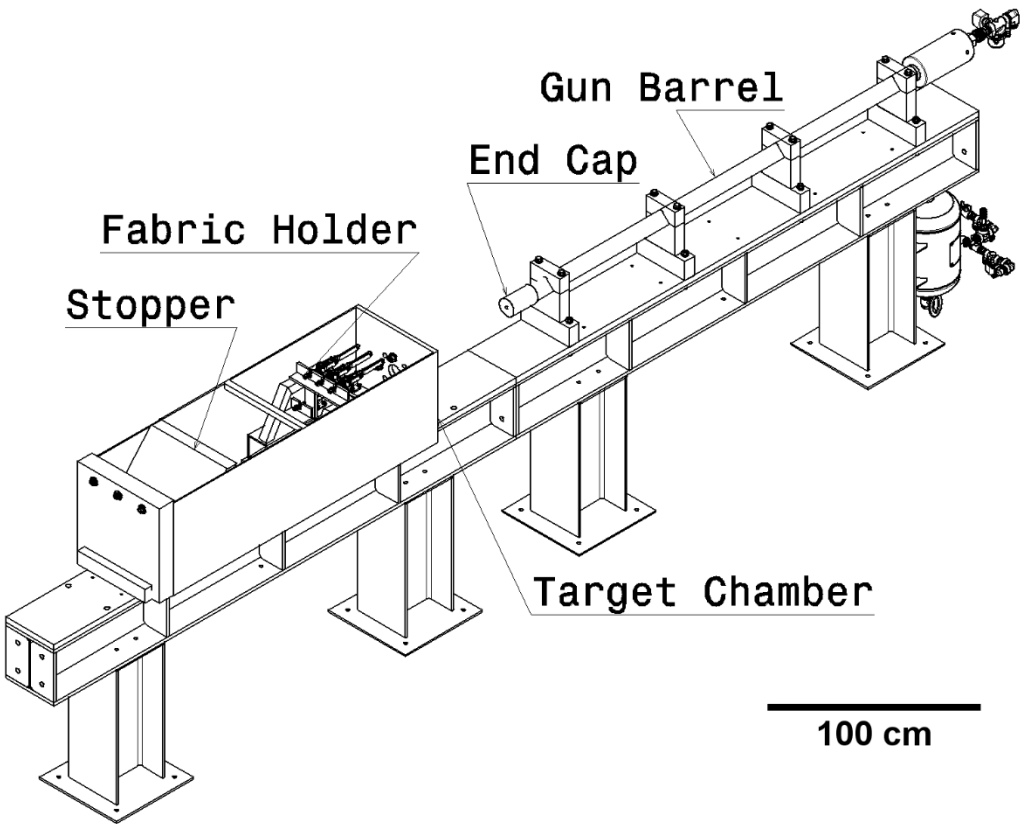

Figure 35: Isometric view of the 20-mm gas gun system used to fire projectiles into the single-ply fabric specimens. Note that an end cap was used to strip the sabot from the projectile.

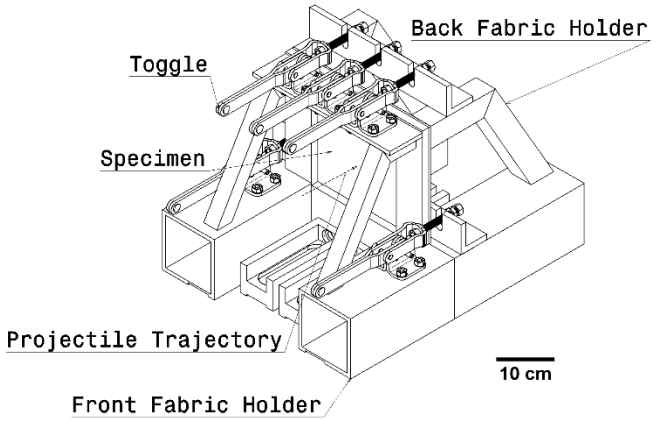

Figure 36: Holder used to affix single-ply specimens within the target chamber.

7.4 Results and discussion

7.4.1 Uniaxial tensile experiments

In an effort to determine the effect of stretching and folding on yarn mechanical properties, uniaxial tensile experiments were performed on single tows extracted from fabric plies. In Figure 37 shows a comparison between mechanical properties of yarns extracted from virgin and artificially aged single ply Twaron® fabric. Most notably, both warp and weft yarns extracted from folded fabric exhibited a demonstrative reduction in tensile strength and breaking strain as compared to the virgin fabric, with increased folding cycles resulting in a corresponding strength/strain degradation. The Young's modulus from warp and weft yarns extracted from virgin and folded single ply fabric show no sign of degradation, quite similar to the degradation behavior exhibited by Zylon® when subjected to temperature and humidity aging [52]. It is important to note that these results do not seem to be in agreement with the previous study [57], wherein the mechanism of folding appeared to be slightly different; Holmes *et al.* placed a thin rod along the folding line, resulting in less stress-concentrated zone. Indeed, a crease-line cannot be seen from post-fold images in the Holmes *et al.* study [56]. However, in the current work, no rod was placed along the fabric folding line, resulting the formation of a crease-line after cyclic folding process. Additionally, Erickson [58] also studied the effects of folding pressure on Kevlar 29 and found that when Kevlar 29 was subjected to high pressure folding, the failure load decreased as the folding pressure increased. The results from Erickson [58] seem to be in agreement with this study; as the folding pressure increases, a folding line will become apparent in the material and introduces localized damage to the material causing the failure load decreases.

For fabric subjected to stretching, increasing the number of loading cycles results in an increase in Young's modulus and a corresponding decrease in failure strain. It is suggested that such a change in mechanical properties is promoted by crimp reduction due to the fabric stretching; the initial waviness in the yarn is removed due to the stretching process, thereby leading to the increase in Young's modulus and apparent reduction in failure strain. Additionally, from Figure 37, the tensile strength for stretched yarn appears to be independent of the applied stretching, suggesting in an independence of cyclic tensile fatigue for the as-tested Twaron® yarns when subjected to 250 MPa loading for up to 80k loading cycles.

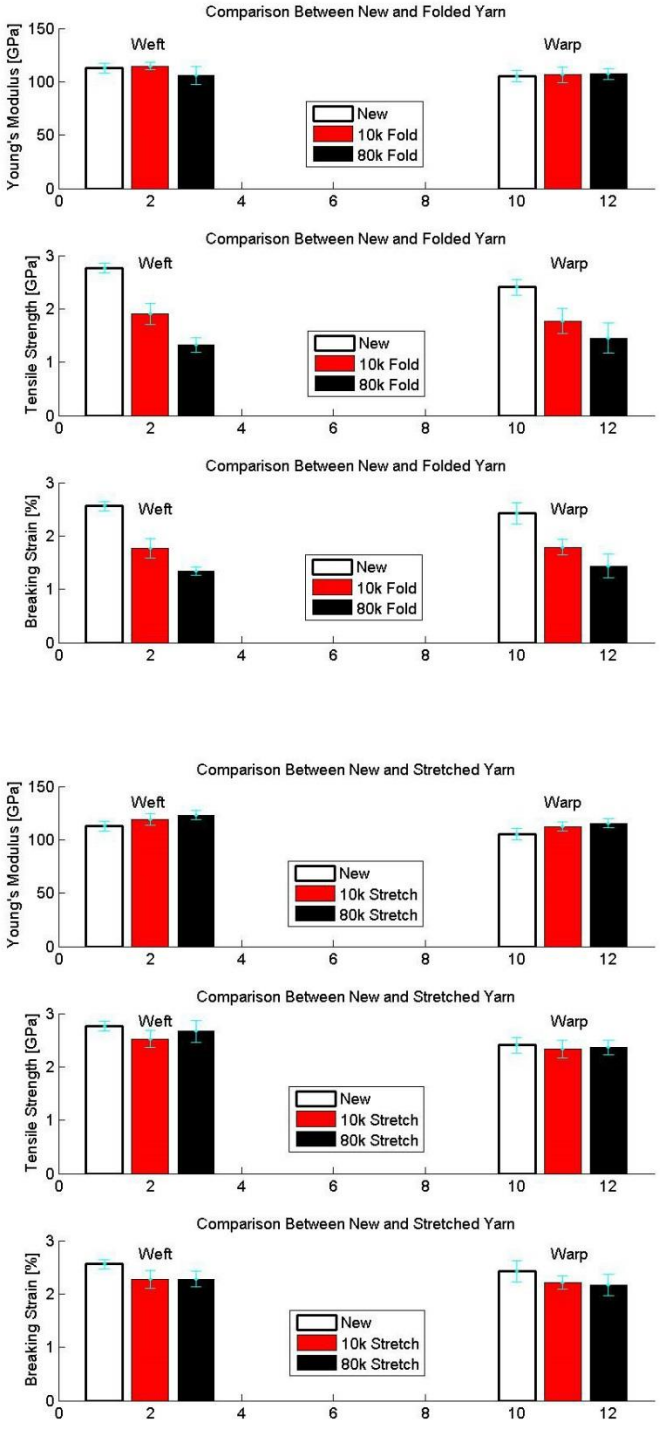

Figure 37: Comparison of mechanical properties between yarns that have been extracted from virgin (New), folded (Fold) and stretched (Stretch) single ply fabric.

7.4.2 Ballistic limit experiments

The single ply ballistic limit, denoted as V50, is defined as the velocity at which the projectile is expected to perforate the armor 50% of the time [1]. Figure 38 shows the projectile residual velocity (V_r) vs. incoming projectile velocity (V_i) for all five cases of interest to the current study; virgin, folded 10k, folded 80k, stretched 10k and stretched 80k. Interestingly, the ballistic limit for all cases was observed to be independent of fabric mechanical degradation, resulting in a V50 value of 55-60 m/s for all cases. These results suggest that the properties of the single ply Twaron® fabrics governing penetration at such low velocities does not deteriorate through repeated mechanical loading. From examination after the fact, it was observed that yarns were pulled out from the fabric by the 9-mm FNJRN projectile, allowing the projectile to "nose through" without rupturing the yarns.

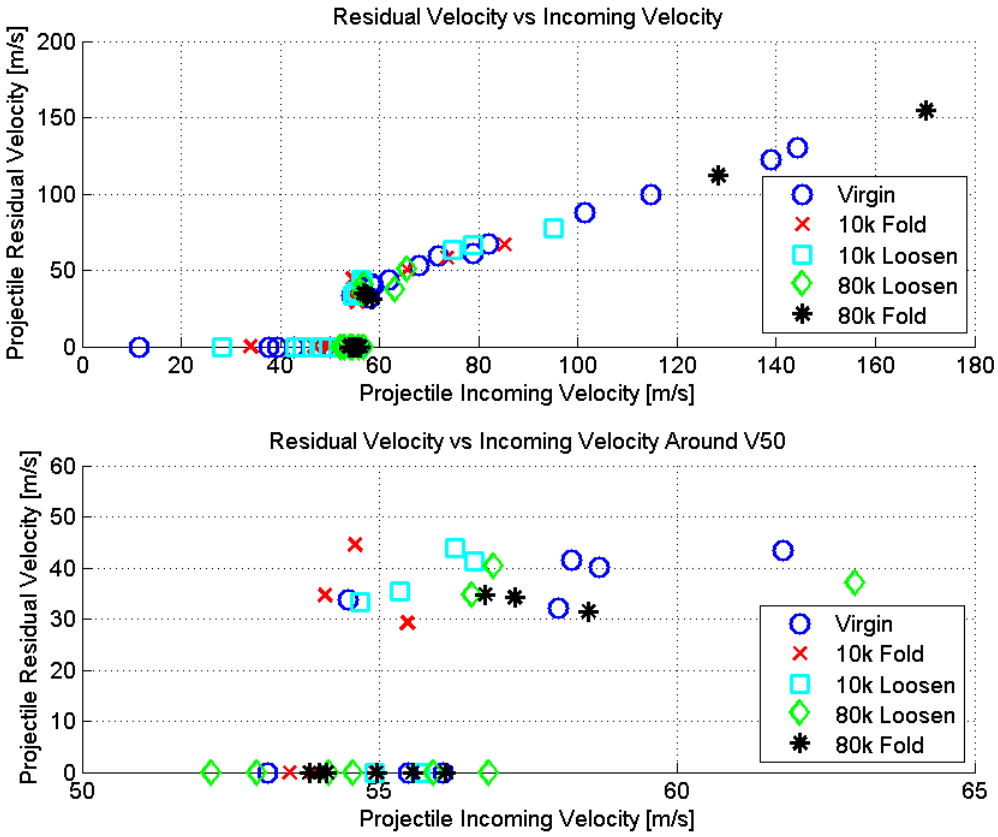

Figure 38: Residual velocity vs incoming projectile velocity for virgin and artificially damaged single ply Twaron® fabric.

The energy absorption by the fabric can be found by taking the different between the incoming and residual projectile kinetic energy.

$$E_m = \frac{V_i^2 - V_r^2}{2} \qquad \text{Eqn. 1}$$

Figure 39 shows energy absorbed by the fabric divided by projectile mass (E_m) as calculated using Equation 1 plotted against incoming projectile velocity (V_i) for all five cases. If the projectile impacts with a velocity far below the ballistic limit, it does not penetrate through the fabric, resulting in the residual velocity of zero (V_r = 0). Therefore, below the ballistic limit, all five cases fall under the same curve as showed in Figure 39. However, at the V50, the projectile is able to penetrate the fabric 50% of the time. Accordingly, the V_r no longer remains as zero, and the energy absorption capability of the fabric drops drastically when the incoming projectile velocity is above the ballistic limit.

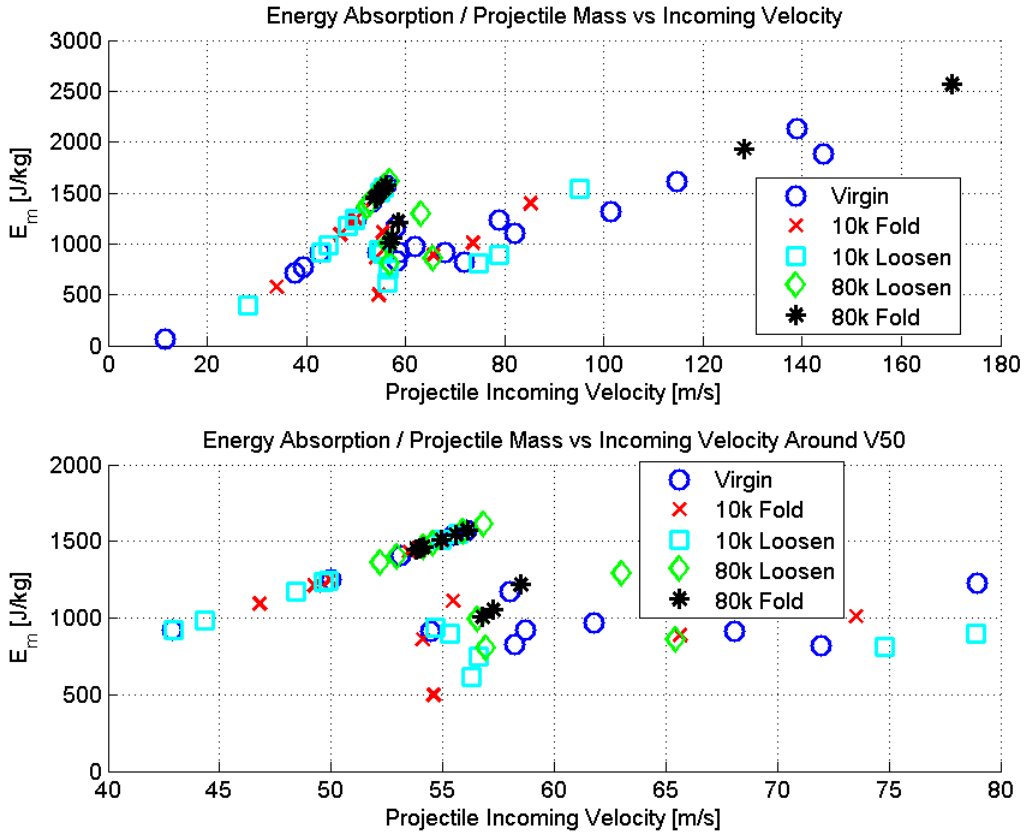

Figure 39: Comparison between virgin and mechanically degraded single ply fabric energy normalized by projectile mass.

Cunniff [60] has reported the correlation between V50 and mechanical properties of the fibers as shown in Equation 24

$$\phi\left(\frac{V_{50}}{\sqrt[3]{\frac{\sigma\varepsilon}{2\rho}\sqrt{\frac{E}{\rho}}}}, \frac{A_d A_p}{m_p}\right) = 0 \qquad \text{Eqn. 24}$$

where σ is the fiber ultimate tensile strength, ε is the fiber breaking strain, E is the fiber Young's modulus, ρ is the fiber's density, A_d is the areal density of the fabric, A_p is the projectile presented area, and m_p is the mass of the projectile [60]. This correlation has also been derived theoretically by Phoenix and Porwal [61]. The correlation shows that degradation in mechanical properties of the fiber should lead to inferior ballistic performance of the fabric. However, for the folded fabric tested in this study, Equation 24 appears to be invalid, as mechanical properties (tensile strength and breaking strain) of yarns extracted from the folded fabric do indeed degrade, however the ballistic limit of said fabric appears to remain unchanged when compared to virgin fabric.

Figure 40 shows typical images of fabric after being shot near the V50. Locally at the impact site, yarns were pulled out from the single ply fabric, as the 9-mm FMJRN projectile was able to nose through the panel. None of the yarns were visually broken due to nosing process, suggesting that the strain developed within the fabric was less than the yarn breaking strain. Utilizing Smith's equations of single yarn transverse impact, the strain developed in the yarn when subjected to transverse impact around the V50 could be determined using Equation 25 [4].

$$\mathrm{V} = \mathrm{C}\sqrt{\varepsilon(1+\varepsilon) - \left(\sqrt{\varepsilon(1+\varepsilon)} - \varepsilon\right)^2} \qquad \text{Eqn. 25}$$

where V is the projectile incoming velocity, C is the yarn wave speed, and ε is the strain developed in the yarn. The strain developed in the yarn is estimated to be only 0.1%. As this strain is significantly less than that required to rupture the yarn, none of the yarns are loaded to failure. Rather, the yarns were pulled out from the fabric, allowing the projectile to nose through the panel [62]. This nose-thru phenomenon was seen for all impact conditions, resulting in a similar fabric penetration process for all tested panels and ultimately providing the similarity in ballistic resistance.

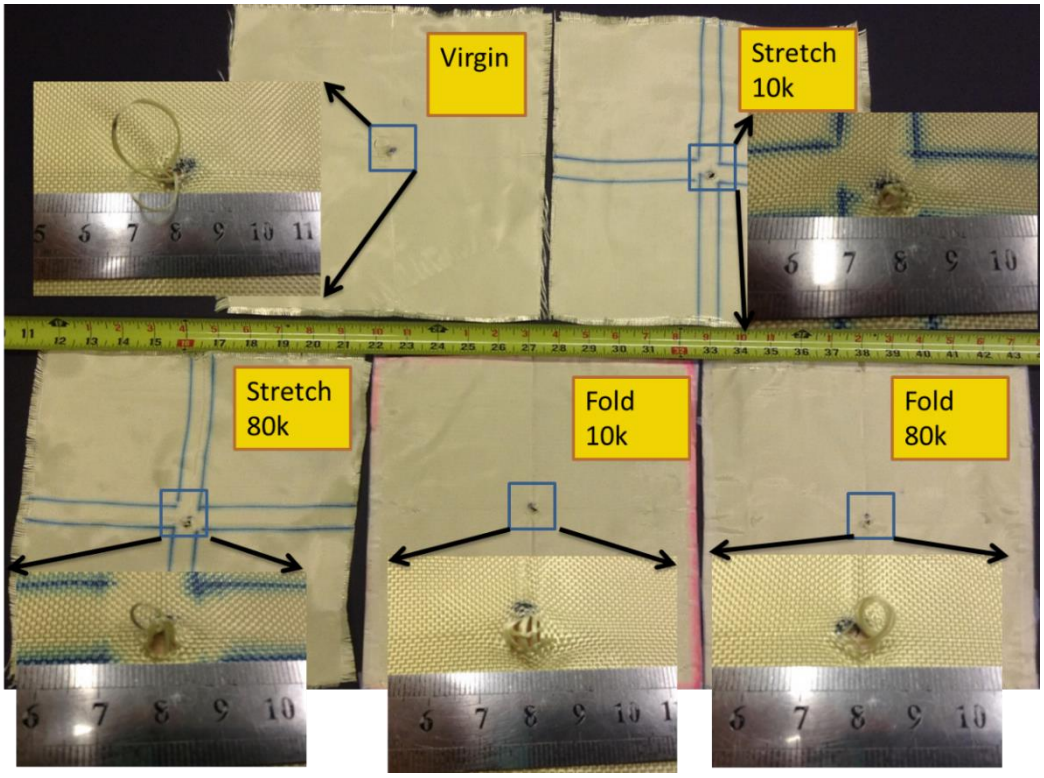

Figure 40: Images for all five cases after being shot near V50.

7.5 Conclusions

Folding and stretching devices were developed to consistently fold or stretch single ply Twaron® fabric for a pre-determined number (10,000 or 80,000) of cycles. Yarns were extracted from virgin, stretched and folded single ply Twaron® fabric to perform uniaxial tensile tests. While the tensile strength and breaking strain of folded yarn showed demonstrative reduction when compared to yarns extracted from virgin fabric, the elastic modulus and failure strain of stretched yarn only showed a slight increase and reduction, respectively, when compare to yarns extracted from the virgin fabric. Additionally, single ply fabric was impacted with a 9-mm FMJRN projectile, yielding an unchanged ballistic limit for mechanically aged fabrics as compared to virgin panels. Regardless of mechanical aging, post shot images from fabric impacted at the ballistic limit, demonstrated that yarns were pulled out from the ply thereby allowing the projectile to nose through the panel without rupturing the local constituent yarns. As a result, the ballistic limits for all five cases were quite similar. These results suggest that repetitive mechanical loading simulating up to ten years of usage does not degrade the ballistic performance of the single ply PPTA fabric.

CHAPTER 8. EFFECTS OF CONSTANT ENGINEERING AND TRUE STRAIN RATES ON THE MECHANICAL BEHAVIOR OF 304 STAINLESS STEEL

(A version of this chapter has been published in Journal of Dynamic Behavior of Materials [63])

8.1 Abstract

A Kolsky bar (split Hopkinson pressure bar) with a pulse shaping technique was utilized to study the dynamic behavior of 304 stainless steel at high constant engineering and true strain rates. To show the differences between the strain rates, equations were presented for the engineering strain rate and strain as a function of true strain rate. To deform the specimen at constant true strain rates at 600 s-1 to 2,500 s-1, a bi-linear incident pulse was necessary. Furthermore, a trapezoidal incident wave was required to deform the specimen at a constant true strain rate of 7,000 s-1. The results show that the dynamic flow stresses of the specimens increased with increasing strain rates. At the highest strain rate of 7,000 s-1, the flow stress of specimen deforming at constant engineering strain rate was clearly higher than the flow stress obtained at a similar constant true strain rate.

Keywords: Engineering strain rate; True strain rate; Kolsky bar; Pulse shaping; Constant strain rate; 304 stainless steel

---

8.2 Introduction

Most metallic materials such as steel, copper, and aluminum are categorized as ductile materials. One of the unique properties of ductile materials is the ability to experience large deformation without fracture. Due to this ductility, these metals are capable of undergoing metal-forming and fabrication processes such as rolling, forging, and extrusion. In addition, ductile materials such as steel also exhibit a balanced combination of high Young's modulus, high yield strength, and high ultimate tensile strength. As such, steel has been widely used in several engineering fields, such as aerospace, building construction, and automotive industry. Some of these applications require the material to survive dynamic loading such as crashes, impact, and blast loading. Therefore, it is

often necessary to determine the mechanical properties of ductile materials undergoing large deformation at high strain rates.

The compressive mechanical behavior of steel deforming to large strains at various strain rates has been studied by many researchers. For example, ASTM E9-09 [64] is widely used as a reference for the mechanical properties of steel at low engineering strain rates. Fitzsimons and Kuhn [65] modified the MTS servo controlled machine by adding a capacitor discharge circuit to investigate the material behavior at true strain rates between 10-2 and 102 s-1. Cam plastometer had been employed to compress specimen at a constant true strain rate which is extremely difficult to control in conventional testing machines [43]. However, the highest true strain rate that could be achieved is only around 150 s-1 [42, 43]. The Kolsky bar is used to characterized the material properties at high strain rates (102 to 105 s-1) [40, 66]. Utilizing a Kolsky bar, the dynamic behavior of steel up to engineering strain rate of approximately 103 s-1 have been obtained by several researchers [67-69]. From these studies, most researchers agree that the compressive yield strength and flow stress increase as the strain rate is increased.

As pointed out by Ramesh and Narasimhan [41], the stress-strain curves obtained from Kolsky bar experiments are usually presented as true stress, true strain, and at nearly constant engineering strain rate. However, when performing numerical simulations for predictions at large deformation, the yield and flow stresses are usually expressed in term of true strain rates instead of engineering strain rates [42, 43]. However, the dynamic behavior of stainless steel deforming at high true strain rates has not been reported. Therefore, it is desired to characterize the behavior of the specimens at constant true strain rates. Hence, the purpose of this study is to present a method to characterize the compressive stress-strain behavior of a 304 stainless steel at high, constant true strain rates using a modified Kolsky bar. The obtained behavior is then contrasted with the behavior of the 304 stainless steel deforming at high, constant engineering strain rates.

8.3 Material and Methods

The ductile specimens utilized in this study were made from a commercially available precision ground 304 stainless-steel rod (diameter = 6.35 mm, length = 0.6 m). The rod was cut into disc-shape specimens with final diameter of 6.35 mm and thickness of 2.8 ± 0.01 mm.

8.3.1 Analytical Model

For an incompressible specimen under uniaxial compression loading with the assumption that compression is taken as positive, the true stress (σ) in the specimen can be calculated from Eqn. 26, where S is the engineering stress and e is the engineering strain.

$$\sigma = S(1 - e) \qquad \text{Eqn. 26}$$

The relationship between true strain (ε) and engineering strain (e) can be calculated from Eqn. 27.

$$\varepsilon = -\ln(1 - e) \qquad \text{Eqn. 27}$$

The true strain rate ($\dot{\varepsilon}$) is calculated by taking the time derivative of the expression presented in Eqn. 27, and the obtained expression is presented in Eqn. 28,

$$\dot{\varepsilon} = \frac{\dot{e}}{1 - e} \qquad \text{Eqn. 28}$$

It should be emphasized that if the strain in the specimens is small, the corresponding true strain rate is nearly equal to the engineering strain rate. In addition, Eqn. 28 also shows that at large strains, the specimen could either deform at a constant engineering strain rate or constant true strain rate but not both.

To allow the specimen to deform at a constant true strain rate, it is necessary for the history of true strain rate to be trapezoidal shape as sketched in Figure 41. The reason is that the specimen requires a finite amount of time to reach the desired true strain rate (*D* in Figure 41d), similar to a specimen being deformed in a Kolsky bar at constant engineering strain rate [40, 67]. Mathematically, the expression for a trapezoidal shape pulse is given in Eqn. 29.

$$\dot{\varepsilon} = \begin{cases} \dfrac{D}{t_0} t \quad , & t \le t_0 \\ D \quad , & t \ge t_0 \end{cases} \qquad \text{Eqn. 29}$$

where t_0 is the time to reach a constant true strain rate as shown in Figure 41d. Substituting Eqn. 29 into Eqn. 28, an expression for engineering strain is obtained (Eqn. 30).

$$e = \begin{cases} 1 - \exp\left(-\frac{Dt^2}{2t_0}\right) & , \ t \le t_0 \\ 1 - \exp\left[-D\left(t - \frac{t_0}{2}\right)\right] & , \ t \ge t_0 \end{cases} \qquad \text{Eqn. 30}$$

Finally, the engineering strain rate (Eqn. 31) is determined by taking time derivative of Eqn. 30

$$\dot{e} = \begin{cases} \frac{Dt}{t_0}\exp(-\frac{Dt^2}{2t_0}) & , \quad t \le t_0 \\ D\exp\left[-D\left(t - \frac{t_0}{2}\right)\right] & , \quad t \ge t_0 \end{cases} \qquad \text{Eqn. 31}$$

The corresponding true strain is obtained by substituting Eqn. 30 into Eqn. 27. Figure 41 presents the time histories of engineering strain (Eqn. 30), engineering strain rate (Eqn. 31), and true strain (Eqn. 27) required to deform the specimen at a constant true strain rate (Eqn. 29). In Figure 41, D = 2700 s^{-1} and t_0 = 50 μs, which simulates one of the experiments discussed later.

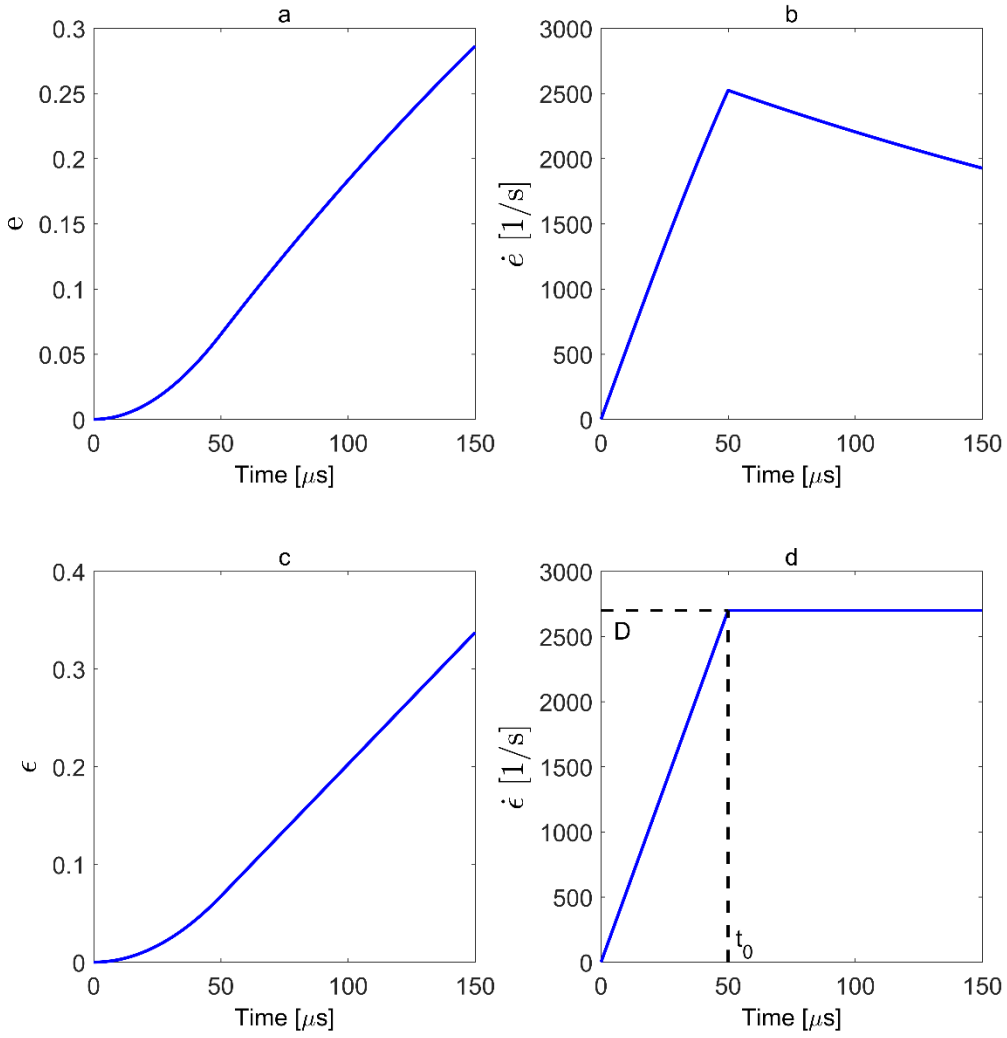

Figure 41: History of (a) engineering strain (b) engineering strain rate (c) true strain and (d) true strain rate for a specimen deformed at a constant true strain rate of 2,700 s^{-1}

8.3.2 Experimental Setup and Procedure

Two different experimental apparatus were used to characterize the behavior of 304 stainless steel at low and high strain rates: an MTS 810 universal testing machine and a Kolsky compression bar with pulse shapers.

For low strain rate experiments, Vaseline act as the lubricant was applied on both ends of the specimen, the specimen then was sandwiched between compression platens as shown in Figure 42. In order to compress the specimens at a constant engineering strain rates, the lower platen was set to move at 0.28 mm/s and 0.028 mm/s resulting in constant engineering strain rates of 0.1 s^{-1} and

0.01 s^{-1}. To determine the mechanical response at a constant true strain rate, the length of the specimen (L) as a function of time should be deformed according to Eqn. 32, where L_0 is the specimen original length [65]. Therefore, the bottom part of the platen was set to move with the displacement history that followed Eqn. 32, resulting in the specimen being compressed at a constant true strain rate.

$$L(t) = L_0 \exp(\dot{\varepsilon} t) \qquad \text{Eqn. 32}$$

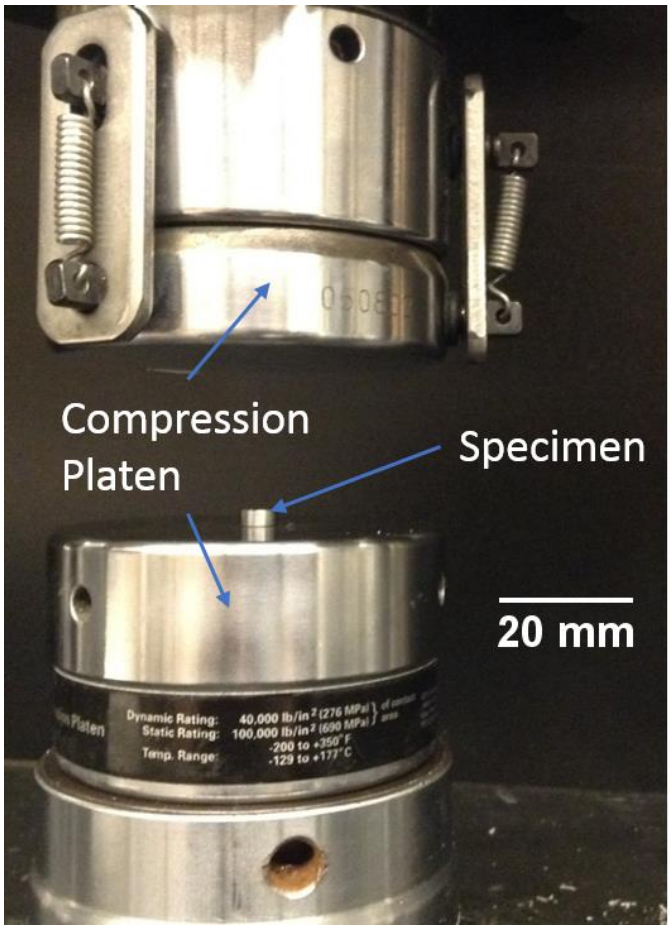

Figure 42: Experiment apparatus to characterized mechanical behavior at low strain rates

A Kolsky compression bar was employed to characterize the dynamic behavior of the specimen at constant engineering and true strain rates. The Kolsky bar consists of an incident bar, a transmission bar and a momentum trap bar as schematically shown in Figure 43. All the bars used in this study are maraging steel rods having a common diameter of 19 mm. The specimen was sandwiched between the incident and transmission bars. Similarly, the Vaseline was applied to the specimen ends. A gas gun launched the striker against the incident bar to generate a compressive

stress wave. Two pairs of resistance strain gages were attached on the incident and transmission bar surfaces to record the incident (ε_I), reflected (ε_R) and transmitted (ε_T) pulses. These strain gages were connected to Wheatstone bridges. Two differential amplifiers were used to amplify the pulses. An upper bandwidth of 100 KHz was set on the amplifiers to filter and smooth the signals. Utilizing the 1-D wave theory with the assumption that the specimen is in stress equilibrium, the engineering strain rate, engineering strain, and engineering stress can be obtained by using Eqn. 33, where C_b, E_b, A_b and A_s are the bar wave speed, bar Young's modulus, bar cross section area and specimen cross sectional area respectively [40]. Finally, the true stress, true strain and true strain rate are determined by substituting Eqn. 33 into Eqn. 26, Eqn. 27 and Eqn. 28 respectively.

$$\dot{e} = -\frac{2}{C_b L_0}\varepsilon_R$$

$$e = \int \dot{e}\, dt \qquad \text{Eqn. 33}$$

$$S = \frac{A_b}{A_S} E_b \varepsilon_T$$

To deform the specimen at a constant engineering strain rate, the reflected wave should have a plateau region as indicated in Eqn. 33a. However, to deform at a constant true strain rate, it is necessary for the reflected pulse to increase in time initially and then have a negative slope afterward as sketched in Figure 41b. To achieve such a pulse profile for a ductile material, it is essential to employ a pulse shaping technique to generate bi-linear (Figure 44c) and trapezoidal (Figure 44d) incident pulses to enable the specimen to deform at constant true strain rates of 600 s^{-1}, 2,500 s^{-1} and 7,000 s^{-1} respectively [70, 71]. To limit experimental trials, the pulse shaping model developed by Frew *et al.* [70, 71] was utilized to predict the material and dimensions of the pulse shaper required to generate the desired incident stress wave. The dimensions of the pulse shapers to deform the specimens at nearly constant engineering and true strain rates are summarized in Table 4.

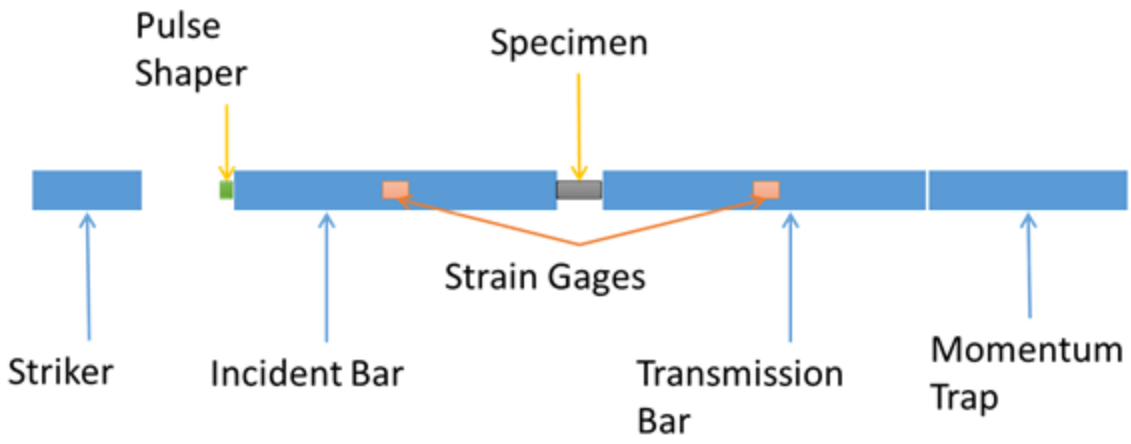

Figure 43: A Kolsky bar experimental setup

8.4 Experimental Results

Dynamic compression experiments were performed using the Kolsky bar on the 304 stainless steel specimens at the engineering and true constant strain rates at about 700 s^{-1}, 2,400 s^{-1}, 7,000 s^{-1}. For each strain rate, five repeating experiments were conducted. Table 4 summarizes the experimental parameters including striker length, striking velocity, pulse shapers material and dimensions to deform the specimen at constant engineering or true strain rate.

Table 4: Kolsky bar experimental parameters to deform the specimen at constant engineering (Eng.) or true strain rates.

		Striker		Pulse Shaper		
	Strain Rate [1/s]	Length [m]	Velocity [m/s]	Material	Diameter [mm]	Thickness [mm]
True	633	0.6	8.8	Copper 110	11.4	3.3
True	2720	0.3	15.8	Copper 110	13.8	3.3
True	6700	0.3	23.5	304 Stainless Steel	14.0	2.4
Eng.	794	0.6	10.3	Copper 110	11.4	3.3
Eng.	2080	0.3	16.8	Copper 110	12.3	3.3
Eng.	6830	0.3	35.4	304 Stainless Steel	12.7	2.8

Figure 44 present four sets of the typical experimental outputs obtained from Kolsky bar experiments to deform the specimens at either constant engineering (Figure 44a and 44b) or true

(Figure 44c and 44d) strain rates. The incident (Inc), reflected (Ref) and transmitted (Tra) pulses were plotted in Figure 44. From these figures, it is verified that the axial forces on the specimens were in equilibrium, since the transmitted pulse is in good agreement with the sum of incident and reflected strain pulse [40].

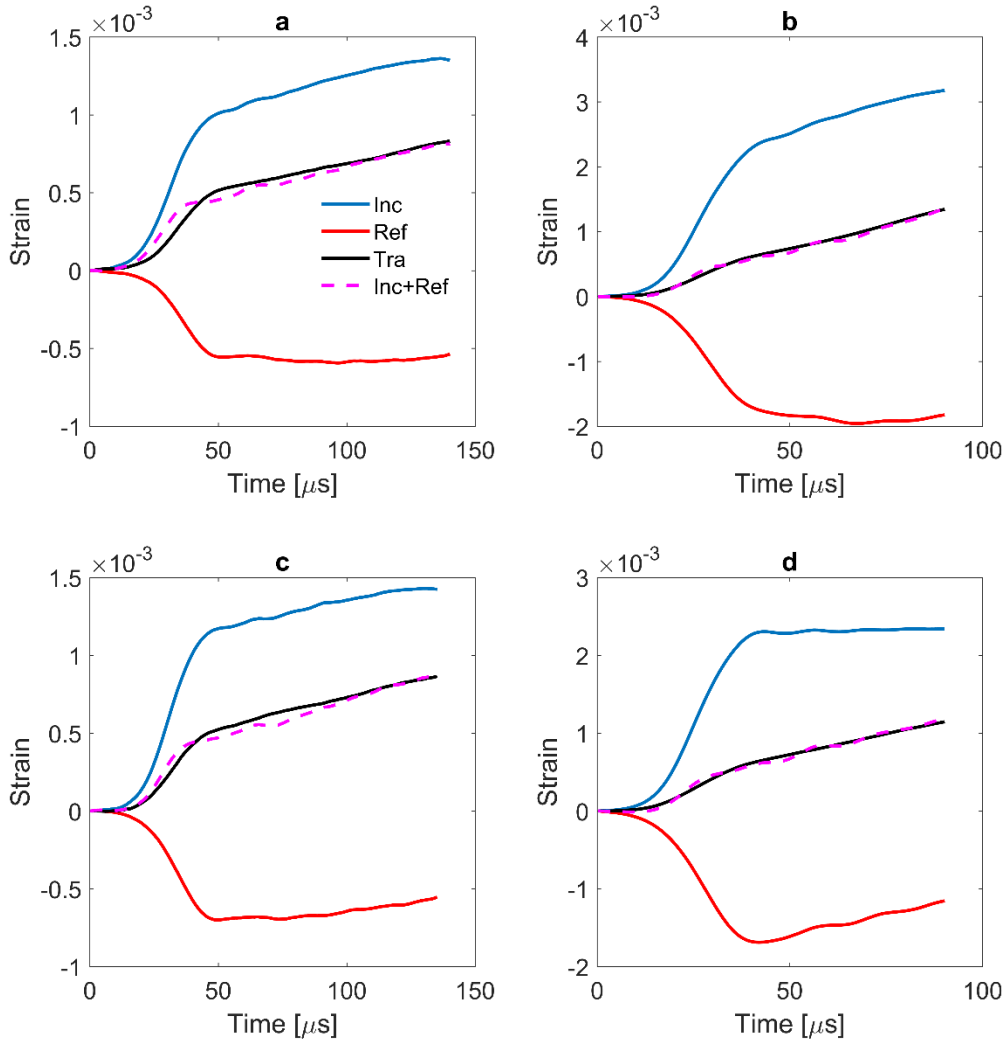

Figure 44: Typical experimental results obtained from Kolsky bar experiments to deformed specimen at constant engineering (Eng.) or true (True) strain rate at about (a) Eng. 2080 s^{-1} (b) Eng. 6830 s^{-1} (c) True 2720 s^{-1} (d) True 6700 s^{-1}

The strain rate histories for the above four cases are summarized in Figure 45. It is noted that there are plateau regions in the plots which indicate that the specimens could only deformed at either nearly constant engineering (Figure 45a and 45b) or true (Figure 45c and 45d) strain rates but not both.

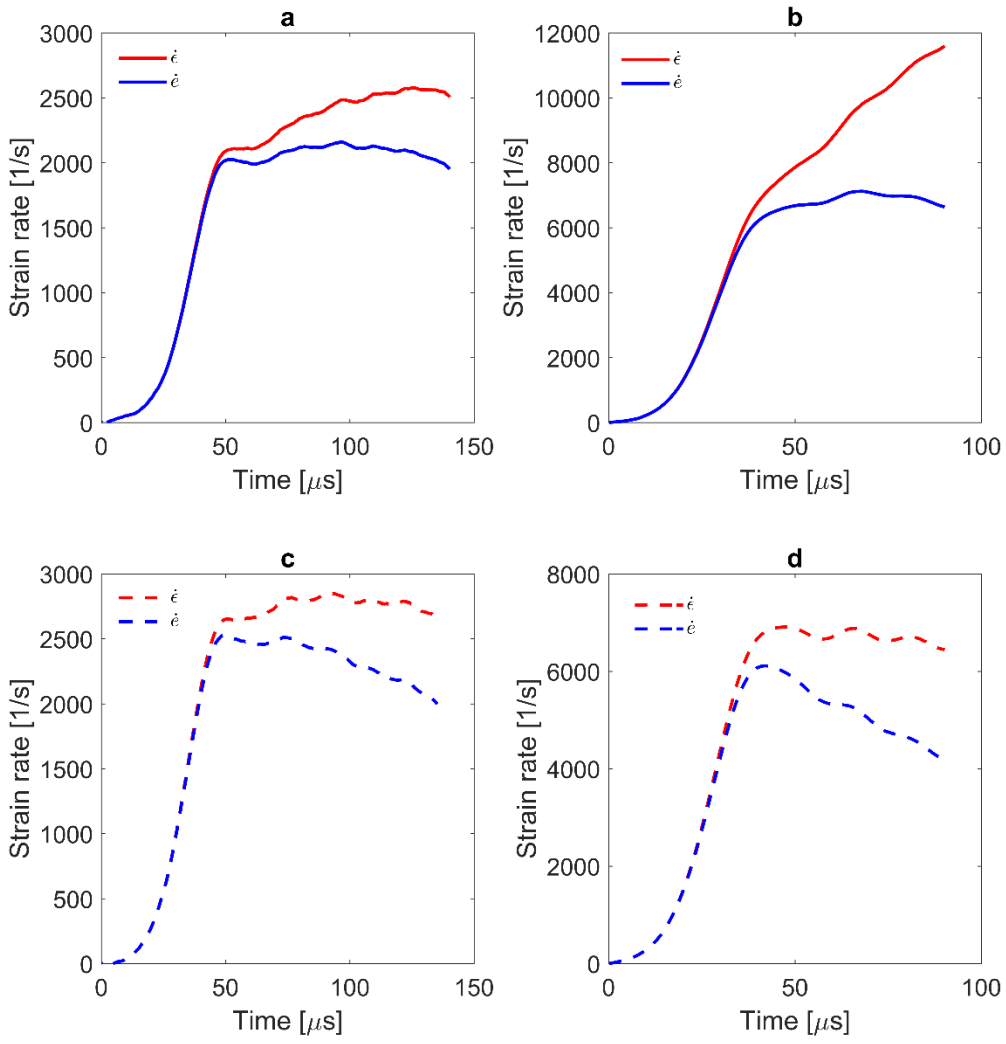

Figure 45: The corresponding strain rate history for specimen that deform at constant engineering (Eng.) or true (True) strain rate at about: (a) Eng. 2080 s^{-1} (b) Eng. 6830 s^{-1} (c) True 2720 s^{-1} (d) True 6700 s^{-1}

In Figure 46, the flow stress-strain curves at nearly constant engineering and true strain rates are presented [67], the error bars in Figure 46 represent one standard deviation. It was observed that the flow stresses tend to increase with increasing strain rate for both constant engineering and true strain rates. This phenomenon is known as strain-rate hardening in ductile metals and has been observed by many researchers [67, 72, 73].

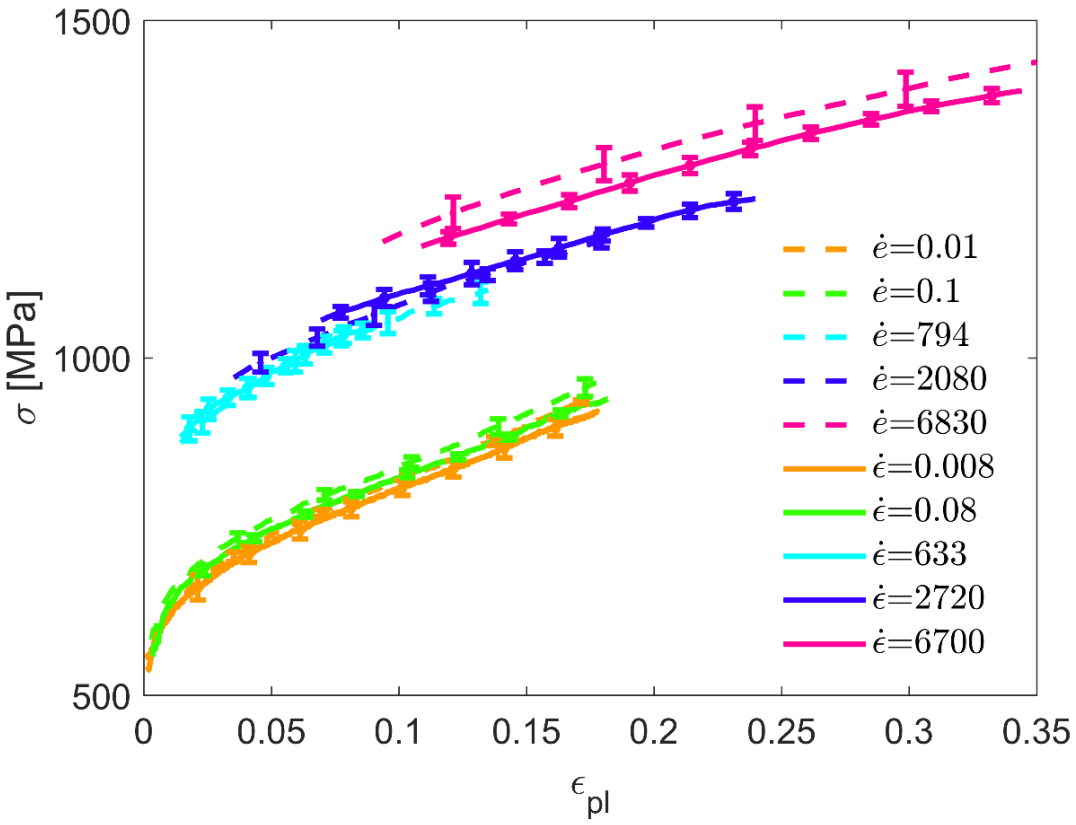

Figure 46: Flow stress strain curves at nearly constant engineering and true strain rates

8.5 Discussion of Results

In Figure 46, it is shown that the flow stress-strain curves between constant engineering and true strain rate at similar magnitudes below 3,000 s^{-1} are very close to each other. For example, at about 2,400 s^{-1} strain rate, it was observed that the flow stress at the constant true strain rate of 2,720 s^{-1} nearly overlaps that obtained at constant engineering strain rate of about 2,080 s^{-1}. However, the flow stress for the specimens deformed at a constant engineering strain rate of 6,830 s^{-1} shows a clearly difference from that obtained at the true strain rate of 6,700 s^{-1}.

One possible explanation for the observed differences in flow stress at higher strain rates is that the average strain rate for a specimen deformed at constant engineering and true strain rates were relatively close at strain rates below 3,000 s^{-1}. For example, to deform a specimen at a constant true strain rate at about of 2700 s^{-1}, the average engineering strain rate (average of the decreasing slope in Figure 45c) that is experienced by the specimen is rate at about 2,200 s^{-1}. As a result, the

flow stress for the specimen deformed at a constant engineering strain rate of 2,080 s^{-1} is similar to that specimen deformed at the constant true strain rate of 2,720 s^{-1}. However, to deform the specimen at around 6,700 s^{-1} true strain rate, the corresponding engineering strain rate needs to have a much steeper decreasing slope as shown in Figure 45d, the average engineering strain rate (average of the decreasing slope in Figure 45d) on the specimen is about 5,000 s^{-1} which is significantly lower than 6,830 s^{-1}. As a consequence, the flow stresses for the specimen deformed at 6,700 s^{-1} true strain rate is significantly lower compared to the specimens deformed at 6,830 s^{-1} engineering strain rate.

8.6 Material Constitutive Models

We used two material models in an effort to represent these data in an analytical form; namely, Johnson-Cook and Camacho-Ortiz [74, 75]. It should be emphasized that the parameters determined from both models were obtained by curve fitting experimental data at constant engineering and true strain rates from about 0.01 s^{-1} to 7,000 s^{-1}. The Johnson-Cook model is expressed in Eqn. 34 as

$$\sigma = \left[A + B\left(\varepsilon_{pl}\right)^{n}\right]\left[1 + C \ln \dot{\varepsilon}^{*}\right]$$

$$\dot{\varepsilon}^{*} = \begin{cases} \dfrac{\dot{\varepsilon}}{\dot{\varepsilon}_0} \ for\ constant\ true\ strain\ rate \\ \dfrac{\dot{e}}{\dot{e}_0} \ for\ constant\ engineering\ strain\ rate \end{cases} \qquad \text{Eqn. 34}$$

For the Johnson-Cook model, the first term represents isotropic hardening where A, B, ε_{pl} and n are equivalent to yield stress, strength coefficient, plastic true strain and strain hardening parameter, respectively. The second term represents the strain rate hardening, where $\dot{\varepsilon}$ and $\dot{e}$ are true and engineering strain rates, $\dot{\varepsilon}_0$ and $\dot{e}_0$ are the reference true and engineering strain rates, and C is a fitting parameter [75]. The parameter A was determined from the yield stress at the lowest engineering or true strain rate using a 0.2% offset strain. Parameters B, C and n were determined through curve fitting. The Johnson-Cook parameters obtained from this study are listed in Table 5.

As pointed out by Clausen *et al*. [72] , an issue with Eqn. 34a can occur with the logarithmic term if the dimensionless strain rate terms are less than one. To avoid this problem, the second term in Eqn. 34a is taken as one for dimensionless strain rates less than one. Thus, for these very low strain rates Eqn. 34b is taken as rate-independent.

Table 5: Johnson-Cook curve fitting parameters for constant true (True) and engineering (Eng.) strain rate

	A [MPa]	B [MPa]	n	C	$\dot{\varepsilon}_0$[1/s]	$\dot{e}_0$[1/s]
True	566	832.8	0.5647	0.02876	0.008	-
Eng.	546	851	0.5075	0.0275	-	0.01

Like the Johnson-Cook model, the Camacho-Ortiz model has a product form with a strain hardening term and a strain rate term [74]. However, the strain rate term is a power law rather a logarithm term. Thus, the problem with small strain rates is avoided. A slightly modified version of the Camacho-Ortiz material model was used for this study (Eqn. 35).

$$\sigma = Y\left(1 + \frac{E\varepsilon_{pl}}{Y}\right)^{n}(1+\dot{\varepsilon}^{*})^{C}$$

$$\dot{\varepsilon}^{*} = \begin{cases} \dfrac{\dot{\varepsilon}}{\dot{\varepsilon}_0} \ for\ constant\ true\ strain\ rate \\ \dfrac{\dot{e}}{\dot{e}_0} \ for\ constant\ engineering\ strain\ rate \end{cases} \qquad \text{Eqn. 35}$$

where Y is the yield stress, E is the Young's modulus, n and C are the curve fitting parameters. Table 6 lists the parameters obtained by curve fitting the average experimental data at different strain rates using Eqn. 35. It should be noted that the yield stresses (Y) were obtained by implementing the 0.2 % offset strain at the lowest engineering and true strain rates, respectively.

Table 6: Camacho-Ortiz curve fitting parameters for constant true (True) and engineering (Eng.) strain rate

	Y [MPa]	E [GPa]	n	C	$\dot{\varepsilon}_0$ [1/s]	$\dot{e}_0$ [1/s]
True	566	200	0.1048	0.05574	10	-
Eng.	546	200	0.119	0.05411	-	10

The comparison of the flow stress-strain curves obtained from both models with the data obtained from experiments at both constant engineering and true strain rates are presented in Figure 47. It can be observed that both models are in good agreement with the experimental results.

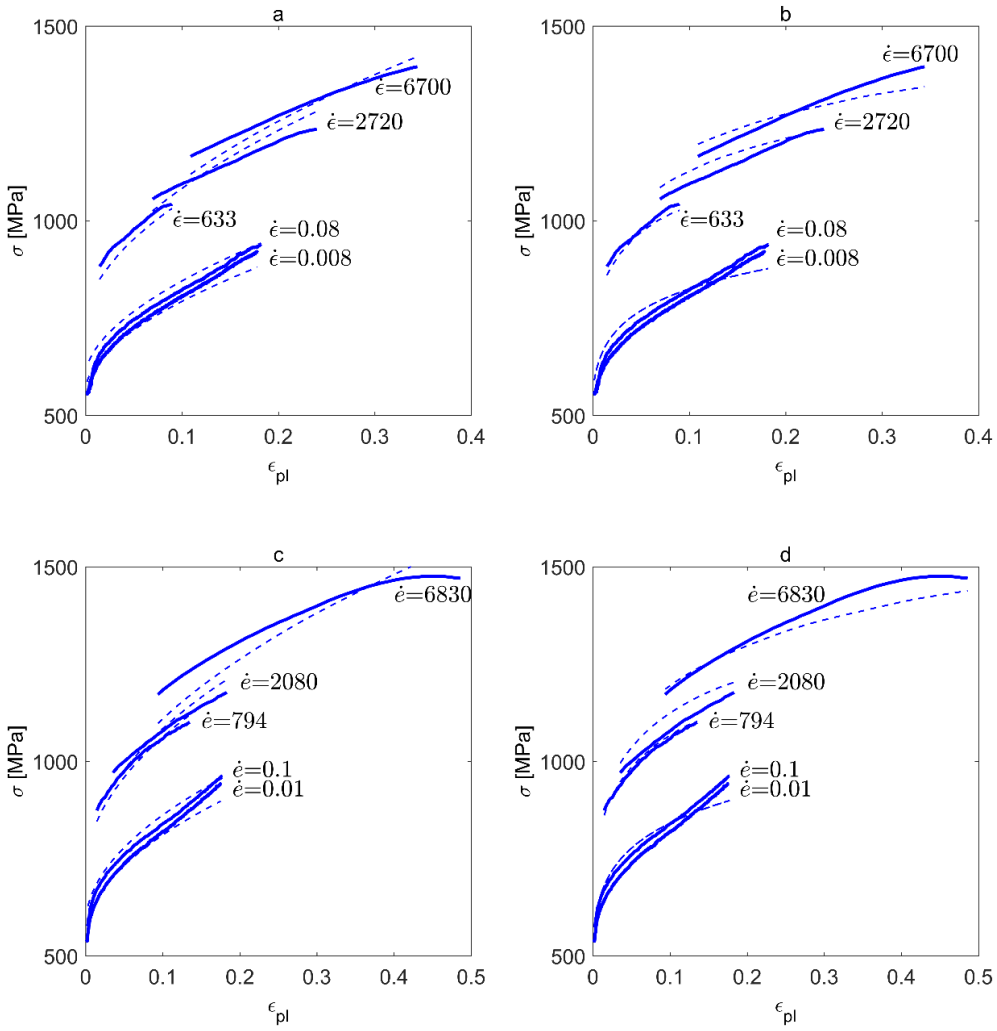

Figure 47: Comparison between experimental flow stress-strain curves (Exp) with (a) Johnson-Cook (JC) model at nearly constant true strain rates (b) Camacho-Ortiz (CO) model at nearly constant true strain rates (c) JC model at nearly constant engineering strain rates and (d) CO model at nearly constant engineering strain rates

8.7 Conclusions

Dynamic experiments utilizing a Kolsky bar to characterize the compressive dynamic behavior of 304 stainless steel at high constant engineering and true strain rates are presented and compared in this study. Equations were derived for the engineering strain rate and strain as a function of true strain rate. To deform the specimen at a nearly constant true strain rate, it is necessary for the engineering strain rate to increase in time initially and then have a negative slope afterward. The negative slope becomes much steeper for experiments at high true strain rates. Consequently, to compress a specimen below 3,000 s^{-1} true strain rate, a bi-linear incident pulse was needed.

However, to deform a specimen at 7,000 s^{-1} true strain rate, a trapezoidal incident wave was needed. Using these incident pulses, the compressive stress-strain response of 304 stainless steel deformed to large strains at high true strain rates was obtained and compared with the response obtained at constant engineering strain rates. The results indicate that, below a strain rate of 3,000 s^{-1}, there is very little difference for the specimens deforming at a particular constant engineering or true strain rate. However, at a high strain rate of 7,000 s^{-1}, the flow stress for the specimens deforming at constant engineering strain rate is higher than the stress from a specimen deforming at comparable constant true strain rate. Finally, both the Johnson-Cook and Camacho-Ortiz material models fit the experimental data accurately.

REFERENCES

1. Standard, N., *0101.06. Ballistic resistance of body armor*. Washington: National Institute of Justice, 2008.–40 p, 2008.
2. Cunniff, P.M. *Decoupled response of textile body armor*. in *Proceedings of the 18th International Symposium of Ballistics*. 1999. CRC, Boca Raton, FL.
3. Hudspeth, M., et al**.**, *Effect of projectile nose geometry on the critical velocity and failure of yarn subjected to transverse impact.* Textile Research Journal, 2016.
4. Smith, J.C., F.L. McCrackin, and H.F. Schiefer, *Stress-Strain Relationships in Yarns Subjected to Rapid Impact Loading: Part V: Wave Propagation in Long Textile Yarns Impacted Transversely.* Textile Research Journal, 1958. **28**(4): p. 288-302.
5. Hudspeth, M., et al., *The effects of off-axis transverse deflection loading on the failure strain of various high-performance fibers.* Textile Research Journal, 2016. **86**(9): p. 897-910.
6. Hudspeth, M., W. Chen, and J. Zheng, *Why the Smith theory over-predicts instant rupture velocities during fiber transverse impact.* Textile Research Journal, 2015.
7. Lim, B.H., J.-M. Chu, and W. Chen, *Mechanical Behavior of High-Performance Yarns Transversely Loaded by Different Indenters.* Fibers, 2018. **6**(4): p. 69.
8. Lim, B., et al., *Critical Velocity of High-Performance Yarn Transversely Impacted by Razor Blade.* Fibers, 2018. **6**(4): p. 95.
9. JB Mayo, J. and E. Wetzel, *Cut resistance and failure of high-performance single fibers.* Textile Research Journal, 2014. **84**(12): p. 1233-1246.
10. Carr, D.J., *Failure Mechanisms of Yarns Subjected to Ballistic Impact.* Journal of Materials Science Letters, 1999. **18**(7): p. 585-588.
11. Chocron, S., et al., *Modeling of fabric impact with high speed imaging and nickel-chromium wires validation.* Journal of Applied Mechanics, 2011. **78**(5): p. 051007.
12. Field, J. and Q. Sun, *A high speed photographic study of impact on fibres and woven fabrics (from 19th International Congress on High-Speed Photography and Photonics 1990).* SPIE MILESTONE SERIES MS, 1995. **109**: p. 57-66.
13. Doyle, J.F., *Wave propagation in structure: spectral analysis using fast discrete Fourier transforms.* Springer-Verlag, New York, 1997.

14. Hudspeth, M., et al., *Degradation of yarns recovered from soft-armor targets subjected to multiple ballistic impacts.* Composites Part A: Applied Science and Manufacturing, 2014. **58**(0): p. 98-106.
15. Sanborn, B., A.M. DiLeonardi, and T. Weerasooriya, *Tensile Properties of Dyneema SK76 Single Fibers at Multiple Loading Rates Using a Direct Gripping Method.* Journal of Dynamic Behavior of Materials, 2015. **1**(1): p. 4-14.
16. Cheng, M., W. Chen, and T. Weerasooriya, *Mechanical Properties of Kevlar® KM2 Single Fiber.* Journal of Engineering Materials and Technology, 2005. **127**(2): p. 197-203.
17. Sockalingam, S., et al., *Recent advances in modeling and experiments of Kevlar ballistic fibrils, fibers, yarns and flexible woven textile fabrics – a review.* Textile Research Journal, 2016. **0**(0): p. 0040517516646039.
18. Sockalingam, S., J.W. Gillespie Jr, and M. Keefe, *Dynamic modeling of Kevlar KM2 single fiber subjected to transverse impact.* International Journal of Solids and Structures, 2015. **67–68**: p. 297-310.
19. Sockalingam, S., J. John W Gillespie, and M. Keefe, *Modeling the fiber length-scale response of Kevlar KM2 yarn during transverse impact.* Textile Research Journal. **0**(0): p. 0040517516669074.
20. Walker, J.D. and S. Chocron, *Why Impacted Yarns Break at Lower Speed Than Classical Theory Predicts.* Journal of Applied Mechanics, 2011. **78**(5): p. 051021-051021.
21. Hudspeth, M.C., *Multi-axial failure of high-performance fiber during transverse impact.* 2016.
22. Guo, Z., et al., *Out-of-plane effects on dynamic pull-out of p-phenylene terephthalamide yarns.* Textile Research Journal, 2015. **85**(2): p. 140-149.
23. *Standard Test Methods for Tensile Testing of Aramid Yarns*. 2011, ASTM International.
24. *Standard Test Method for Tensile Properties of Yarns by the Single-Strand Method*. 2015, ASTM International.
25. Hudspeth, M., X. Nie, and W. Chen, *Dynamic failure of Dyneema SK76 single fibers under biaxial shear/tension.* Polymer, 2012. **53**(24): p. 5568-5574.
26. Barber, J.R., *Intermediate mechanics of materials*. Vol. 175. 2010: Springer Science & Business Media.

27. Hearle, J.W., B. Lomas, and W.D. Cooke, *Atlas of fibre fracture and damage to textiles*. 1998: Elsevier.
28. Shin, H.-S., et al., *Cut Resistance of High-strength Yarns.* Textile Research Journal, 2006. **76**(8): p. 607-613.
29. Bazhenov, S., et al., *The fracture of SVM aramide fibers upon a high-velocity transverse impact.* POLYMER SCIENCE SERIES AC/C OF VYSOKOMOLEKULIARNYE SOEDINENIIA, 2001. **43**(1): p. 61-71.
30. Guo, Z., W. Chen, and J. Zheng, *Improved quasi-static twin-fiber transverse compression of several high-performance fibers.* Textile Research Journal. **0**(0): p. 0040517518775927.
31. Guo, Z., et al., *Transverse compression of two high-performance ballistic fibers.* Textile Research Journal, 2016. **86**(5): p. 502-511.
32. Doyle, J.F., *Guided explorations of the mechanics of solids and structures*. 2009: Cambridge University Press.
33. Popov, V.L., *Contact mechanics and friction*. 2010: Springer.
34. Versteeg, H.K. and W. Malalasekera, *An introduction to computational fluid dynamics: the finite volume method*. 2007: Pearson Education.
35. Phoenix, S., et al., *Modeling and Experiments on Ballistic Impact into UHMWPE Yarns Using Flat and Saddle-Nosed Projectiles.* Fibers, 2017. **5**(1): p. 8.
36. Utomo, B.H. and J. Broos, *Dynamic Material Determination Using Single Fiber Impact.* IMAC XXV, Orlando, Florida, USA, 2007.
37. Heru-Utomo, B. *Dynamic Young's modulus determination using single fibre impact*. in *Proceedings of the 57th ARA Meeting, Venice, Italy*. 2006.
38. Hudspeth, M., et al., *In Situ Visual Observation of Fracture Processes in Several High-Performance Fibers.* Journal of Dynamic Behavior of Materials, 2015. **1**(1): p. 55-64.
39. Guo, Z., J. Zheng, and W. Chen, *Reverse ballistics penetration of Kevlar® fabric with different indenters at different loading rates.* Textile Research Journal, 2016.
40. Chen, W.W. and B. Song, *Split Hopkinson (Kolsky) bar: design, testing and applications*. 2010: Springer Science & Business Media.
41. Ramesh, K.T. and S. Narasimhan, *Finite deformations and the dynamic measurement of radial strains in compression Kolsky bar experiments.* International Journal of Solids and Structures, 1996. **33**(25): p. 3723-3738.

42. Baragar, D.L., *The high temperature and high strain-rate behaviour of a plain carbon and an HSLA steel.* Journal of Mechanical Working Technology, 1987. **14**(3): p. 295-307.
43. Hockett, J.E., *Compression testing at constant true strain rates.* Journal Name: Am. Soc. Testing Materials, Proc.; Journal Volume: Vol: 59; Other Information: Orig. Receipt Date: 31-DEC-60, 1959: p. Medium: X; Size: Pages: 1309-19.
44. Ashcroft, J., D.J. Daniels, and S.V. Hart. *Status report to the attorney general on Body Armor Safety Initiative testing and activities*. 2004; Available from: http://purl.fdlp.gov/GPO/gpo29780.
45. Ashcroft, J., D.J. Daniels, and S.V. Hart, *Supplement I: Status Report to the Attorney General on Body Armor Safety Initiative Testing and Activities*. 2004, U.S. Dept. of Justice, Office of Justice Programs, National Institute of Justice: Washington, DC.
46. Gonzales, A.R., R.B. Schofield, and S.V. Hart, *Third Status Report to the Attorney General on Body Armor Safety Initiative Testing and Activities*. 2005, Washington, DC: U.S. Dept. of Justice, Office of Justice Programs, National Institute of Justice.
47. Holmes, G.A., K. Rice, and C.R. Snyder, *Ballistic fibers: A review of the thermal, ultraviolet and hydrolytic stability of the benzoxazole ring structure.* Journal of Materials Science, 2006. **41**(13): p. 4105-4116.
48. Walsh, P.J., et al., *Environmental effects on poly-p-phenylenebenzobisoxazole fibers. I. Mechanisms of degradation.* Journal of Applied Polymer Science, 2006. **102**(4): p. 3517-3525.
49. Forster, A.L., et al., *Hydrolytic stability of polybenzobisoxazole and polyterephthalamide body armor.* Polymer Degradation and Stability, 2011. **96**(2): p. 247-254.
50. Forster, A.L., et al., *Long-term stability of UHMWPE fibers.* Polymer Degradation and Stability, 2015. **114**: p. 45-51.
51. Tamargo-Martínez, K., et al., *Studies on the Thermal Degradation of Poly (p-phenylene benzobisoxazole).* Chemistry of Materials, 2003. **15**(21): p. 4052-4059.
52. Chin, J., et al., *Temperature and humidity aging of poly(p-phenylene-2,6-benzobisoxazole) fibers: Chemical and physical characterization.* Polymer Degradation and Stability, 2007. **92**(7): p. 1234-1246.

53. Jin, J., et al., *Effects of light stabilizer on the ultraviolet stability of poly-p-phenylenebenzobisoxazole (PBO) fibers.* Iranian Polymer Journal, 2012. **21**(10): p. 739-745.
54. So, Y.-H., *Photodegradation mechanism and stabilization of polyphenylene oxide and rigid-rod polymers.* Polymer International, 2006. **55**(2): p. 127-138.
55. Zhang, T., et al., *UV accelerated aging and aging resistance of dihydroxy poly(p-phenylene benzobisoxazole) fibers.* Polymers for Advanced Technologies, 2011. **22**(5): p. 743-747.
56. Holmes, G.A., et al., *The role of folding in the degradation of ballistic fibers.* Polymer Composites, 2010. **31**(5): p. 879-886.
57. Kobayashi, H., et al., *X-ray scattering study on the damage in fibers used in soft body armor after folding.* Polymer Composites, 2012. **33**(5): p. 803-811.
58. Ericksen, R.H., *Effect of folding on the strength of kevlar 29 and nylon parachute materials.* Fibre Science and Technology, 1981. **15**(3): p. 161-172.
59. Holmes, G., et al. *The effect of environmental and mechanical mechanisms on the performance of soft body armor*. in *17th International conference on composite materials*. 2009.
60. Cunniff, P.M. *Dimensionless parameters for optimization of textile-based body armor systems*. in *Proceedings of the 18th international symposium on ballistics*. 1999. San Antonio: Texas.
61. Leigh Phoenix, S. and P.K. Porwal, *A new membrane model for the ballistic impact response and V50 performance of multi-ply fibrous systems.* International Journal of Solids and Structures, 2003. **40**(24): p. 6723-6765.
62. Cheeseman, B.A. and T.A. Bogetti, *Ballistic impact into fabric and compliant composite laminates.* Composite Structures, 2003. **61**(1–2): p. 161-173.
63. Lim, B.H., et al., *Effects of Constant Engineering and True Strain Rates on the Mechanical Behavior of 304 Stainless Steel.* Journal of Dynamic Behavior of Materials, 2017. **3**(1): p. 76-82.
64. *Standard Test Methods of Compression Testing of Metallic Materials at Room Temperature*. 2009, ASTM International.
65. Fitzsimons, G. and H.A. Kuhn, *A device for control of high speed compression testing at constant true strain rates.* Journal of Physics E: Scientific Instruments, 1982. **15**(5): p. 508.

66. Casem, D.T., S.E. Grunschel, and B.E. Schuster, *Normal and Transverse Displacement Interferometers Applied to Small Diameter Kolsky Bars.* Experimental Mechanics, 2012. **52**(2): p. 173-184.
67. Song, B., et al., *Determination of Early Flow Stress for Ductile Specimens at High Strain Rates by Using a SHPB.* Experimental Mechanics, 2007. **47**(5): p. 671-679.
68. Song, B., et al., *High-rate Characterization of 304L Stainless Steel at Elevated Temperatures for Recrystallization Investigation.* Experimental Mechanics, 2010. **50**(4): p. 553-560.
69. Song, B., B.R. Antoun, and M. Boston, *Development of high-temperature Kolsky compression bar techniques for recrystallization investigation.* The European Physical Journal Special Topics, 2012. **206**(1): p. 25-33.
70. Frew, D.J., M.J. Forrestal, and W. Chen, *Pulse shaping techniques for testing elastic-plastic materials with a split Hopkinson pressure bar.* Experimental Mechanics, 2005. **45**(2): p. 186-195.
71. Frew, D.J., M.J. Forrestal, and W. Chen, *Pulse shaping techniques for testing brittle materials with a split hopkinson pressure bar.* Experimental Mechanics, 2002. **42**(1): p. 93-106.
72. Clausen, A.H., et al., *Flow and fracture characteristics of aluminium alloy AA5083–H116 as function of strain rate, temperature and triaxiality.* Materials Science and Engineering: A, 2004. **364**(1–2): p. 260-272.
73. Rösler, J., H. Harders, and M. Bäker, *Mechanical behaviour of engineering materials: metals, ceramics, polymers, and composites*. 2007: Springer Science & Business Media.
74. Camacho, G.T. and M. Ortiz, *Adaptive Lagrangian modelling of ballistic penetration of metallic targets.* Computer Methods in Applied Mechanics and Engineering, 1997. **142**(3): p. 269-301.
75. Johnson, G.R. and W.H. Cook. *A constitutive model and data for metals subjected to large strains, high strain rates and high temperatures*. in *Proceedings of the 7th International Symposium on Ballistics*. 1983. The Hague, The Netherlands.